Texture and chemistry of pyrite from the Waihi epithermal system, Hauraki Goldfield, New Zealand

A thesis

submitted in partial fulfilment

of the requirements for the degree

of

Masters of Science in Earth Sciences

at

The University of Waikato

by

Anna G Eames

THE UNIVERSITY OF
WAIKATO
Te Whare Wānanga o Waikato

2017

Abstract

The Waihi epithermal system is a low sulfidation epithermal system that hosts one of the largest epithermal Au-Ag deposits in the Southern Hemisphere. Various sulfide minerals are present within the system, including pyrite (FeS_2), one of the most abundant sulfide minerals on Earth. Pyrite is an archive for hydrothermal fluid chemistry due to its crystal structure enabling incorporation of other elements such as Co, Ni, Se, As, Te. The presence or absence of these elements reflects the changes in the hydrothermal fluid chemistry throughout the growth of the grain. The textural variations in the grains indicates changes in growth conditions for each grain at the time of formation. The chemistry of each different zone, coupled with stages of growth, indicates the chemical influences on the pyrite in the Waihi system at that time.

The use of petrographic, EPMA and LA-ICPMS analyses demonstrates distinctive textural zones within pyrite grains, varying in chemistry and appearance. Some zones contain elevated concentrations of Au and Ag, and varying concentrations of Cu, Pb or Zn. The textural observations indicate pyrite growth was interrupted by periods of dissolution before the grain continued growing. Most grains begin growth with high trace element concentrations. The lowest concentrations of trace elements occur in the outer growth phase. Inclusions are rich in Pb, Ca, Se, Zn, Au and Ni, and cause the ‘dirty’ texture observed in grains. The distinctive textural features are attributed to the varying concentrations in Au, As, Cu, Zn, Ag and Te.

This research showcases the dynamics of hydrothermal fluid flow at Waihi, revealing that the gold-forming hydrothermal system at Waihi are more complex than initially thought. There is both evidence for periods of low gold pyrite growth, and periods of high pyrite growth.

This thesis is dedicated to Cyrano Embling,

your unwavering support and patience made it all possible.

Thank you for always listening.

I could not have done it without you.

Acknowledgments

I would like to thank Dr Shaun Barker for setting up this project, and providing me with incredible opportunities during the course of my research. Thank you for all the help and support with the writing stage, especially towards the end, when I struggled to get the words out.

To Dr Patricia Durance (GNS), thank you for all your support and continued interest in this study. I appreciate your time and feedback, especially with the more technical writing (and referencing!).

A big thank you to Steve Cameron for conducting all the LA-ICPMS analysis, in spite of vacuum pump failures and other technological difficulties.

To Dr Ian Schipper, thank you for all your help making the EPMA analysis happen so smoothly, and your continuing optimism during the frustrating times.

To Dr Steve Micklethwaite (Monash University, Australia), Dr Louise Fisher (CSIRO) and David Paterson (Australian Synchrotron), thank you for making the time at the Australian Synchrotron so entertaining. Such an incredible learning experience.

A huge thank you to Sarah Fyfe, whose previous research helped build the foundations which this study is based on, and provided me with a ready set of samples at my fingertips.

To my fellow students, thank you for all the talks and shared coffees. It is nice to know we all struggle with our work at some point, and that we all can get through it.

A massive thank you to my family; Dad, for the inspiration to further my education, Mum, for the café dates (often a much-needed break), and both of you for all the proof reading I put you through! Jen, thank you for your interest in my studies.

A big thank you to Karen and Owen, for your support, and the lake days over summer that provided brief respite, especially towards the end.

To Harrietanne, thank you for taking the opportunity to show me Melbourne, and driving me to the Synchrotron.

Thanks to the Australian Synchrotron for access to their amazing facility. Also to the University of Victoria for providing access to their SEM, and the EPMA analysis.

Funding for this research was provided by the New Zealand Ministry of Business, Innovation and Employment, the University of Waikato, the Education Endowment Trust of the Australasian Institute of Mining and Metallurgy (AusIMM), the Crown research organisation of Geological and Nuclear Sciences (GNS), the Broad Memorial Fund, and the New Zealand Geoscience Society.

Table of Contents

Abstract iii

Acknowledgments vii

List of Figures xiii

List of Tables xvii

1. Introduction to Epithermal Settings 19

1.1 Introduction 19

1.2 Epithermal Settings 20

1.2.1 Pyrite in Epithermal Settings 21

1.3 Sulfidation in Epithermal Systems 22

1.3.1 Pyrite in Pyrite in Low Sulfidation Systems 22

1.3.2 Genesis 23

2. Pyrite 25

2.1 Pyrite 25

2.1.1 Pyrite Mineralogy 25

2.1.2 Pyrite Chemistry 27

2.2 Environmental Issues (AMD) 29

2.3 Context of Study 31

2.4 Case Studies 31

2.5 Industry Application 34

2.6 Conclusion 35

3. Geological Setting 37

3.1 Regional Geology 37

3.2 Local Geology 39

4. Methods 43

4.1 Sampling 43

4.2 Bleach Etching Method 48

4.3 XFM Analysis 49

4.3.1 Data Reduction 50
4.4 EPMA Analysis Method 52
4.4.1 Data Reduction 53
4.5 LA-ICPMS Analysis 54
5. Pyrite Textures 55
5.1 Pyrite Textures in the Martha Deposit, Waihi Epithermal System 55
5.1.1Classification Scheme 55
5.2 Classification of samples 57
5.3 Discussion 67
5.3.1 Sulfidation and Crystal Growth 67
5.3.2 Zoning and Crystal Growth 68
5.3.3 Fluid Changes 71
5.3.4 Relationships 73
5.4 Limitations 76
5.5 Comparisons 77
6. Trace Element Composition of Pyrite 82
6.1 Trace Element Composition of Pyrite in the Martha Deposit 82
6.2 XFM analysis – Element Associations 82
6.3 EPMA 93
6.4 LA-ICPMS 100
6.5 Discussion 110
6.5.1 Element Behaviour 111
6.5.2 Chemistry and Growth 118
6.5.3 The Independence of Gold 120
7. Discussion 127
7.1 Summary of Findings 127
7.2 Theories on Au-Ag Mineralisation 127

7.3 Implications on Precious Metal Deposits in New Zealand 129
7.3.1The Waihi Au-Ag Deposit..... 129
7.3.2 The Taupo Volcanic Zone..... 131
7.3.3 Future Exploration 132
7.4. Future Work..... 133
8. Conclusion 135
References..... 137
Appendices 146
Appendix I – Samples 146
Appendix II – Raw Data 146
Appendix III – Analysis Images 146

List of Figures

1.1.1: Maps showing Waihi location in New Zealand. Waihi is in the circle (adapted from Christie et al., 2001). ……..**19**

2.4.1: Zoned pyrite from Sukhoi Log gold deposit. The most inner zone is py3 (euhedral pyrite growing over framboidal pyrite), py4 is a synmetamorphic zone, py5 is the outer zone parallel to quartz vein bedding (Large et al., 2009)……**32**

2.4.2: backscatter image of an As rich pyrite grain showing the variation in As toward the outer edge (Baker et al., 2006). ……**34**

3.1.1: The Hauraki Goldfield, with black circles indicating locations of epithermal Au-Ag deposits. Inset figure of location of the Hauraki Goldfield in the North Island, New Zealand (Brathwaite & Faure, 2002)……**38**

3.2.1: Map of the local Waihi geology. Quartz lodes have been projected on the surface for ease of visibility (Brathwaite & Faure, 2002)……**39**

3.2.2: Cross section (A-B) of the Waihi Vein system with main lithologies and alteration zones. Inset image shows location of the cross section A-B. I/S is the medial illite-smectite zone. Location of drill holes W21, W20, W2 and W7A are noted (adapted from Brathwaite & Faure, 2002). ……..**41**

4.1.1: Map showing the locations and geology in the sampling area (adapted from Fyfe, 2014). ……...**43**

4.1.2: Example of the 1 inch epoxy mounts. A: AU58203, B: AU58144, C: AU57390B and D: AU57390. A, B and C all have visible sulfides….....**44**

4.1.3: Examples of hand sample (P56023) on the left and thin section (WDH9_169.5) on the right. Both found through PetLab and are from Brathwaite (1982). ……**45**

4.2.1: A – sample AU57390 before etch. B – same area on sample AU57390 after bleach etching……..**48**

5.1.1.1: A – inter grain zoning in pyrite from AU57417. Zones have been labelled Py1 to Py3 based on relative shading within each grain; Py1 is palest, Py3 is darkest. B – intra grain zoning in pyrite from AU56192_Z2 with zones Py1, Py2 and Py3 within single grain……...**55**

5.1.1.2: A – example of a clean boundary between Py1 and Py2 from sample AU57390B_Z1. The solid black line indicating where the boundary occurs. B – example of irregular zone boundaries between Py1 and Py2 in sample AU56196_Z2. The black dashed line indicates a possible boundary. ……**56**

5.1.1.3: Example of the radial zoning shape in sample AU58148_Z2. ……**56**

5.1.1.4: Example of planar zoning in sample AU58144_Z1. Where zone Py1 does not extend radially from the grains centre. ……**57**

5.2.1.1: Pyrite from AU57417 showing inter grain variation. Different shades have been labelled Py1 to Py3 based on colour; Py1 is palest, Py3 is darkest. ……**58**

5.2.1.2: Examples of ICR zoning from A: AU56192_Z2, B: AU56192_Z1, C: AU56192_Z3b and D: AU58148_Z2……**61**

5.2.1.3: Examples of IDR zoning in A: AU56192_Z3a and B: AU60281_Z1……**62**

5.2.1.4: Examples of ICRB zoning in A: AU57390B_Z1 and B: AU57390B_Z2a……**63**

5.2.1.5: Examples of ICP zoning from A: AU56202_Z4, B: AU56211, C: AU57414 and D: AU57417_Z1……**64**

5.2.1.6: Examples of IDP zoning in A: AU58148_Z1 and B: AU60281_Z3……**65**

5.2.1.7: Examples of IDPB zoning in A: AU58144_Z1 and B: AU56196_Z2……**66**

5.3.2.1: The three stages of growth that could produce a grain with ICRB zoning…….**69**

5.3.2.2: Suggested growth history of an ICP grain, where the beginning has two grains, that fuse to one……**70**

5.5.1: EMP maps of A- Cu, B- Fe, C- Ag, D- As from pyrite in the Pascua epithermal system. The numbers in C show the various growth zones. The numbers in D indicate EMP spot analyses. The bright spots in A and D are soluble sulfates. The bright spots in C are late iodargyrite and chlorargyrite (Chouinard et al., 2005). ……..**78**

5.5.2: Examples of the zoning found in the various deposits studied by Large et al. (2009). A; the Sukhoi Log deposit with Au inclusions. B; Spanish Mountain. C; Bendigo gold deposit. D; Sukhoi Log gold deposit……..**79**

5.5.3: Sample AU57390B_Z2a from Waihi (left) next to pyrite from Sukhoi Log (right). There are similarities between the grain's central texture and outer cleaner zone. ……**80**

5.5.4: sample AU57390B_Z1 from Waihi (left), next to pyrite from Spanish Mountain (right) (Large et al., 2009). Similarities between the pyrites can be seen, with the dirty central zoning and clean outer zone. ……..**80**

6.2.1: Images of sample AU56187. The hand sample was cut into two thin sections. Left is AU56187A, right is AU56187B. The red numbers show the different XFM analysis points……**83**

6.2.2: example of a RGB image of element distribution modelled from the XFM data. Image from sample AU56187A_2. Red: Au, Green: As, Blue: Fe. ……**84**

6.2.3: RGB image AU56187B_5 from the XFM data showing the As bands within pyrite. Red: Au, Green: As, Blue: Fe…….....**85**

6.2.4: RGB image from sample AU56187B_4. XFM data showing the As bands within pyrite. Red: Au, Green: As, Blue: Fe. ……**85**

6.2.5: RGB image from sample AU56187A_3. XFM data showing the As bands within pyrite. Red: Au, Green: As, Blue: Fe. ……**86**

6.2.6: RGB image from sample AU56187B_7. XFM data showing the As bands (paler blue) within pyrite. Red: Au, Green: As, Blue: Fe. ……**86**

6.2.7: RGB image from sample AU56187A_5 showing an arsenic-rich pyrite grain with gold inclusions. The blue edge of the grain is Cu-rich. Red: Au, Green: As, Blue: Cu…..**88**

6.2.8: RGB image from sample AU56187A_5 showing the occurrence of Au (green) and Ag (red) outside of the As-rich pyrite grain (blue). Red: Ag, Green: Au, Blue: As.....**89**

6.2.9: RGB image from sample AU56187A_4 showing the occurrence of Ag (red) outside of the pyrite grain. Red: Ag, Green: As, Blue: Fe. ……**90**

6.2.10: RGB image from sample AU56187A_4 showing the occurrence of Ag (red) outside of the pyrite grain. Red: Ag, Green: As, Blue: Fe. ……..**90**

6.2.11: RGB image from sample AU56187A_4 showing the occurrence of Au (red) outside of the pyrite grain. Red: Au, Green: As, Blue: Fe. As is present in this sample in the matrix, coating the quartz grains, as well as present in the pyrite grains. ……..**91**

6.2.12: RGB image from sample AU56187B_6 showing the appearance of a bubble with a Mn and Fe-rich wall, containing a fleck of gold. Red: Au, Green: Mn, Blue: Fe……**92**

6.3.1: image of grain from sample AU57390B_Z1. The red numbers indicate the location of point analysis. The maximum, average and minimum As values are annotated on the corresponding zones in blue……..**96**

6.3.2: graph of As, Au, Ag, Zn and Cu concentration across zones 1-6 on sample AU57390B_Z1. The numbers correspond to numbered points on figure 6.3.1 above. Au, Ag, Zn, Cu on Y axis. As on Z axis……**96**

6.3.3: image of grain from sample AU60281_Z3. The red numbers indicate the location of point analysis……..**97**

6.3.4: graph of element concentration across zones 1-8 on sample AU60281_Z3. The numbers correspond to numbered points on figure 6.3.4 above. Y axis: Au, Ag, Zn. Z axis: As, Cu…….**97**

6.3.5: image of grain from sample AU57390B_Z2. The red numbers indicate the location of point analysis. ……**98**

6.3.6: graph of element concentration across zones 1-7 on sample AU57390B_Z2. The numbers on the x axis correspond to numbered points on figure 6.3.5 above..……**98**

6.3.7: graph of the distribution of trace element concentrations with depth……..**99**

6.4.1: image of grain AU56192_Z1 and cell space maps produced from the LA-ICPMS analysis……**101**

6.4.2: image of grain AU56192_Z2 and cell space maps produced from the LA-ICPMS analysis……102

6.4.3: image of grain AU56192_Z3b and cell space maps produced from the LA-ICPMS analysis……103

6.4.4: image of grain AU57390B_Z1 and cell space maps produced from the LA-ICPMS analysis……104

6.4.5: image of grain AU57390B_Z2 and cell space maps produced from the LA-ICPMS analysis……..**105**

6.4.6: image of grain AU58144_Z1 and cell space maps produced from the LA-ICPMS analysis……..**106**

6.4.7: image of grain AU57414_Z1 and cell space maps produced from the LA-ICPMS analysis……..**107**

6.4.8: image of grain AU57417_Z1 and cell space maps produced from the LA-ICPMS analysis……..**108**

6.4.9: image of grain AU58148_Z2 and cell space maps produced from the LA-ICPMS analysis……..**109**

6.5.1.1: A- SEM backscatter image of zoning in sample AU56192_Z1. B- Microprobe image of As zoning in a pyrite from Pajingo (Baker et al., 2006)……..**112**

6.5.1.2: graph showing the maximum concentrations of Zn, Cu and Pb against depth. The dotted line indicates the Cowshed sample……**115**

6.5.2.1: image of a pyrite grain from the Pascua deposit that exhibits sector zoning. The white arrows are suggesting a favoured orientation for the incorporation of As into the [111] stage pyrite (Chouinard et al., 2005)……**119**

6.5.3.1: Graphs of the relationship between Au and As, Cu, Zn, Pb and Ag and As, Cu, Zn, Pb……..**120**

7.3.1.1: graph of trace elements against depth. The Cowshed sample is the highest in Cu, Pb and Se. ……**129**

List of Tables

4.1.1: Mineral assemblages of samples, adapted from Fyfe (2014)……...**46**

4.1.2: Sample descriptions, adapted from Fyfe (2014)……**47**

5.2.1.1: Results of the bleach etching showing the different types of intra grain zoning……**59-60**

6.3.1: Element concentration medians in mass% from EPMA analysis……**94**

6.3.2: Element concentration maximums in mass% from EPMA analysis……**94**

6.3.3: Element concentration minimums in mass% from EPMA analysis……**95**

1. Introduction to Epithermal Settings

1.1 Introduction

Epithermal deposits are an important source of gold and silver, originating from high-temperature, subaerial hydrothermal systems (Simmons et al., 2005). Valuable deposits in epithermal settings are found as vein structures and range in gold grade, with typical reported assay values below 600 m ranging from 0.1 to 2 g/t Au, 5 to 70 g/t Ag, 0.3 to 4 wt% Zn, 0.05 to 2 wt% Pb and 0.01 to 0.2 wt% Cu (Brathwaite & Faure, 2002). These systems are often associated with calc-alkaline to alkaline magmatism, in volcanic arcs and rift settings. Pyrite (FeS_2) is one of many hydrothermal minerals found in such systems, and is of interest in these settings due to its ability to incorporate various trace elements (Large et al., 2011). The chemical variation in the fluid passing through a system over time has the potential to be recorded in the growing pyrite grains (Baker et al., 2006, Large et al., 2009).

Waihi, in the North Island of New Zealand, is situated in a former volcanic arc setting (Christie et al., 2001). Figure 1.1.1 shows the location of the Waihi epithermal system in the North Island, at the base of the Coromandel Peninsula. There is a common occurrence of pyrite within the veins of the Waihi system, as well as the surrounding host andesites (Brathwaite & Faure, 2002), providing the opportunity for a study of changes in the fluid chemistry during pyrite growth at Waihi.

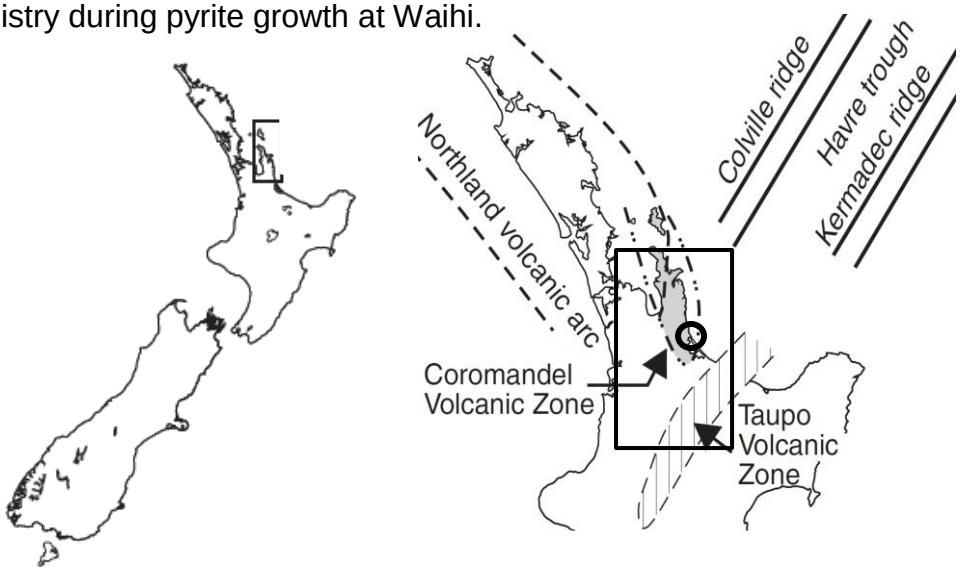

Figure 1.1.1: maps showing Waihi location in New Zealand. Waihi is in the circle (adapted from Christie et al., 2001).

1.2 Epithermal Settings

Deposits in epithermal systems are formed at a shallow depth (~1.5 km) beneath the Earth's surface in temperatures of less than ~300°C (Zhu et al., 2011) The districts which host epithermal veins can range in size from <10 to >100 km^2 and have a diversity of shapes (Zhu et al., 2011). Veins within ore bodies make up a comparatively small volume of the whole system (Simmons et al., 2005). The shapes of veins and associated ore bodies differ depending on the permeability, which is influenced by the lithological and structural controls. Most commonly, ore bodies are found in veins that formed in dilational or extension cracks which provided a pathway for hydrothermal fluids (Rowland & Sibson, 2004). Ore bodies can be hosted by major faults, but are more typically hosted by minor faults with small displacements. The optimum structural development is dependent on the host rock rheology and associated brittle failure, with lithology a dominant control for porosity and permeability development. These characteristics can be intrinsic to the host rock, but also a by-product of hydrothermal alteration (Simmons et al., 2005). The mineralisation of the precious metals in an epithermal system relies on zones of high paleo-permeability within sequences of coeval volcanic and underlying basement rock. The highest grade ore tends to occur in the more steeply dipping veins, where fractures or cracks in the rock create areas of high permeability and encourage mineralisation (Simmons et al., 2005).

Epithermal deposits are characterised based on their alteration and gangue mineral assemblages and their metal and sulfur content, and sulfide mineral assemblages (Christie et al., 2007). Typical gold and silver bearing deposits in low sulfidation systems, are quartz ± calcite ± adularia ± illite alteration assemblages containing Au-Ag, Ag-Au or Ag-Pb-Zn ores (Brathwaite & Faure, 2002). Electrum, acanthite, silver sulfosalts, silver selenides and Au-Ag tellurides are the main gold and silver bearing minerals with minor sphalerite, galena and chalcopyrite also typical (Simmons et al., 2005). Generally, quartz is the major gangue mineral often accompanied by varying concentrations of chalcedony, adularia, illite, pyrite, calcite and sometimes rhodochrosite. Quartz, adularia, illite and pyrite form proximal

alteration zones that envelope orebodies (Christie et al., 2007). Contrastingly, hydrothermal alteration zones exist over a distal or regional scale and are extensive and propylitic. Ore grade mineralisation in epithermal systems typically increases with the depth of the system. If erosion occurs, the system can be buried by regional scale clays (Simmons et al., 2005).

1.2.1 Pyrite in Epithermal Settings

Hypogene pyrite occurs in hydrothermally altered cores. The iron sulfides are generally thinly disseminated through the host rock and veins. Sulfur for the formation of iron sulfide minerals typically comes from the H_2S in the geothermal fluid (Steiner & Rafter, 1966).

In most hydrothermal deposits, gold is primarily hosted in chalcopyrite, arsenopyrite, pyrrhotite and pyrite. The sulfide concentration in the host rock can vary hugely and the gold concentration can alter within grains. Gold mostly occurs as micro-inclusions if conditions are oversaturated with respect to gold. The equation for the incorporation of gold into As-rich pyrite can be seen below (Zhu et al., 2011).

$$Fe(S_2As)_2 + 2Au(HS) = Fe(S_2As)_2 \cdot Au2S + H_2S$$

$$Fe^{2+} + 2HAsS_2 + 2Au(HS) + 2H_2 = Fe(S_2, As) \cdot Au_2S + 3H_2S + 2H^+$$

The most typical evolution is from an early leaching and alteration stage to an ore forming stage. The most common mineral formation is vuggy silica rock with advanced clay (argillic) assemblages and disseminated pyrite. This forms early stage acidic alteration and is usually followed by Cu, and/or Au, and/or Ag deposition (Arribas Jr, 1995). The initial growth of pyrite is where the incorporated gold and other trace elements As, Ni, Pb, Zn, Mo, Te, V and Se are usually concentrated (Chouinard et al., 2005). During diagenetic pyrite growth these can be remobilised and concentrated in the outer growth zone, causing the zoning within the pyrite grain. These textural

differences based on the zoning can be examined to give a history of the conditions of the fluid in which the pyrite grew (Large et al., 2009).

1.3 Sulfidation in Epithermal Systems

The term sulfidation was initially applied to describe the oxidation state of the aqueous sulfur species in deep ore-forming solutions (Simmons et al., 2005). It has since been modified to describe more of the minerals found in the ore. High sulfidation systems are majorly pyrite-enargite ± luzonite, covellite-digenite, farnatinite, orpiment (Zhu et al., 2011). Intermediate sulfidation systems are characterised by tennantite, tetrahedrite, hematite-pyrite-magnetite, pyrite, chalcopyrite, Fe-poor sphalerite and pyrite (Simmons et al., 2005). Low sulfidation systems contain arsenopyrite-loellingite-pyrrhotite, pyrrhotite, Fe-rich sphalerite and pyrite (Simmons et al., 2005). Low sulfidation systems occur in calc-alkaline, alkaline and tholeiitic bimodal basalt-rhyolite rocks and the tectonic setting is typically a magmatic arc undergoing extension (Zhu et al., 2011). Low sulfidation systems will be focused on for the rest of the chapter, as Waihi is defined as a low sulfidation system (Brathwaite & Faure, 2002, Simmons et al., 2005).

1.3.1 Pyrite in Pyrite in Low Sulfidation Systems

In low sulfidation epithermal systems, the main hydrothermal minerals that occur are quartz, illite, adularia, albite, chlorite, calcite and pyrite. In low sulfidation systems in New Zealand, pyrite is the most common sulfide and occurs primarily as a replacement phase for magnetite and ferromagnesium minerals (Simmons & Browne, 2000). Pyrite in low sulfidation systems has been shown to exhibit internal zoning structures, of bands of high As and bands of low As pyrite (Baker et al., 2006). In previous studies of pyrite found in sedimentary rocks associated with hydrothermal ore deposits, hydrothermal pyrite is commonly depleted in Ni, V, Zn, Pb, and Ag with cyclic zonations of Co, Ni, and As, compared to earlier formed diagenetic pyrite. The outermost hydrothermal pyrite rims are either As-Au rich, or Co-Ni rich and As-Au poor (Large et al., 2009). Metamorphic and/or

hydrothermal pyrites are expected to be coarser grained and less enriched in trace elements due to the higher temperature and slower growth of pyrite, which allows the trace elements to be partitioned into separate sulfide phases rather than incorporated into pyrite in solid solution or as very small (<5μm) inclusions (Large et al., 2009). In high sulfidation systems, similar zoning characteristics have been observed, with the same high trace element concentration in the early pyrite growth, followed by a trace element depleted secondary growth zone (Chouinard et al., 2005). These zoning characteristics have been briefly documented as present in low sulfidation epithermal systems. Baker et al. (2006) describe As zoning in a pyrite grain from the Pajingo deposit, another low sulfidation system. Their work is discussed further below and in chapters 6 and 7.

1.3.2 Genesis

Pyrite forms in epithermal settings by the passing of hydrothermal fluid at high and low temperatures and the subsequent deposition of iron and sulfur. The hydrothermal fluids are reduced and near neutral in pH, with chloride being the dominant aqueous constituent in collected hot water samples, although in deep chloride waters, CO_2 species are often more dominant. The presence of reduced sulfur influences the solubility of metals (Simmons et al., 2016). The heat is provided by magmatic influence at depth, which is either an intrusion but more commonly a large magma chamber. The growth of pyrite occurs due to sulfidation, where the Fe from the host rock becomes mobilised due to the fluid presence. This allows the S from the fluid to bind with the Fe from the host rock, and pyrite growth begins (Chouinard et al., 2005).

The crystal structure of pyrite, as mentioned above, allows trace elements present in the hydrothermal fluid to be included in the pyrite grain (Deol et al., 2012). As the fluid chemistry changes, so too does the chemistry of the growing pyrite grain. In high sulfidation systems, fluid variations are common and zoned pyrite is often observed (Chouinard et al., 2005). In low sulfidation systems, variations are less common, and pyrite grains are commonly observed as being homogenous (Arribas Jr, 1995). Sulfur can also form other sulfide species such as chalcopyrite, sphalerite and galena.

This occurs when there is the presence of copper, zinc and lead respectively either in the host rock or in the hydrothermal fluid (Simmons & Browne, 2000). The reason pyrite is of interest is due to its ubiquitous nature, and the occurrence of Au, Ag and trace elements in the pyrite crystal structure. These inclusions are often not visible to the naked eye or under reflected light microscopy and detection of these metals is typically through SEM or laser ablation inductively coupled plasma mass spectrometry (LA-ICPMS) analysis (Deol et al., 2012). Optimum conditions for ore grade deposits are periods of deep boiling and high metal fluxes, synchronized with conditions of strongly focused fluid flow at <2 km depths (Simmons et al., 2016).

As highlighted above, pyrite is a ubiquitous hydrothermal mineral in epithermal systems. Therefore, understanding how pyrite chemistry varies over time and space has the potential to provide information about ore genesis, and potential environmental impacts of mining. In the following sections, I summarize background information on the mineralogy, structure and chemistry of pyrite and highlight the environmental issues associated with mining sulfides, the use of sulfides in exploration and what previous studies on pyrite zoning have shown. This section ends with a summary of the main points associated with this study, and outlines the key questions that will be addressed.

2. Pyrite

2.1 Pyrite

FeS_2 (iron disulfide, or pyrite) is the most abundant of the sulfide minerals on Earth. It is found in hydrothermal deposits, veins, igneous and sedimentary rocks and as a replacement mineral and is sought after not for its economic value but because it is often found in association with valuable sulfide minerals such as sphalerite, chalcopyrite and galena. In some cases pyrite can also carry dispersions of gold and other valuable metals, and is also used for the production of sulfuric acid (Chandra & Gerson, 2010). There are two crystal forms of iron disulfide; cubic pyrite and orthorhombic marcasite. Pyrite is a semiconductor which causes anisotropy for some physical properties.

2.1.1 Pyrite Mineralogy

Pyrite is opaque with a pale brass yellow colour and is irridescent when oxidised. It has a greenish black or brownish black streak and a metallic lustre, giving it the easy misidentification as native gold. In polished section pyrite is creamy white, isotropic (occasionally anisotropic) and can display pleochroism. It can also show zonal growth or banding (Lowson, 1982).

Pyrite morphology can be used to identify the setting in which it formed. For example, in sedimentary settings, pyrite is often disseminated, making it invisible without a microscope, and has a framboidal morphology (Lowson, 1982). Most framboidal pyrite is a primary sedimentary mineral, forming as a result of bacteriogenic H_2S during early diagenesis (Berner, 1970). Primary replacement pyrite is pyritic material that has replaced plant parts, with grains often having well-developed faces, distinguishing them from disseminated pyrite. Secondary replacement pyrite has well-developed crystal faces and is not framboidal, it includes fracture filling pyrite. These different forms of pyrite have different reactivities (Lowson, 1982).

FeS_2 can exist in two polymorphs; pyrite which is cubic and marcasite which is orthorhombic. Marcasite is less stable and not as widespread as pyrite. Pyrite has a face centred crystallographic arrangement similar to rock salt (NaCl) with the Fe^{2+} ion centred between two S^{2-} anions. In marcasite, each

Fe^{2+} ion is oriented to six S in a distorted octahedral arrangement. Each S is oriented to one S and three Fe^{2+} in a distorted tetrahedral arrangement. The S_2^{2-} dumbbells are diagonal, alternating in orientation for each crystal layer. This is different from the high symmetry, close packed NaCl structure, but despite this pyrite is very dense (~5.02 g cm^{-3}) (Chandra & Gerson, 2010).

Pyrite can also form as a dodecahedron with pentagonal shaped faces (pyritohedron) as well as octahedral crystals with triangular faces. The crystals are usually striated due to microscopic alternation of cubic and dodecahedron growth. Natural pyrite is found as a single morphology, or as a varied combination of the aforementioned structures. Pyrite shows poor fracture which is dominantly conchoidal (Chandra & Gerson, 2010).

The difference in electronegativity of Fe and S indicates the bonding of pyrite is likely to be mostly covalent, defined by the overlap of the 3d valence electrons of Fe and the 3p valence electrons of S. Pyrite is the most electrochemically inert of all the common sulfide minerals due to its relatively high rest potential of ~0.66 V (Brostigen & Kjekshus, 1969). The shortest interatomic distance calculated between two anionic pairs is thought to be $d_{S\text{-}S}$ of 2.20 A and $d_{S\text{-}S}$ of 2.14 A. The typical lengths between Fe and S is considered to be $d_{Fe\text{-}S}$ of 2.26 A and $d_{Fe\text{-}S}$ of 2.27 A. This differs from minerals like chalcopyrite and sphalerite, as in these there is no S to S bonding. The different polymorphs of pyrite have different termination surface stabilities. The loss in coordination of surfaces results in a higher dangling bond density, creating highly reactive sites. Surfaces have to undergo relaxation to stabilise low coordinated sites, which results in a shortening of the S-S and Fe-S bond lengths (Chandra & Gerson, 2010). This information is useful for predicting potential chemical weathering, or how the ore rock may respond to the different mining practices.

2.1.2 Pyrite Chemistry

There are reported minor deviations from the stoichiometric relationship of Fe and S_2, meaning a higher cation or anion concentration and a ratio of 1:1.978 or 1:2.2027. These deviations can occur because of the lattice substitutions of the ferrous and sulfide ions with other atoms of a similar radius and atomic charge (Chandra & Gerson, 2010). These trace elements can be Co, Cu, Cr, Ni, Zn, Pb, As and Mo. Also found but less common are Ag, Ga, Ge, Y, Zr, Nb, Sn, Sb, La, Ce, Bi, Th and U. These elements can be useful for identifying the possibility of hydrothermal remobilisation of ores containing pyrite (Huang, Gao, Qi, & Zhou, 2015). These minor trace elements can cause significant variations in the conducting properties of pyrite and directly affect the reactivity of the surface. This is information that can be used in geometallurgy; where the identification of trace elements present in pyrite at potential mine sites can strengthen the case that mining could occur. The presence of some trace elements could also be harmful to the environment so identifying the 'impurities' in the ore can help environmental management practices. The distribution of these minor trace elements is not homogeneous, creating site specific variations and resulting in major implications for leaching and flotation behaviour (Chandra & Gerson, 2010; Zhu et al., 2011). These trace elements found within pyrite are typically divided into three groups; 1) elements that occur mostly as inclusions (Cu, Zn, Pb, Ba, Bi, Ag, and Sb), 2) nonstoichiometric substitutions in the lattice (As, Tl, Au and sometimes Mo), and 3) stoichiometric substitutions for Fe (Co and Ni) or S (Se and Te). In hydrothermal and metamorphic recrystallization conditions, the first two groups are removed from the pyrite and the third is unaffected (Huston et al., 1995). Up to 200 ppm of As and Au is found in colloform pyrite grains from volcanic hosted massive sulfide (VHMS) deposits. The relationship between high concentrations of detectable As, Tl and Au, along with Tl and Au enrichment in the colloform pyrite indicates a rapid precipitation of pyrite, allowing the incorporation of As, and hence Tl and Au (Huston et al., 1995). Subsequently, low As, Tl and Au concentrations imply slow crystallisation of pyrite (Huston et al., 1995).

In low temperature conditions it is typical for the pyrite to contain a large variety of trace elements which have been incorporated into the nanoparticles within the pyrite structure. Arsenic is the most common element to be incorporated into pyrite. Arsenian pyrite with high concentrations of trace elements is abundant in low and high temperature hydrothermal systems (Large et al., 2009). Most nanoparticles found in hydrothermal pyrite are crystalline and formed by exsolution from the pyrite matrix, or as a precipitation from the hydrothermal solution. Exsolved trace element nanoparticles are generally smaller than those that are directly precipitated. 'Pure' pyrite and Cu-rich pyrite have less ability to accumulate trace metals then arsenian pyrite (Deditius et al., 2011).

Pyrite can incorporate up to ca. 10 wt% of arsenic into the structure, strongly impacting on arsenic's mobility. Arsenic rich pyrites often contain trace elements and valuable metals such as gold. The two main forms are arsenopyrite (FeAsS) and löllingite ($FeAs_2$), both of which are orthorhombic, as well as incorporations of arsenic into the crystal lattice of pyrite by atomic substitution. In both oxidising and reducing conditions, the substitution of As for S is preferable to the substitution of As for Fe (Blanchard et al., 2007). The formation of an AsS group is energetically favoured over the formation of an As_2 group. During the dissolution of pyrite, the forming of sulfur vacancies will preferentially occur if arsenic is present (Blanchard et al., 2007).

The oxidation of pyrite is economically important in mineral flotation and leaching. The oxidation of pyrite can cause hydrophobicity or hydrophilicity to pyrite surfaces and influence interactions with collectors during flotation (Chandra & Gerson, 2010). Oxidation is a major process involved in the dissolution of pyrites during leaching and is described in the equation below (Lowson, 1982).

$$FeS_2 + 8H_2O \rightarrow Fe^{3+} + 2SO_4^{2-} + 15e^- + 16H^+$$

Aqueous oxidation processes also play a significant role in the acidification of natural water systems by producing sulfuric acid. This can occur by the natural weathering of pyritic rocks and shale, or from the waste dumps of mining operations (acid mine drainage - AMD) (Chandra & Gerson, 2010). For oxidation and reduction to occur there needs to be a vacant orbital in fluid phase or a vacant site in solid phase (Luther, 1987). Oxidation of pyrite surfaces can occur if they are exposed to atmospheric O_2 and water. The resulting oxidation layer can passivate against further oxidation, determining subsequent aqueous phase oxidation processes. Different surface species and abundance on a freshly fractured surface can determine the atmospheric reactivity. During the conchoidal fracture of pyrite, rupturing of the Fe-S bonds creates S_2^{2-} surfaces and a reduced coordination to Fe (Chandra & Gerson, 2010).

It is suggested that S-S bonding is weaker than Fe-S bonding in pyrite, meaning that during fracture of the pyrite, more S-S bonds are broken. Pyrite oxidation is initiated by minutes of exposure to the atmosphere, causing S^{2-} oxidation. Sulfate ($Fe_2(SO_4)_3$) is the main oxidation product, representing up to 39% of all surface oxidation products. Fe^{3+} oxy-hydroxide (FeOOH) is the next main oxidation product after sulfate (Chandra & Gerson, 2010). Pyrite, as a sulfide, has the potential to affect the environment as it breaks down. This is discussed further below.

2.2 Environmental Issues (AMD)

One of the major environmental issues associated with mining epithermal systems in New Zealand is acid mine drainage (AMD). This is the result of oxidising sulfidic waste rock producing sulfate anions (SO_4^{2-}) and sulfuric acid when reacting with groundwater or pit water runoff (Castendyk & Webster-Brown, 2010). Subsequent acidification can lead to the mobilisation of dissolved metals (Craw, 2001). This acid, accompanied by dissolved metals from the waste rock, then drains into waterways, lowering the pH, contaminating the local stream ecology and often drinking water for nearby towns. This is an issue that occurs not only in actively mined sites

all over New Zealand (Anawar, 2015), but also in those that have been abandoned and lack an environmental rehabilitation programme (Anawar, 2015). The acid produced causes plant die back around waterways due to the mobilisation of phytotoxic levels of dissolved metals (Gurung et al., 2000). Among the dissolved metals can be gold and silver in either dissolved colloidal form, as a result of cyanide ore oxidation (Myagkaya et al., 2016).

Waste rock from mining sites that is high in sulfides such as pyrite typically contains enough non-oxidised and partially oxidised sulfide minerals to provide a constant supply of acidity (Gurung et al., 2000). Also present in the rock are other potentially toxic metals such as As, Ag, Cd, Cr, Cu, Hg, Ni, Pb, Sb, Th, U and Zn (Anawar, 2015). For example, zinc occurs as either sphalerite or impurities within pyrite in epithermal settings and is not controlled by the precipitation of Zn minerals, but rather accumulates, especially if mine water is recirculated. Zinc is an issue as it is one of the most common transition metals found in mine drainages. This is more of an issue in abandoned mine sites as zinc is removed as a matter of course by chemical water treatment at active sites today. Levels of zinc discharging into local water ways at abandoned sites has increased the background zinc concentrations to well above environmental protection guidelines (Pope & Trumm, 2015).

Mines in epithermal settings vary in their output of metals within mine drainage over a single deposit due to ore zone and alteration mineralogy containing varying amounts of AMD contributing minerals. These include; sulfides, silicates and carbonates (Pope & Trumm, 2015). If there is a comprehensive understanding of the trace element deportment with pyrite, then the understanding of trace elements associated with pyrite can provide access to the necessary information to produce valid predictions of what metals will be released during acid mine drainage. Recognising and monitoring the potential of a site to have issues associated with AMD can help improve planning for rehabilitation and remediation of sites all over New Zealand.

2.3 Context of Study

Epithermal systems are known for containing high grade precious metal deposits. The genesis of ore in epithermal settings is rare, and has been found globally to contain Au, As, Ag, Zn, Pb, Tl and Cu (Simmons et al., 2016). The presence of sulfides is often the first indication exploration geologists look for when assaying for precious metal deposits. Understanding whether particular mineral compositions are associated with ore deposits will be useful for predicting the existence of mineralized veins. Therefore, understanding the characteristics of pyrite associated with mineralization will give additional constraint to assay data and potential exploration sites through the interpretation of trace element analysis. Often gold and silver is not present in visible amounts at the surface, and commonly occurs as inclusions within pyrite and is referred to as invisible gold (Barker et al., 2009). A detailed study of the geology and mineral characteristics of known economic deposits can help with predictions of new, previously unknown deposits in similar settings. This is demonstrated in several studies in the section below.

2.4 Case Studies

LA-ICPMS has been used in past research to reveal gold and other trace elements in sedimentary hosted gold-arsenic deposits. Large et al. (2009) revealed two separate periods of gold enrichment within the pyrite in the four deposits studied. The study looked at the compositional zoning of the pyrite found in the sedimentary deposits, using LA-ICPMS imaging. This technique involves ablating sets of parallel lines in a grid across the sample. Every position of ablation was repeated 10 times, creating 5 consecutive pixels and an unprocessed effective resolution matching the beam size. This analysis, combined with the sweeps recorded by the mass spectrometer revealed ‘invisible’ gold (not seen in hand sample or under reflected light microscopy) concentrated in early pyrite growth, as well as other trace elements such as As, Ni, Pb, Zn, Mo, Te, V and Se. These elements, along with the gold, are thought to then be remobilised and reconcentrated in the outer growth zones of the hydrothermal pyrite. This

creates the zoning textures visible under LA-ICPMS imaging, seen in figure 2.4.1 below (Large et al., 2009).

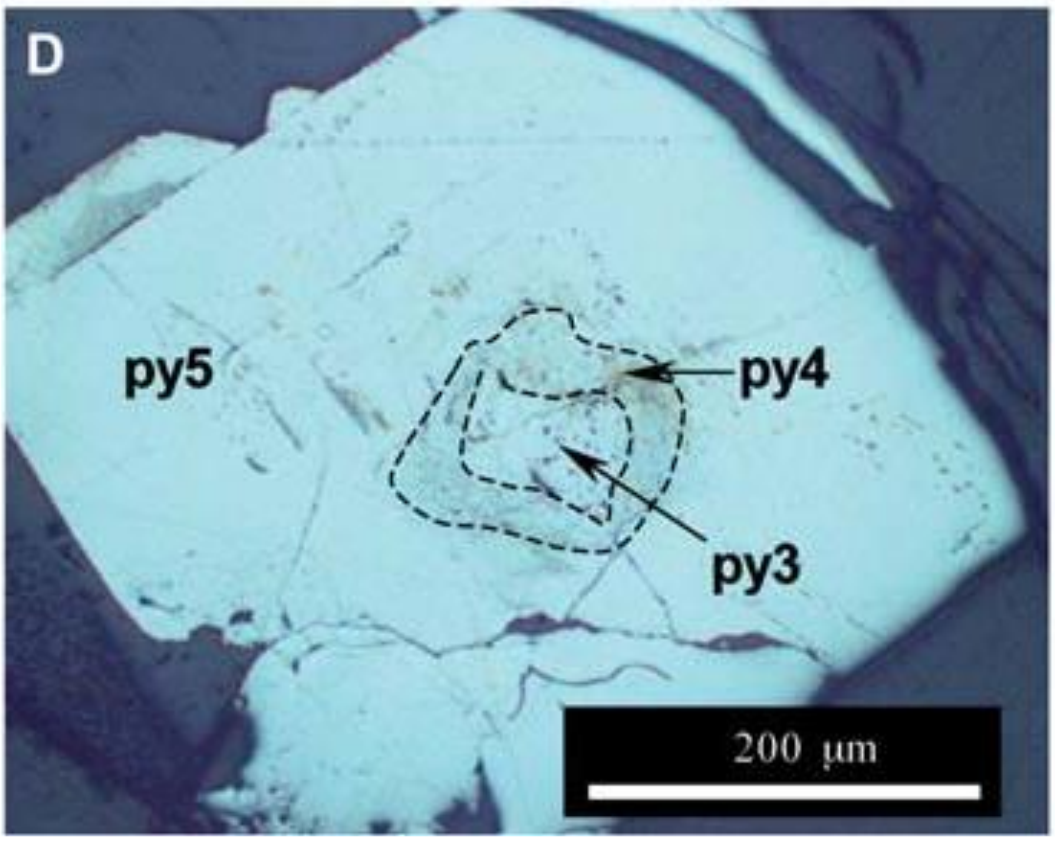

Figure 2.4.1: Zoned pyrite from Sukhoi Log gold deposit. The most inner zone is py3 (euhedral pyrite growing over framboidal pyrite), py4 is a synmetamorphic zone, py5 is the outer zone parallel to quartz vein bedding (Large et al., 2009).

The zonation found in the pyrite by Large et al. (2009) suggests a multistage process of ore genesis. The initial gold bearing fine grained diagenetic pyrite was high in trace elements, which were dissolved into the pyrite structure or dispersed as nanoparticles. During diagenesis and the early metamorphism, most of the early pyrite was then recrystallized, releasing trace elements which formed micro-inclusions. During this deformation larger euhedral pyrite crystals grew and replaced the younger, earlier metamorphic fabric. Lastly, euhedral As-Co-Ni-Se-bearing pyrite overgrew the previous two stages. The invisible gold content of the last stages is comparatively low, with the early diagenesis providing most of the gold content. Later

deformation and concentration of gold in the core of grains was caused by later deformation and hydrothermal pyrite formation (Large et al., 2009).

Thomas *et al.* (2011) looked at the compositional zoning of pyrite in gold-bearing saddle reefs, quartz veins and surrounding sedimentary rocks at Bendigo in Australia. The focus was to identify a potential source and timing of gold and arsenic related fluid processes responsible for mineralisation at Bendigo. They also used LA-ICPMS analysis to determine the changing concentrations of gold and trace elements at different zones within the pyrite. They observed that the pyrite with the thickest gold-rich rims was in closest proximity to the gold-bearing saddle reefs. The pyrite within the reef had the highest concentration of invisible gold and silver, and the lowest concentration of trace elements. Below the known gold production levels in the reef, the pyrite had been replaced by pyrrhotite during metamorphism. This pyrrhotite has similar levels of Ni and Co to the diagenetic pyrite in the reef, but is strongly depleted in gold and silver. Thomas *et al.* (2011) combined the spatial relationship between the shales, folded bedding parallel laminated quartz veins and gold-arsenic-bearing saddles and the trace element composition of the pyrite. They suggest the gold and arsenic came from the black shales, with the laminated quartz acting as a pathway for the hydrothermal fluid flow to go from the shales to the reef. This input of maximum gold and arsenic to the reefs occurred late in the deformation, towards the end of the hydrothermal cycle, and appears as Au-As-rich rims in the pyrite (Thomas et al., 2011).

Baker et al. (2006) analysed pyrite from the Pajingo deposit, a low sulfidation epithermal system. They found that the pyrite chemistry varied throughout the alteration halo of the system, with Pb decreasing overall from the hanging wall to the footwall, and Ag, Pb and Mo relationships within the pyrite changed depending on proximity to the veins. In silica-pyrite alteration, Pb/Mo ratios were less than 30, and Pb/Ag ratios were less than 10 (Baker et al., 2006).

Baker et al. (2006) also noted the occurrence of internal zoning within high As pyrite grains. This is significant, as it is one of the first documented

studies of internal zoning textures within pyrite grains from a low sulfidation epithermal system. The grain discussed showed zones of high As bands towards the outer edge of the grain, and can be seen below in figure 2.4.2.

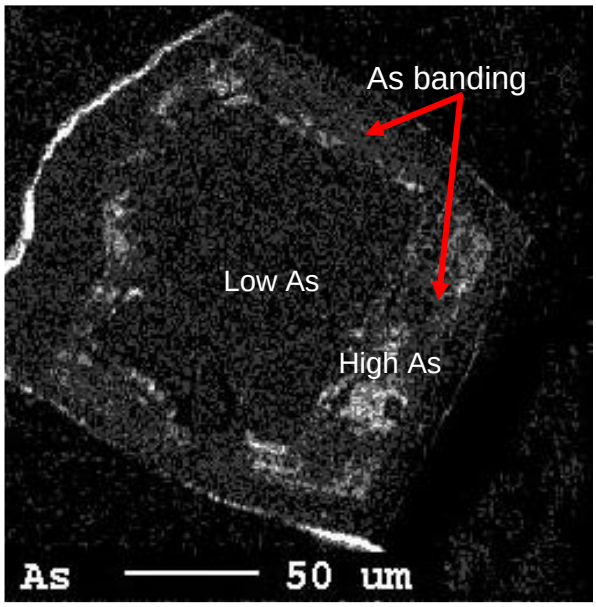

Figure 2.4.2: backscatter image of an As rich pyrite grain showing the variation in As toward the outer edge (Baker et al., 2006).

2.5 Industry Application

Geometallurgy refers to the cross-disciplinary method of combining geology and geostatistics with extractive metallurgy and subsequent processes in order to produce spatially and geologically based predictive models for use by mineral processing plants. A knowledge of the grade of valuable metals, their regional variation, the method of extraction and overall concentration is required to build a complete working model for subsequent mining. For a geometallurgical programme, samples of a wide variety and range of sizes need to be analysed, in order to make prediction models as accurate as possible (Parian et al., 2015). Geometallurgy has become an essential practise in mining sites all over the world. For example, Australian uranium mine planning and processes are being designed based on several geometallurgical studies aimed at heightening the mine's exploitation and profit potential (Pownceby & Johnson, 2014). Another example is the use of

geometallurgy of copper-gold-molybdenum deposits in Alaska in one of the world's largest porphyry deposits. In this study, regions of constant hydrothermal alteration, sulfide mineralogy and gold deportment provide the information to create the mineral processing model. Geometallurgy is becoming more widespread in its use and is increasingly applied routinely in the exploration industry, being best utilised in the advanced exploration stage prior to ore mining commencement (Gregory et al., 2013). A greater understanding of the chemistry of pyrite and other ubiquitous sulfide minerals is important. Increasing the understanding of how sulfides behave in certain mining and rehabilitation conditions will provide the necessary information to further increase the efficiency of mining, as well as increasing environmental safety.

2.6 Conclusion

Pyrite in epithermal settings is of interest for environmentalists, exploration geologists and in the practise of geometallurgy. Pyrite has the useful characteristic of allowing the incorporation of trace elements within grains. This makes pyrite valuable for the reconstruction of gold precipitation stages and paleofluid chemistry in epithermal settings today. Studies in Australia have demonstrated that the examination of pyrite zones can provide enough information to reconstruct the system's history of gold production. Taking all this into consideration, several questions can be posed about the textures and chemistry of pyrite in the epithermal setting at Waihi.

Knowing that Waihi is a low sulfidation epithermal system, and that zoning in such systems is yet to be documented, the first question is, is there any zoning in the pyrite grains found in the main, gold-bearing vein structures? Secondly, where in the pyrite does the gold and silver mostly occur, and what other trace elements occur with it, and, with this data can controls on gold and silver concentration in the pyrite be determined? And finally; what does pyrite zoning mean for future mining potential and environmental management?

3. Geological Setting

3.1 Regional Geology

The Coromandel Volcanic Zone (CVZ) was last active 5-7 million years ago. It is a NNW belt of andesites, dacites and rhyolite rocks of Miocene to Pliocene age (Brathwaite & Blattner, 1995). This sits on top of a basement of lithic-volcanic greywacke of Jurassic age (Christie et al., 2007). The volcanic rocks young to the south, the southernmost merging with, and underlying, rocks from the Taupo volcanic zone of Quaternary age (Brathwaite & Faure, 2002). The CVZ hosts the Hauraki goldfield, which comprises around 50 epithermal Au-Ag deposits (Simpson et al., 2001). These deposits are quartz ± calcite ± adularia ± illite type (i.e. low sulfidation) (Christie et al., 2007).

The Hauraki goldfield is hosted mainly in the andesites and dacites of the Coromandel Group, with small areas of mineralisation in the Whitianga Group rhyolites and basement greywackes (Christie et al., 2007). Throughout the CVZ, ore is typically hosted in quartz veins that have formed within tensional fault-fracture structures (Brathwaite & Blattner, 1995). The main ore forming minerals associated with the CVZ are electrum, and acanthite (mostly associated with pyrite, chalcopyrite and galena) (Christie et al., 2007). Most of these ore deposits are less than 200 m below current land surface. The land surface is known as Relative Level (RL). Waihi and Karangahake reach 575-700 m below RL. In these two deeper deposits the electrum is associated with Zn-Pb-Fe-Cu-Ag sulfides, which transitions at depth to Zn-Pb-Fe sulfide assemblages with little electrum present (Brathwaite & Faure, 2002).

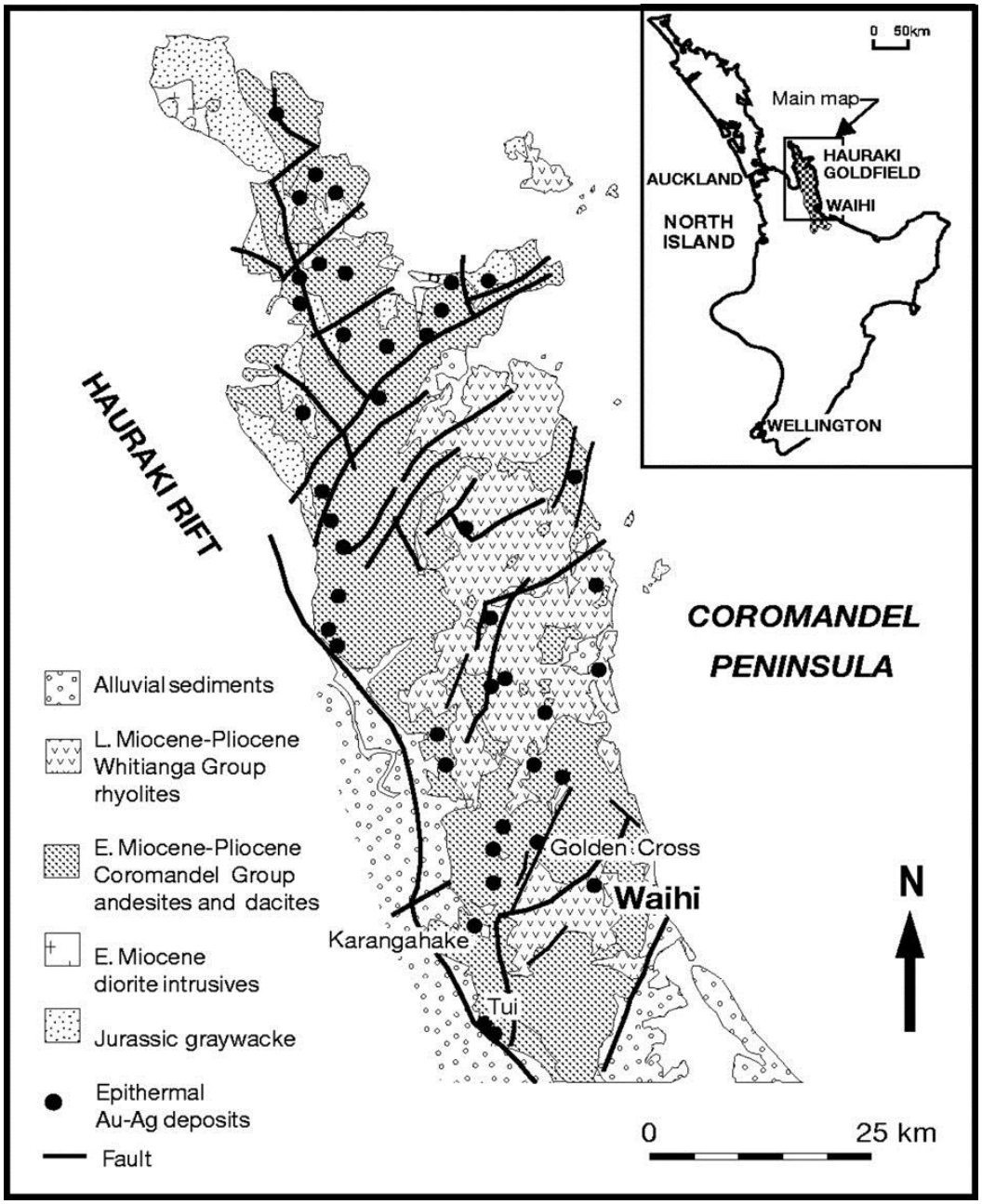

Figure 3.1.1: The Hauraki Goldfield, with black circles indicating locations of epithermal Au-Ag deposits. Inset figure of location of the Hauraki Goldfield in the North Island, New Zealand (Brathwaite & Faure, 2002).

3.2 Local Geology

The Waihi epithermal system is a gold-silver-base metal sulfide-quartz vein system (Brathwaite & Faure, 2002). The system is hosted in andesites and dacites of the Coromandel Group, along with Whitianga Group rhyolites and basement graywackes in some places (Christie et al., 2007). The geology of the area can be seen in figure 3.2.1 with the areas of concentrated mining shown to be in the altered andesite**.** The andesite host rock is unconformably overlain to the East of Waihi by an unaltered hornblende dacite of late Miocene to early Pliocene age, as shown in figure 3.2.1. The main rock type is a plagioclase-porphyritic two-pyroxene andesite containing prominent but minor quartz phenocrysts in lower parts of the sequence (Christie et al., 2007). The unaltered andesite at Waihi contains phenocrysts of plagioclase, augite, hypersthene, minor quartz and local hornblende, with additional magnetite, apatite and zircon (Brathwaite & Blattner, 1995). The main ore minerals of the quartz vein systems include electrum and acanthite (commonly associated with pyrite, sphalerite, galena and chalcopyrite) (Brathwaite & Faure, 2002).

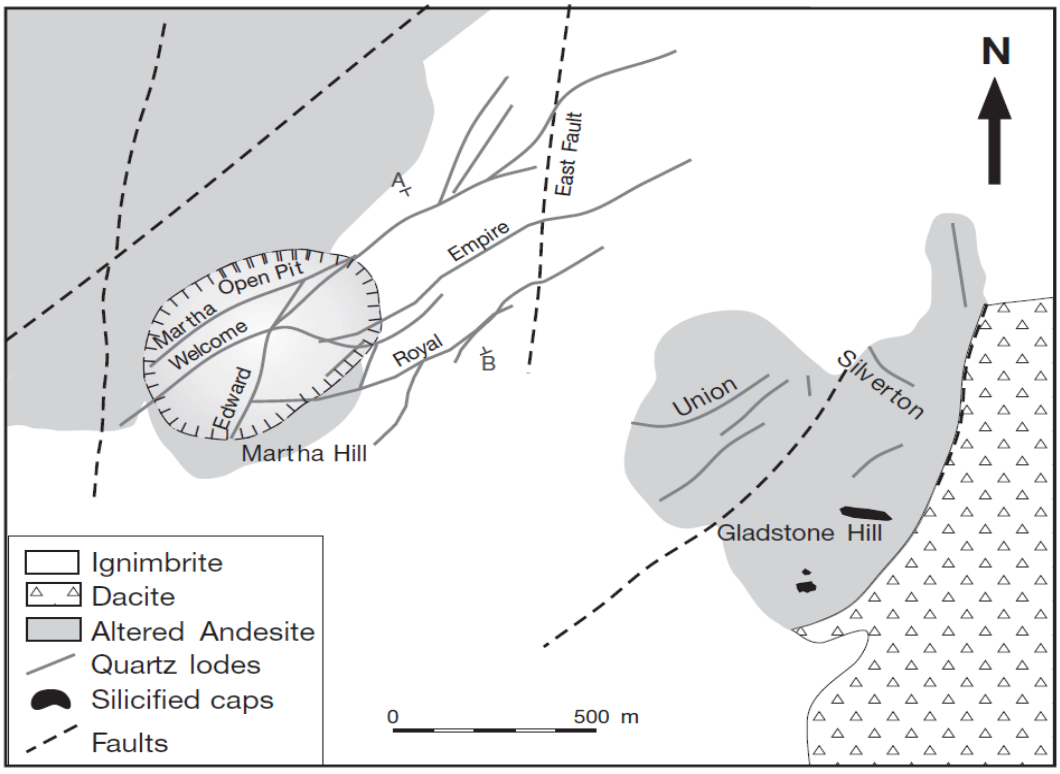

Figure 3.2.1: Map of the local Waihi geology. Quartz lodes have been projected on the surface for ease of visibility (Brathwaite & Faure, 2002).

Previous studies on fluid inclusion data from the Golden Cross, Karangahake and Tui deposits suggest that the base metal sulfides were deposited from fluids at high temperatures (260°C-320°C) and a salinity of 1.7-6 wt% NaCl equivalent, comparatively higher than the electrum bearing sulfide ore, which was deposited between 190°C-260°C (Brathwaite & Faure, 2002). The Waihi alteration structure indicates how the hydrothermal activity affected the local area and is outlined in figure 3.2.2**.** Three alteration zones are apparent in the Waihi system. (1) a smectite zone composed of smectite-chlorite-calcite-pyrite, (2) an interlayered illite-smectite zone, and (3) an illite zone with adularia-quartz-illite subzone, adjacent to the quartz lodes (Christie et al., 2001). In the least altered zone (1), magnetite is altered to pyrite + titanite. With increasing intensity of alteration, the plagioclase is altered to chlorite + calcite + pyrite, which occurs mostly in the upper part of the vein system on the hanging wall of the Martha lode, especially to the eastern end of the deposit (Brathwaite & Faure, 2002). In zone (2), which is more altered, the magnetite is replaced by pyrite + titanite. In the zone of strongest alteration, the groundmass of the rock consists of mosaic quartz, illite, minor interlayered illite-smectite and disseminated pyrite. The location of each of these zones can be seen in figure 3.2.2 below, where the smectite zone is directly beneath the ignimbrite. The illite-smectite zone lies near horizontal with the illite zone below at the same orientation.

The Martha deposit, which is the focus of this study, is located in the northwest of the Waihi vein system. Within the Martha deposit, the mineralogical zonation is influenced by paleo-depth, with electrum levels decreasing with depth, while sulfide minerals become more abundant. There is an increase of electrum and base metal sulfide assemblages, along with acanthite and quartz, at shallower levels in the Martha vein system (Fyfe, 2014). The distribution of gold in the central vein system at Waihi is complex and not yet fully understood (Fyfe, 2014).

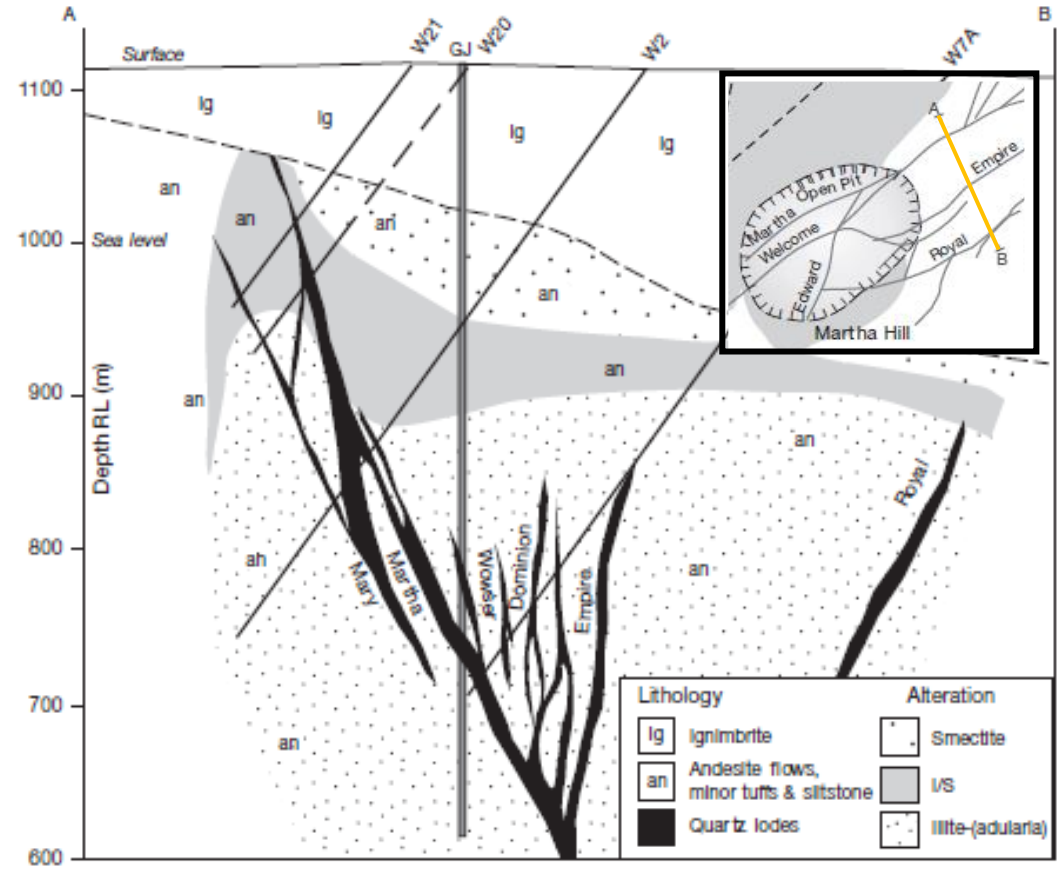

Figure 3.2.2: Cross section (A-B) of the Waihi Vein system with main lithologies and alteration zones. Inset image shows location of the cross section A-B. I/S is the medial illite-smectite zone. Location of drill holes W21, W20, W2 and W7A are noted (adapted from Brathwaite & Faure, 2002).

The vein mineralisation at Waihi consists of multiple vein phases filled with microcrystalline- to medium-grained quartz and quartz vein breccias (Brathwaite & Faure, 2002). The quartz can be divided into main stage quartz (including the sulfides) and a late stage of amethyst (Brathwaite & Blattner, 1995). Pyrite, sphalerite, galena, chalcopyrite, and acanthite occur mostly in the form of sulfide bearing bands in fine to medium grained quartz (Brathwaite & Faure, 2002). Microcrystalline colloform quartz comprises most of the shallow vein fill. It occurs as colloform and crustiform bands. The colloform quartz contains minor pyrite, sphalerite, chalcopyrite, tetrahedrite, acanthite, and electrum. Deeper, the colloform quartz grades to crustiform comb quartz and sulfides (Christie et al., 2001). Fine grained quartz and sulfide bands have colloform textures with comb quartz lining

vugs also common. Crustiform veins are interbanded with hydrothermal breccias made up of angular vein quartz, or wall rock fragments. These are in a fine-grained matrix with quartz and sulfides with cockade overgrowth common around the fragments.

Below 700m RL, fibrous chlorite in either discontinuous bands or radial aggregates occurs with the quartz in the sulfide bands (Brathwaite & Faure, 2002). Bladed or platy calcite is found with the quartz locally, but is absent in metal sulfide and electrum bearing bands (Christie et al., 2001). Commonly, quartz has replaced the calcite and deposited on remnant calcite blades, resulting in the characteristic lattice texture of quartz pseudomorph after calcite. This is common in the Martha lode below 700m RL (Brathwaite & Faure, 2002).

The fluids present during the hydrothermal activity at Waihi are thought to be from deep chloride fluid with steam-heated meteoric water $\delta^{18}O_{water}$ levels at around -5‰ relative to the Vienna Standard Mean Ocean Water (VSMOW) (Brathwaite & Faure, 2002). The deep water compositions suggest that redox conditions within the system are constrained by the equilibria between pyrite and Fe chlorite. Some of the reduced waters corresponds to pyrite-pyrrhotite equilibria and this is attributed to local incorporation of steam with relatively high H_2/H_2S ratios (Simmons & Browne, 2000).

The Waihi epithermal system had three stages of evolution. The first stage was an initial vein filling with platy calcite, quartz, pyrite and adularia. This is associated with the alteration of the andesite wall rock. The second stage is a main stage of vein filling by quartz and sulfides, with or without electrum. The final stage is of vein deposition by minor amethyst. The wall rock alteration associated with the first stage is characterised by a proximal mineral assemblage of adularia + quartz + pyrite (Brathwaite & Faure, 2002).

4. Methods

4.1 Sampling

The samples in this study are described in the thesis from Fyfe (2014) and are from the Auckland University collection and PetLab collection at GNS. sampling for the Fyfe study was done from drill cores from the Waihi mine, formerly owned by Newmont, and as of October 30 2015 owned by Oceana Gold. Samples were chosen from the collections based on their sulfide content, and the presence of pyrite grains identified in their descriptions. The descriptions are detailed in tables 4.1.1 and 4.1.2 below. The location of the samples was constrained to the Martha deposit as those had the highest sulfide levels of any vein system, and the Martha Vein is the largest of all the veins in the Waihi system. The precise locations of samples can be seen in figure 4.1.1 below. A full sample list can be found in Appendix I.

One sample (AU60281) was chosen as a comparison between vein systems and is from Cowshed, not Martha.

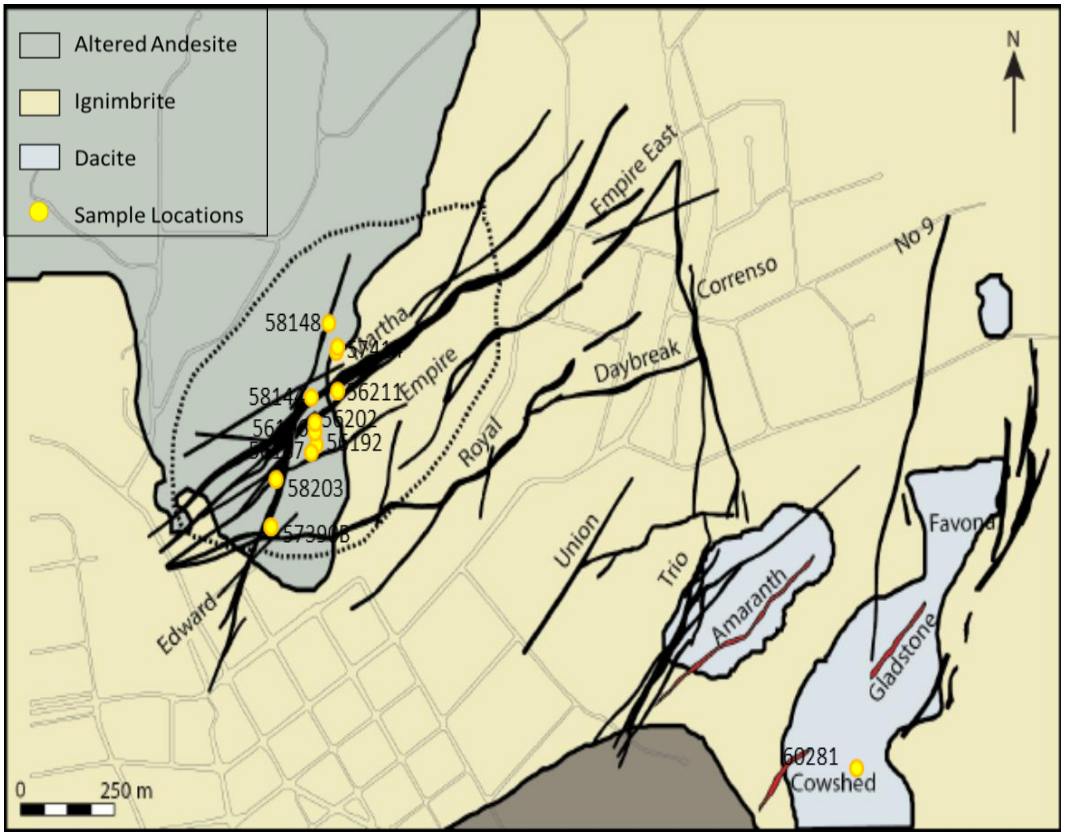

Figure 4.1.1: Map showing the locations and geology in the sampling area (adapted from Fyfe, 2014).

Based on the work done by Fyfe (2014), samples were selected from the University of Auckland collection in the form of 1 inch epoxy mounts. The selection of these was based on their location (within the Martha deposit) and their rock description (common sulfides). Examples of the mounts can be seen in figure 4.1.2 below. In sample AU58203 there are visible sulfides and visible gold.

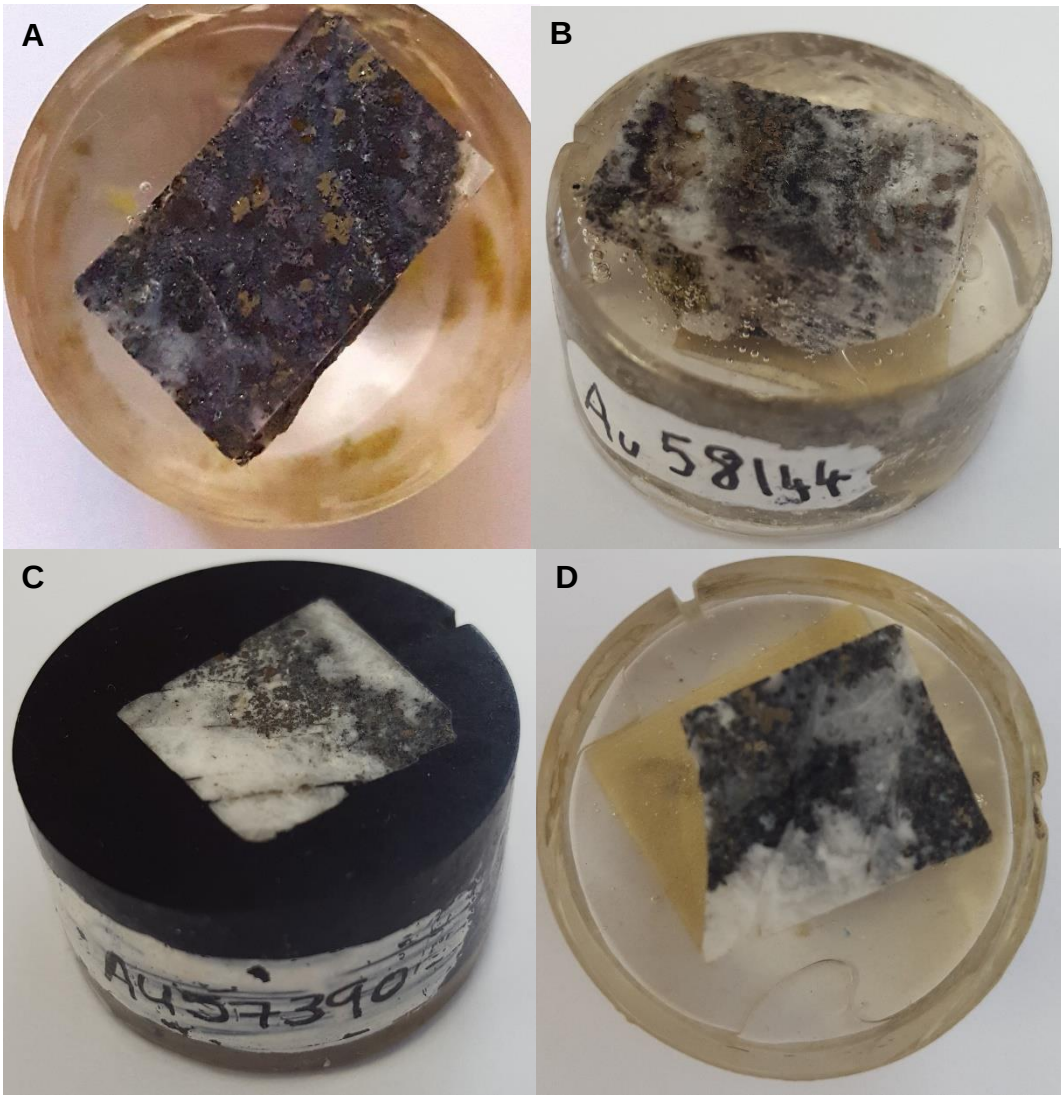

Figure 4.1.2: example of the 1 inch epoxy mounts. A: AU58203, B: AU58144, C: AU57390B and D: AU57390. A, B and C all have visible sulfides.

Samples were also obtained using the PetLab database run by GNS. Samples were hand sample and thin section in form. Examples of these can be seen below in figure 4.1.3. These samples were selected based on their location (Martha vein) and their high sulfide content.

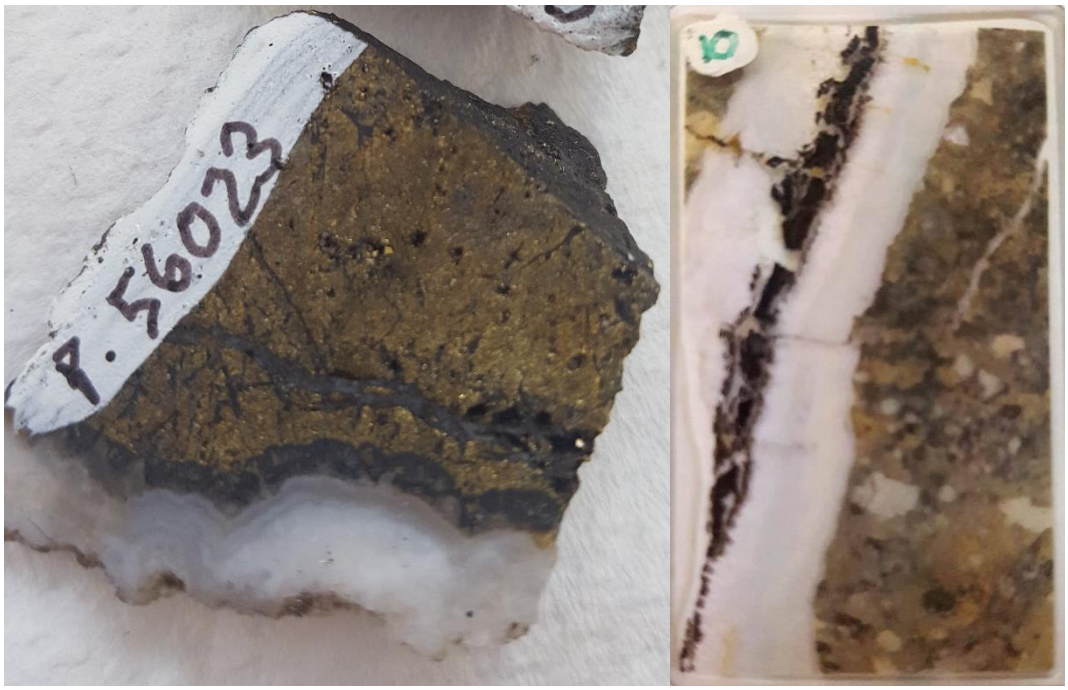

Figure 4.1.3: examples of hand sample (P56023) on the left and thin section (WDH9_169.5) on the right. Both found through PetLab and are from Brathwaite (1982).

Table 4.1.1: Mineral assemblages of samples, adapted from Fyfe (2014).

Sample Number	Depth (m RL)	Easting	Northing	Mineral Assemblage
AU56192	940	395452	643087	some pyrite, few sphalerite grains, quartz vein with alteration on edge. No pyrite in altered zone.
AU56196	940	395448	643096	common pyrite in large clusters, elongate grouping, few tiny sphalerite grains, quartz vein with sulfide mixed in.
AU56202	0	395451	643102	some large pyrite grains, few tiny sphalerite and chalcopyrite grains, suggested order chalc-sphalerite-pyrite, in sulfide band of quartz.
AU56211	950	395527	643123	few large pyrite grains, some small sphalerite and chalcopyrite, suggested order chalc-sphalerite-pyrite, quartz vein with sulfide band.
AU56187	940	395438	643082	HAND SAMPLE thin sulfide band in light blue grey rock with yellow tinge.
AU57390	942.5	395295	643033	common large pyrite, common small sphalerite and chalcopyrite, suggested order chalc-sphalerite-pyrite, quartz vein with sulfide band.
AU57390B	942.5	395295	643033	few large pyrite grains, common small to tiny sphalerite and chalcopyrite grains, suggested order chalc-sphalerite-pyrite, quartz vein with sulfide vein through.
AU57414	935	395523	643149	some medium pyrite grains, few small sphalerite grains, sulfide band with oxidised rock on either side.
AU57417	952	395529	643152	common pyrite in large clusters, elongate grouping, sulfide vein in light grey rock (possibly quartz) on edge of vein.
AU58144	927.5	395437	643119	few large pyrite grains, rare sphalerite grains and covellite replacement of chalcopyrite, quartz vein with sulfide band.
AU58148	927.5	395498	643168	some large pyrite grains, few medium sphalerite grains, suggested order sphalerite-pyrite, edge of quartz vein with sulfide band.
AU58203	945	395314	643065	few large pyrite, some galena, chalcopyrite and sphalerite and possibly native gold and silver, whole sample made up of sulfides.
AU60281	830	397351	642873	few small pyrite grains, rare tiny sphalerite grains, quartz vein with thin sulfide band through the middle.

Table 4.1.2: Sample descriptions, adapted from Fyfe (2014).

Sample Number	Depth (m RL)	Easting	Northing	Description
AU56192	940	395452	643087	Quartz vein with brecciated green coloured wall rock and dark sulfide bands. The brecciated wall rock is intensely altered. Sulfides minerals occur in dark crustiform bands.
AU56196	940	395448	643096	The rock is a moderately altered andesite- vein breccia. The matrix is comprised of massive quartz with disrupted sulfide rich bands containing high-grade mineralisation.
AU56202	0	395451	643102	vein breccia; clasts are infilled by massive quartz. Sulfide clots contain high-grade mineralisation. Vugs containing drusy quartz also occur in the sample.
AU56211	950	395527	643123	Consists of crustiform-colloform banded white-grey quartz. Visible gold occurs in sulfide rich bands.
AU56187	940	395438	643082	Multi-coloured, highly altered, clast supported polymict vein breccia. Clasts are sub-angular and are <3cm in size (85% of rock). Quartz veins are largely colloform.
AU57390	942.5	395295	643033	Veins consist of colloform banded green clay-sulfides, which are cross cut by fine colloform banded quartz veins.
AU57390B	942.5	395295	643033	Veins consist of colloform banded green clay-sulfides, which are cross cut by fine colloform banded quartz veins.
AU57414	935	395523	643149	Wall-rock and vein sample, that contains localised sulfide pods and bands. These are crosscut by colloform white quartz.
AU57417	952	395529	643152	Sample contains altered host rock that is cross cut by colloform and crustiform banded veinlets.
AU58144	927.5	395437	643119	The sample is comprised of massive drusy quartz that is cross cut a discontinuous ginguro band with visible gold and a quartz/light green clay band.
AU58148	927.5	395498	643168	Pervasively altered host rock sample, which is cross-cut by pyrite stringer veins and colloform -base metal sulfide bands.
AU58203	945	395314	643065	The sample is a large vein that contains thick ginguro bands (3 cm) with visible gold, these cross-cut massive white quartz.
AU60281	830	397351	642873	Crustiform banded amethyst quartz, in filled by fine-grained milky quartz that contains sulfide blebs.

4.2 Bleach Etching Method

This method was used to encourage oxidation of the surface of the samples, with the aim to reveal textural information due to variation in oxidation rate caused by variable trace element content of the pyrite, similar to etching previously by Large et al. (2007). This created the zoning visible under reflected light microscopy. Before they were etched, images were taken of the pyrite as reference for the amount of change after etching. A small amount of 5% sodium hyperchlorite (NaOCl) was deposited onto the sample surface with an eye dropper. Care was taken to ensure the dropper did not touch the surface of the sample. The entire surface was covered to ensure all pyrite grains were affected. The NaOCl was left on the samples until a colour change from brassy gold to bronze was observed. This took around 1 minute 40 seconds. A test run was done to check that the bleach wasn't being left on for too long. This would cause the pyrite grains to adopt a "peacock tail" rainbow on the surface, obscuring any variations in oxidation that would otherwise be seen. The samples were then run under a cold water tap for 45 seconds and then left to air dry, being careful not to touch the surface and rub off the oxidised layer. Once dried, the samples were observed under reflected light microscopy. Images were taken by camera of the varying pyrite textures. An example of these from AU57390 can be seen in figure 4.2.1 below.

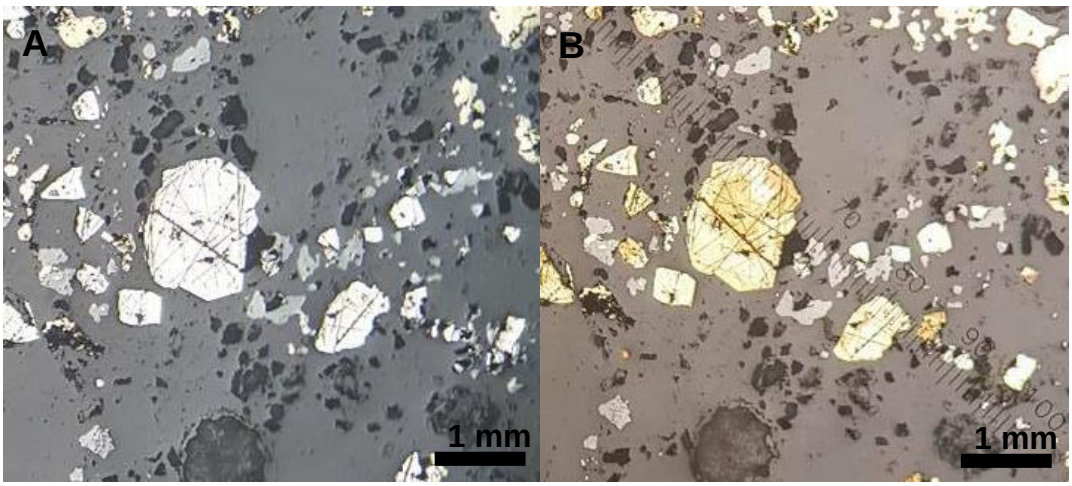

Figure 4.2.1: A – sample AU57390 before etch. B – same area on sample AU57390 after bleach etching.

4.3 XFM Analysis

Two samples were analysed using the X-ray fluorescence microscopy (XFM) beamline at the Australian Synchrotron facility in Melbourne. Sulfide bands on the edge of quartz veins were identified in two hand sample specimens and prepared on 100 µm quartz glass slides for analysis under the XFM beam. Attention was paid to the distribution of Fe, As, S, Au, Ag and Zn within the sulfides.

Scanning X-ray fluorescence microscopy combined with synchrotron radiation is an effective technique for rare phase detection. This is due to the nature of synchrotron radiation and its penetrating power, resulting in the ability to image small grains (in µm) within a sample, as opposed to intersecting a surface. The use of the synchrotron increases the chance of intersecting rare phases in samples by ~70 times, compared to conventional 2D techniques ie. SEM (Barnes et al., 2015).

The XFM beamline, located at the Australian Synchrotron, uses the Kirkpatrick-Baez mirror microprobe end-station, providing a monochromatic 2 µm beam spot size, with energies from 4-20 keV. Used in conjunction with a Maia 384 detector array, the beamline acquires full spectral X-ray data over several square centimetres in area, at step sizes as low as 2 µm, with count rates at ~4-10 M/s and energy resolution of 240-400 eV. This data, once processed (real-time or offline) produces quantitative, multi-element images, with up to 100 M pixels (Fisher et al., 2015).

The Maia 384 detector identifies all elements during peak fitting of the spectra during processing. As the beam makes contact with the sample surface, energy is reflected back to the detectors. The amount of energy reflected back depends on the elemental composition of the sample area the beam hits at that moment. Each element has a different energy, and on this basis the Maia 384 detectors identify the different elements (Dyl et al., 2014). This is the principle of X-ray Fluorescence (XRF). The length of dwell time increases the accuracy of the data produced. Detection limits of 10-100s of ppm can be achieved with dwell times of <1 ms.

The Dynamic Analysis (DA) matrix is a transform method that generates real-time quantitative elemental images. This is used in conjunction with the XFM to monitor the progress of the Maia 384 detectors while analysis is underway. DA builds a matrix transform mapping the spectrum vector onto the concentration vector, with reference to the integrated beam charge or fluence at that instant. In real-time imaging, each event isolates a column of the DA matrix containing increments, making each elemental image. This results in the accumulation of images in ppm-fluence units (Ryan et al., 2005).

For the sulfide samples analysed, first an overview sweep with dwell times optimised to allow sufficient count rate data yet allow a map to be generated in a reasonable period of time and energy set at 18.5 KeV. Once areas of interest were identified, using the overview images, the area size was decreased to the specific area of interest, and the dwell time to <1 ms to increase the quality of the data in the areas of importance.

4.3.1 Data Reduction

Once the data was produced, the GeoPIXE program for data reduction was used. GeoPIXE uses the fundamental parameter model for the layered sample, the Maia 384 detector array efficiency model, and the DA matrix method, to deconvolute the spectra. For all sulfide samples the thickness of 100 µm was determined as that was the size of the quartz slide. The standard composition expected was set as pyrite with the formula FeS_2, with the layer of quartz glass slide at 100 µm. The program GeoPIXE allows for the adjusted fitting of the Compton scatter peaks manually, to cope with any issues of energy overlap between elements (Ryan et al., 2015).

There is an issue of secondary fluorescence in the lighter elements due to their ability to reflect. However, while this has the potential to increase the analysis volume for those elements in question, it appears to have a minor effect, which is insignificant compared to other sources of error mentioned below (Dyl et al., 2014).

Fe pile-up is a difficulty associated with analysis of high Fe samples such as sulfides. This produces artificial peaks in Fe rich areas. As the samples were predominantly sulfide, the appearance of artificial peaks was taken into account when manually adjusting the Compton tail. There was also the issue of element overlap, which occurs between elements such as X and Y. This needed to be taken into consideration also, when manually adjusting the fit.

4.4 EPMA Analysis Method

Nine individual round 1 inch epoxy mounts were analysed. The pyrite grains with identified zoning were analysed on the JEOL JXA-8230 SuperProbe Electron Probe Microanalyser at Victoria University of Wellington. The analyses were done using a 1µm spot on different spots within various textural zones for 8 minutes per spot. The instrument was calibrated using an Elba pyrite standard for Fe and S, and various pure metals for the other elements to define peak and background positions. The Virtual WDS software (Cambridge) was used for determining optimal crystal and peak positions to avoid elemental overlaps and optimise analysis times. The specific elements selected for analysis were Bi, Au, W, Mo, Fe, As, Si, Zn, Co, Cu, Se, Pb, Sn, V, Ca, Sb, Te, Ni, Hg, Ag and S. The data was obtained at 20 KV and 10 nA for major elements, and 100 beam current nA for trace elements, with detection limits as low as ~ 50 ppm for some elements. The lack of appropriate microanalytical standards for sulfide minerals makes independent assessment of detection limits or data quality difficult.

Electron microprobe analysis works on the principle that exciting the sample with a beam of electrons results in the reflection of energy from the sample. The amount of energy reflected depends on the elemental composition of the sample surface. This method of analysis is more commonly used for the major elements in minerals, but can be used in fused whole rock samples also. The electron microprobe has high quality spatial resolution, with the electron beam typically between 1 to 2 µm in diameter. Although the electron microprobe is generally used for major elements, trace element analysis can be practised by using long counting times and precise background measurements. This extends the detection limits for trace elements, allowing the producing of usable data (Rollinson, 1993).

4.4.1 Data Reduction

The program ioGAS was used as a means of data analysis. The software allows the interpretation of large amounts of geochemical data by providing means of creating XY plots of element concentration, rare earth element (REE) maps, data plotted in easting, northing and elevation and other geologically specific analyses such as mineral assemblages within samples. The program allows for the manual identification and deletion of outliers, and provides the user with the tools to quickly identify chemical trends in data based on previous theories about the specific samples studied (Lawie & Paraschivoiu, 2009).

4.5 LA-ICPMS Analysis

Trace element analysis was undertaken using the laser ablation system; Laser Ablation Inductively Coupled Plasma Mass Spectrometry (LA-ICPMS), at the University of Waikato. Ablation was carried out using an Australian Scientific Instruments (formerly Resonetics) 193 nm SE-155 laser ablation system, coupled to a Perkin Elmer Elan ICPMS. Analysis was carried out on whole grains using a rastering technique utilising a 30µm spot traversing at 15 µm per second, and relatively low laser fluence (4 J cm^{-2}), and forming element maps with a resolution of ~ 30 µm, showing element concentration over the grain surface. For each image the elements analysed were ^{54}Fe, ^{57}Fe, ^{51}V, ^{52}Cr, ^{59}Co, ^{63}Cu, ^{66}Zn, ^{69}Ga, ^{75}As, ^{77}Se, ^{95}Mo, ^{107}Ag, ^{111}Cd, ^{118}Sn, ^{121}Sb, ^{126}Te, ^{182}W, ^{197}Au, ^{205}Tl, ^{208}Pb and ^{209}Bi. Ablated material was swept to the ICPMS using Helium in the ablation cell which was then blended with Ar in the sampling cone. The data was then analysed using Iolite software, creating cellspace maps to show the spatial distribution of specified elements within grains of interest (Paton et al., 2011; Paul et al., 2012). NIST610 was analysed in raster mode before and after maps in order to correct for instrument drift.

5. Pyrite Textures

5.1 Pyrite Textures in the Martha Deposit, Waihi Epithermal System

Samples containing pyrite grains from the Martha vein system, found in the Waihi deposit, were observed under reflected light microscopy and etched with NaOCl. A classification system was developed to describe the primary textural features and colour variations observed in the bleach etched pyrite samples from the Martha vein system. Three primary textural zoning classifications have been made: zoning occurrence; zoning type and; zoning shape. The textural variations within each of these groups are discussed below and include subcategories based on the presence/absence of inclusions.

5.1.1Classification Scheme

Zoning Occurrence

Inter grain: There are distinct colour variations between individual grains of pyrite in a single thin section (Figure 5.1.1.1).

Intra grain: colour/texture varies within a single grain, see figure 5.1.1.1.

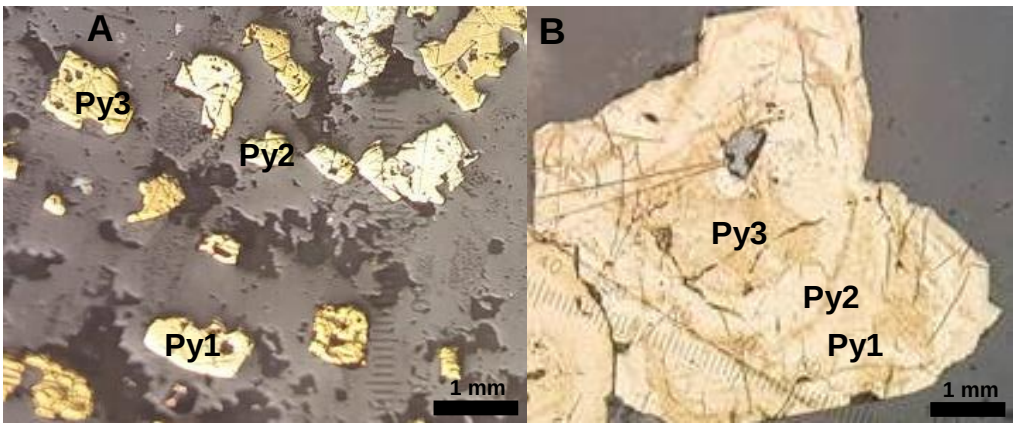

Figure 5.1.1.1: A – inter grain zoning in pyrite from AU57417. Zones have been labelled Py1 to Py3 based on relative shading within each grain; Py1 is palest, Py3 is darkest. B – intra grain zoning in pyrite from AU56192_Z2 with zones Py1, Py2 and Py3 within single grain.

Zoning Type

Clean: sharp edges of clearly visible colour change between zones, see figure 5.1.1.2.

Dirty: indistinct a diffuse or irregular transition between zones, making zone boundaries difficult to define. See figure 5.1.1.2.

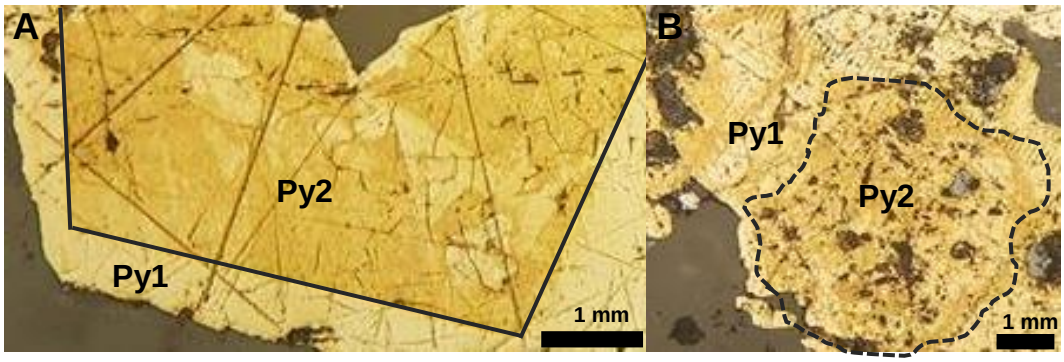

Figure 5.1.1.2: A – example of a clean boundary between Py1 and Py2 from sample AU57390B_Z1. The solid black line indicating where the boundary occurs. B – example of dirty boundaries between Py1 and Py2 in sample AU56196_Z2. The black dashed line indicates a possible boundary.

Zoning Shape

Radial: pattern inside grain is similar to a tree ring form, multiple bands of varied colour that roughly follow the grain's geometry, spreading outwards from the grain's centre. See figure 5.1.1.3 for an example of radial zoning shape.

Figure 5.1.1.3: example of the radial zoning shape in sample AU58148_Z2.

Planar: The colour varies within a grain, but the grains appear anhedral, resulting in any relationship between the zonations and crystal faces to be

obscured. Zones do not follow the radial pattern as seen above. Figure 5.1.1.4 shows an example of planar zoning. The inner pale zone can be seen stretching along the length of the grain, while the top and bottom of the grain are of a different zone, referred to as Py2 in figure 5.1.1.4 below.

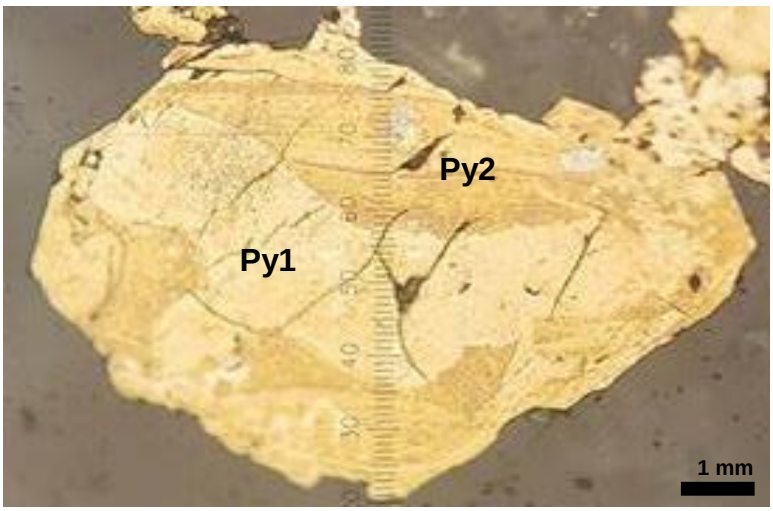

Figure 5.1.1.4: example of planar zoning in sample AU58144_Z1. Where zone Py1 does not extend radially from the grains centre.

5.2 Classification of samples

Here the samples examined have been grouped based on their textural characteristics. Grains observed under reflected light after etching were separated into categories based initially on the zoning shape, as this is the most visually defining characteristic. Subcategories were added to accommodate variations such as inclusion textures, dissolution features and the number of zones. The subsequent groups are named in such order; zoning occurrence, zoning type, zoning shape, and are explained in greater detail below. Inter grain zoning is briefly discussed, followed by a summary of the types of intra grain zoning in table 5.2.1.1. The types of intra grain zoning are then further explained in greater detail below.

Inter grain

Grains in this group display no internal zoning textures. A number of samples including AU57417, AU56202, AU56211 and AU60281 displayed both visible and no visible zoning within individual grains. The etched mounts display pyrite grains with (at least) three distinct colour variations, labelled Py1, Py2 and Py3 in figure 5.2.1.1. The pyrites in these samples are (internally) homogeneous, with no obvious textures or zoning patterns. The collection of samples that fall into the inter grain classification are a mix of wall rock and vein rock, with AU60281 being the only sample to occur outside of the Martha deposit. Pyrite in these samples is in the same size range as the pyrite grains found to have internal zoning characteristics.

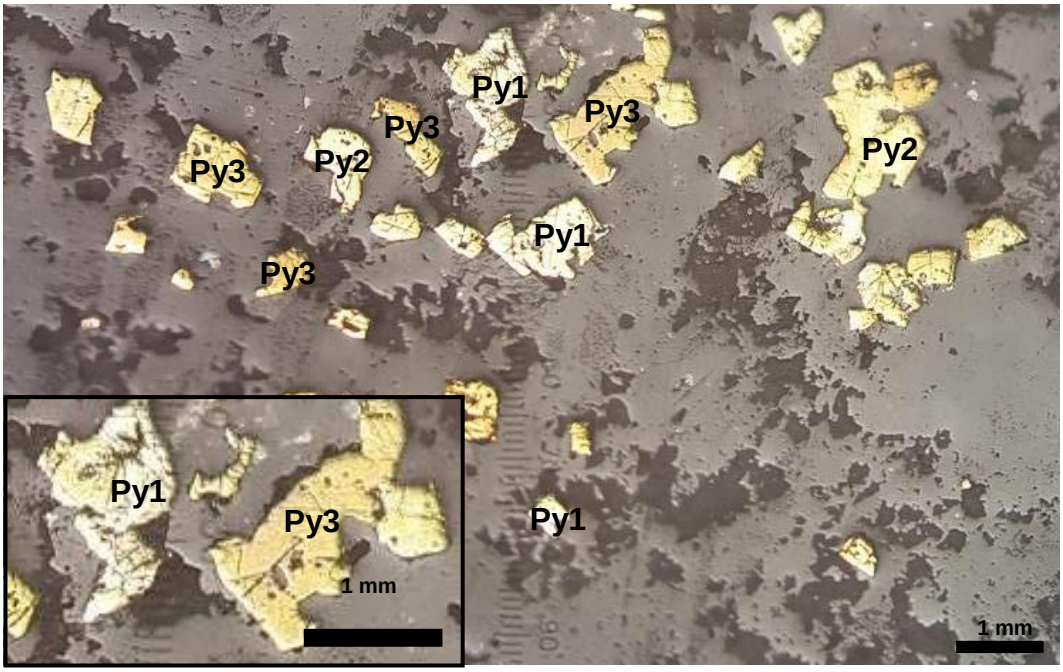

Figure 5.2.1.1: pyrite from AU57417 showing inter grain variation. Different shades have been labelled Py1 to Py3 based on colour; Py1 is palest, Py3 is darkest.

Table 5.2.1.1: Results of the bleach etching showing the different types of intra grain zoning.

Zoning Type	Main Characteristics	Example
Intra, Clean, Radial (ICR)	Grains in this group display a tree ring like zoning pattern. Each zonation is sharply defined, straight (no jagged or wavy edges) and parallel with the crystal faces of the grain. Grains of this group are generally the larger grains in the sample, and are around 300µm. Figure (a) shows the best example of this type of zoning.	 Figure (a): An example of ICR zoning from sample AU58148 after bleach etching.
Intra, Dirty, Radial (IDR)	These grains are similar in appearance to the ICR group grains however, the zonations are wider (ie. there are fewer zones) and the edges of each zonation are more diffuse, making them more difficult to define. Within each band there may also be some pitted textures that give the grain a dirty appearance. Figure (b) shows an example of the 'dirty' textures.	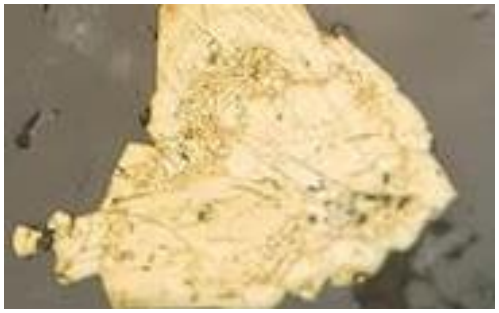 Figure (b): An example of IDR zoning from sample AU56192 after bleach etching.
Intra, Clean, Radial, Bordered (ICRB)	These grains have the same characteristics as the ICR grains. The zoning in this group is limited to two distinct zones, creating a border appearance. The border follows the inner shape of the grain, with the outer grain edge is sometimes parallel, but often displays poor formation of crystal faces. Figure (c) shows the single colour change in the grain, creating the lighter, 'border' around the edge.	 Figure (c): An example of ICRB zoning from sample AU57390B after bleach etching.

Table 5.2.1.1: Continued.

Intra, Clean, Planar (ICP)	The grains in this group have clearly defined zones of differing colour that are not the same shape as the grain itself suggesting new pyrite growth around a pre-existing pyrite grain. Often these zone textures apply to one side of a grain or have an apparently random occurrence. These grains are similar in size to the IDR and ICR. Figure (d) shows the clear defined edge of the colour zones and how they do not follow the grain geometry.	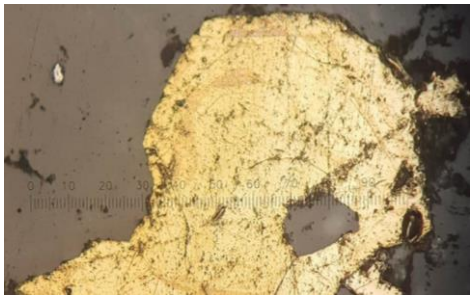 Figure (d): An example of ICP zoning from sample AU57414 after bleach etching.
Intra, Dirty, Planar (IDP)	This group is similar in appearance to the ICP grains. The edges of each colour zone are not clear or easy to define. Within each zone there may also be some large pitted textures. The darker coloured zones are commonly dirtier than the lighter zones. Figure (e) shows how the 'dirty' texture occur, and how the zoning is not following the grain geometry.	 Figure (e): An example of IDP zoning from sample AU58148 after bleach etching.
Intra, Dirty, Planar, Bordered (IDPB)	These grains have a similar appearance to the ICRB grains. However, they are not as obvious under reflected light, as the colour change can be very slight. Also, the dirty, pitted textures of the grain can obscure the recognition of the zonations. Within each zone there may also be some dissolution and the grain surface can look pitted. The darker coloured zones are commonly dirtier than the lighter zones. Figure (f) shows the indistinct nature of the zoning, and the single colour, including the textures in the inner part of the grain and their 'dirty' appearance.	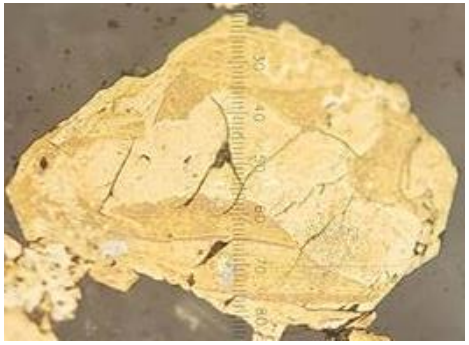 Figure (f): An example of IDPB zoning from sample AU58144 after bleach etching.

Intra grain - Radial

Intra grain, clean, radial (ICR)

Grains in this group display concentric or radial zoning similar to tree ring growth formations. The rings reflect the crystallographic growth surfaces of the grains, seen in figure 5.2.1.2. Each colour change is sharply defined, and straight (no jagged or wavy edges). Grains of this group are generally the larger grains in the sample, and can be seen from 50x magnification using a reflected light microscope.

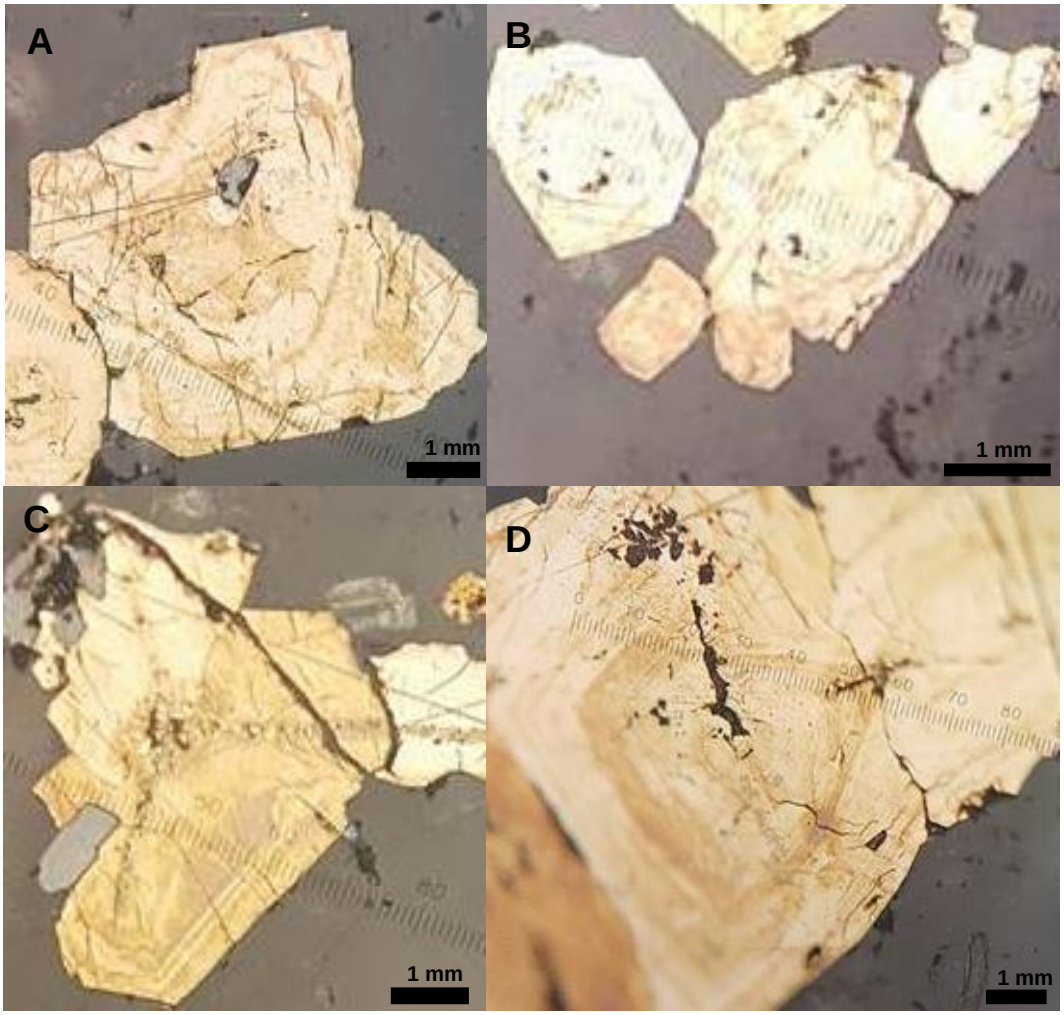

Figure 5.2.1.2: examples of ICR zoning from A: AU56192_Z2, B: AU56192_Z1, C: AU56192_Z3b and D: AU58148_Z2.

Intra grain, inclusion rich (dirty), radial (IDR)

These grains are similar to ICR grains as their zones also reflect the crystal faces. However, in IDR grains there are typically less visible growth bands. The edges of each colour zone are not as clear or easy to define as in the ICR grains, however there are some well-formed crystal faces, as seen in B in figure 5.2.1.3 below. Within each band there may also be some pitted textures and the grain surface can have multiple colours, including green, blue and purple.

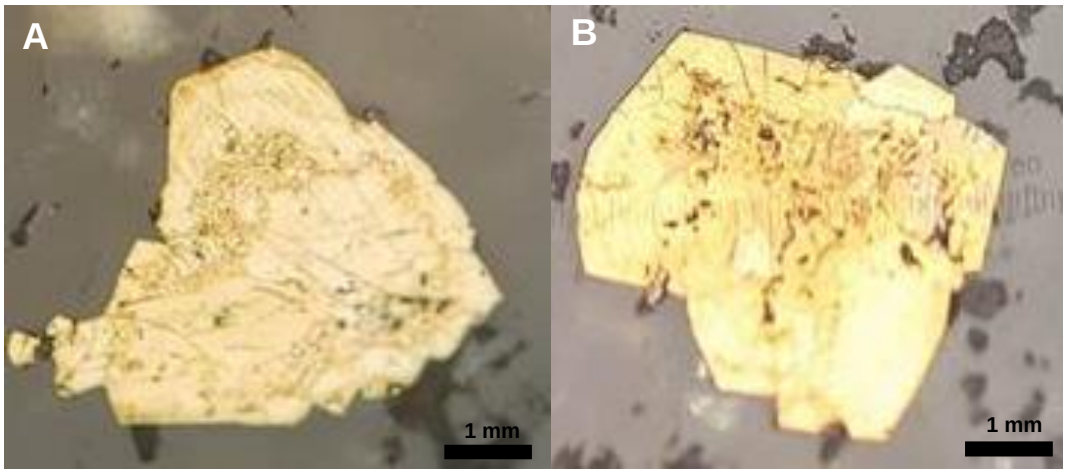

Figure 5.2.1.3: examples of IDR zoning in A: AU56192_Z3a and B: AU60281_Z1.

Intra grain, clean, radial, bordered (ICRB)

The zoning in this type of pyrite grain is limited to two distinct zones, creating the appearance of a border or rim. The border follows the inner shape of the grain, with the outer grain edge sometimes parallel, but often not.

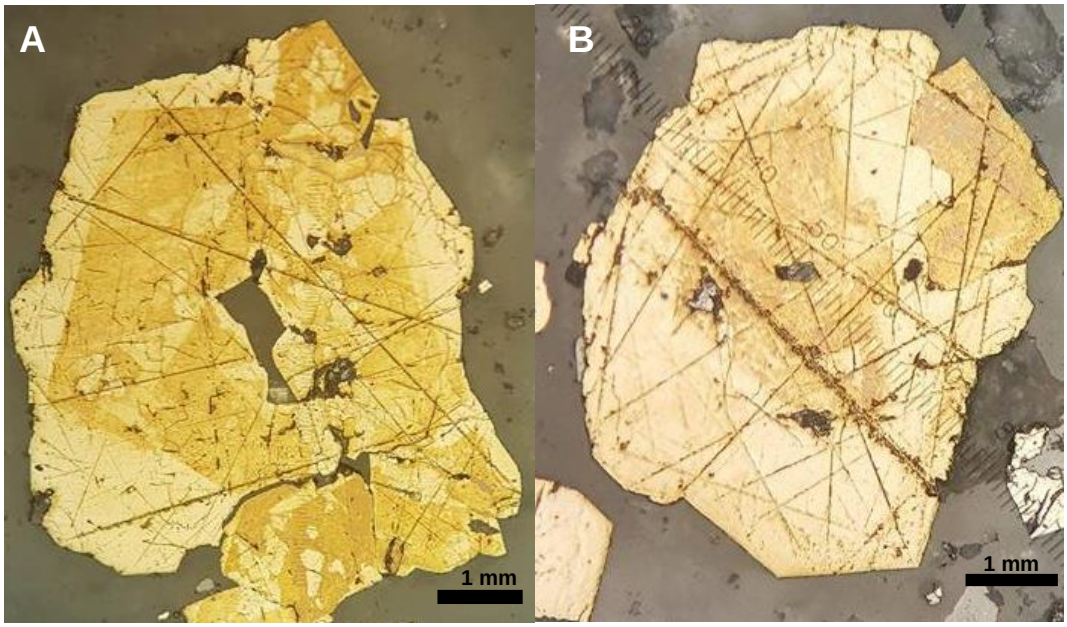

Figure 5.2.1.4: examples of ICRB zoning in A: AU57390B_Z1 and B: AU57390B_Z2a.

Intra grain - Planar

Intra grain, clean, planar (ICP)

The grains in this group have clearly defined zones of differing colour that do not define well-formed crystal faces. Often these zone textures apply to one side of a grain or have an apparently random occurrence. These grains are similar in size to the IDR and ICR, being larger again (300 µm) than the inter grain group (<30 µm).

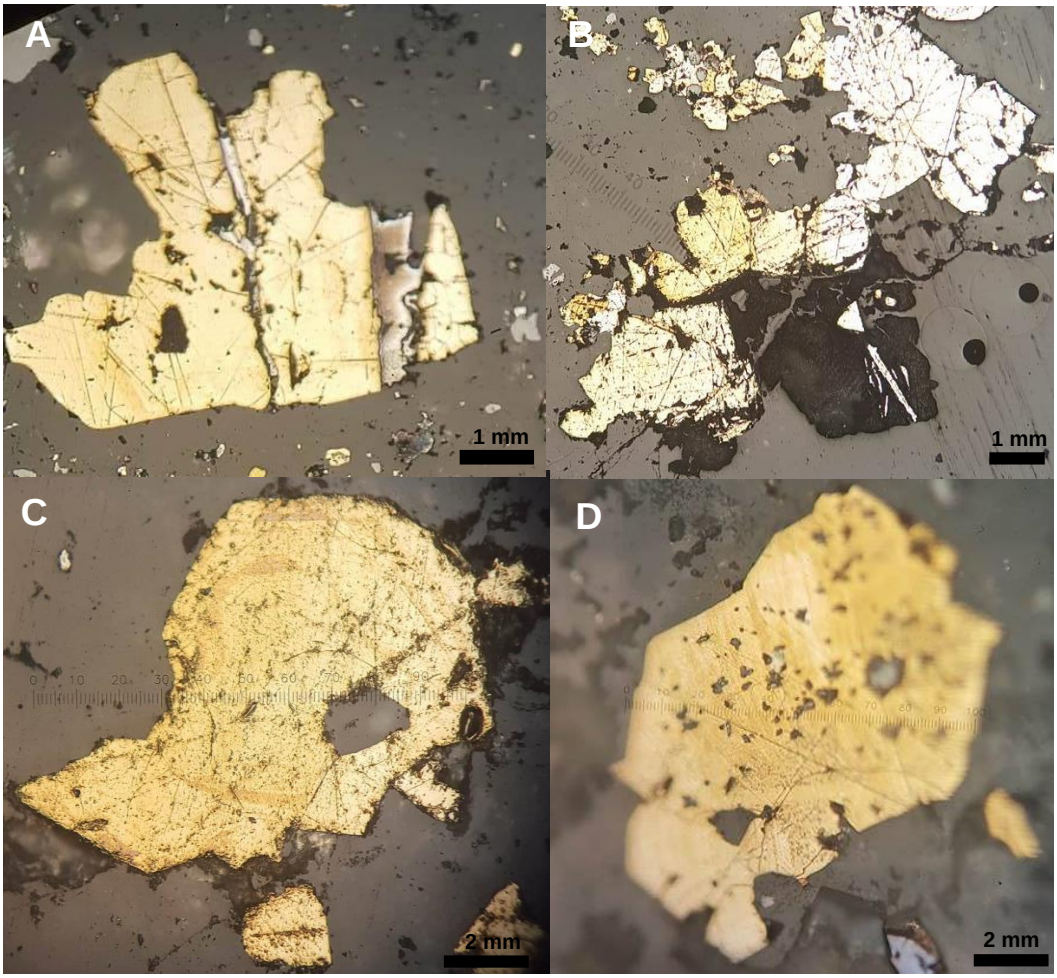

Figure 5.2.1.5: examples of ICP zoning from A: AU56202_Z4, B: AU56211, C: AU57414 and D: AU57417_Z1.

Intra grain, inclusion rich (dirty), planar (IDP)

This group is similar in appearance to the ICP grains. The edges of each colour zone are not clear or easy to define. Within each zone there may also be some pitted textures, giving the grain a dirty appearance, and the grain surface can include other colours such as green, blue and purple. The darker coloured zones are commonly dirtier than the lighter zones. There are at least two zones within individual grains in samples of this type.

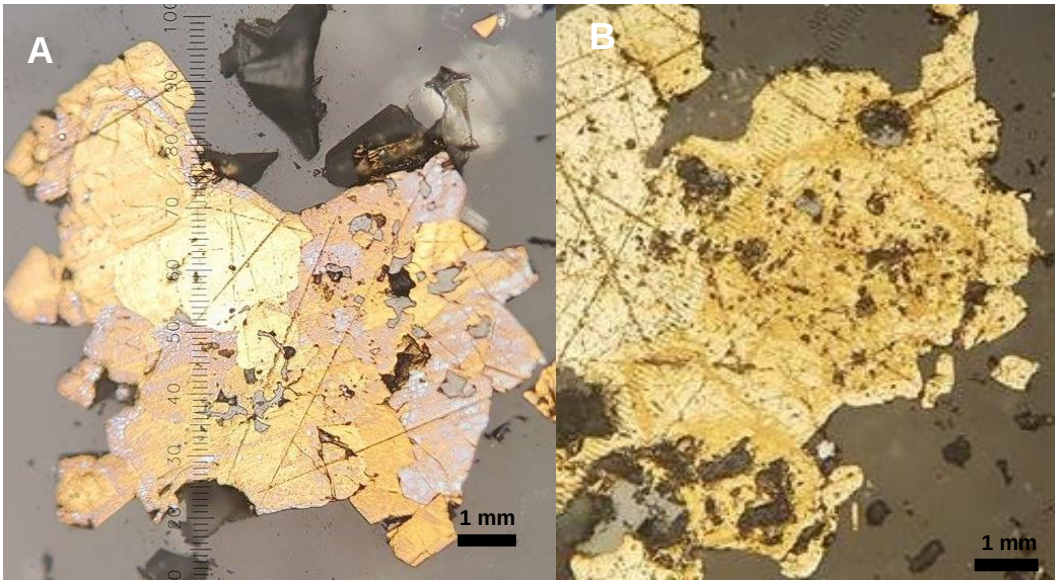

Figure 5.2.1.6: examples of IDP zoning in A: AU60281_Z3 and B: AU58148_Z1.

Intra grain, dirty, planar, bordered (IDPB)

These grains have a similar appearance to the IDP grains. However, they only have two zones, and the colour change can be very slight, or the dirty texture of the grain can obscure the defined zone change. Within each zone there may also be some dissolution and the grain surface can look pitted and include greens, blues and purples. The darker coloured zones are commonly dirtier than the lighter zones.

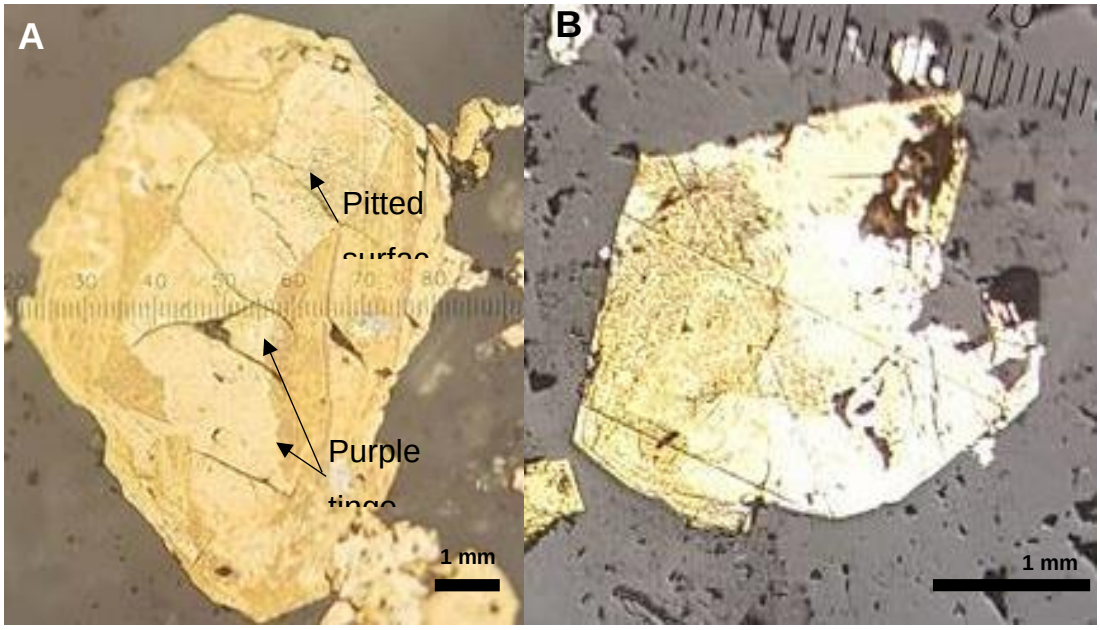

Figure 5.2.1.7: examples of IDPB zoning in A: AU58144_Z1 and B: AU56196_Z2.

5.3 Discussion

The pyrite from the Martha deposit within the Waihi epithermal system displays a wide range of textures. The samples showed both inter grain and intra grain type zoning. All samples observed showed inter grain type zoning, with not all displaying intra grain zoning. The pyrite grains in sample AU56192 exhibited both ICR zoning and IDR zoning. The pyrite grains in sample AU58148 had both ICR and IDP type zoning. The pyrite in sample AU60281 was shown to have inclusion rich zoning types with grains in both IDR and IDP zoning groups, making it similar in appearance to the Martha samples. Sample AU57390B displayed only ICRB type zoning. The single zoned grain from AU56202 was in the ICP category, along with the sole grains from samples AU56211, AU57417 and AU57414. The only zoned grain in sample AU56196 displayed IDPB zoning.

5.3.1 Sulfidation and Crystal Growth

Crystal growth begins with nucleation (Murowchick & Barnes, 1987). The conditions for growth depend on the thermodynamics, and mass transfer within the system (Rosenberger, 2012). Ideal conditions are trace element-rich fluid, with optimum temperature, pH and saturation (Wu et al., 2004). Transport of S, Fe availability and trace elements to encourage crystal growth depends on phase equilibrium (Rosenberger, 2012). In the case of pyrite, there is H_2S present dissolved in water, forming a saturated solution (HS^-). There is also Fe present in the wall rock, releasing Fe^{2+} ions. The reaction of the HS^- with the Fe^{2+} forms FeS_2, or, pyrite (Wu et al., 2004). The majority of H_2S present is still in gaseous form as the solubility of H_2S in water is 0.01 mol/L (Wu et al., 2004). These conditions; the presence of FeS and $H_2S_{(g)}$, drives the pyrite forming reaction which is outlined in the equation below, and is known as the mechanism of sulfidation (Rickard & Luther, 1997, Wu et al., 2004).

$$H_2S + FeS = FeS_2 + H_2$$

Pyrite crystallises in many different crystal forms. Pyrite growth depends on the presence of the required elements; Fe and S (Rickard & Luther, 1996). Pyrite forms via sulfidation, described in the equation above (Cline, 2001).

5.3.2 Zoning and Crystal Growth

Intra, Clean, Radial

The clean texture of the grains with ICR zoning suggests that growth of these grains was uninterrupted. The radial appearance of the zones indicates that growth was a consistent, continued process (Rickard & Luther, 1996). Each zone can be attributed to when the fluid chemistry changed throughout grain growth, rather than the rate of grain growth, as it is not always possible to tell how fast each grain grew (Chouinard et al., 2005). None of the grains with ICR zoning have straight clean edges on all sides. This suggests their growth was limited by available space, rather than chemical conditions conducive to pyrite growth, or, sulfidation (Rickard & Luther, 1996). The samples that exhibited ICR zoning were replacement pyrite in the wall rock. This supports the statement that their growth was limited, as pyrite formation as replacement pyrite in the wall rock is more restricted, in terms of space, than vein pyrite formation. This is because the wall rock is pre-existing at the time of pyrite formation, compared to the vein, which was still infilling at the time of pyrite formation.

Intra, Dirty, Radial

IDR zoning suggests a more complex growth than the ICR zoning. The dirty texture can be suggestive for a higher concentration of trace elements or inclusions (Huston et al., 1995). Grains with IDR zoning indicate initial growth conditions with high trace element concentration and condition conducive to trace element incorporation within pyrite. The subtle nature of the boundary between the dirty and clean zones suggests the whole grain grew without periods of dissolution (Chouinard et al., 2005). The trace element chemistry of the grains is discussed in further detail in the following chapter, sections 6.3, 6.4 and 6.5.

Intra, Clean, Radial, Bordered

The grains that exhibit ICRB zoning suggest a more complex growth history. Both the grains central darker zones are heterogeneous in texture. This suggests that these grains experienced a period of initial growth followed by a period of dissolution, where part of the grain was dissolved or possibly cracked under pressure or movement (Thomas et al., 2011). When growth began again the outer border of the grain was formed with the inner gaps possibly infilled during the later growth stage, as explained in figure 5.3.2.1. The sharp edges of the boundaries within the ICRB zoned grains indicates the conditions for growth, dissolution and regrowth occurred with periods where the pyrite became under-saturated in trace elements. These conditions were possibly the result of a decrease in pH of the fluid, as this is seen in multiple grains and pyrite growth is hindered in strongly acidic conditions (Wu et al., 2004).

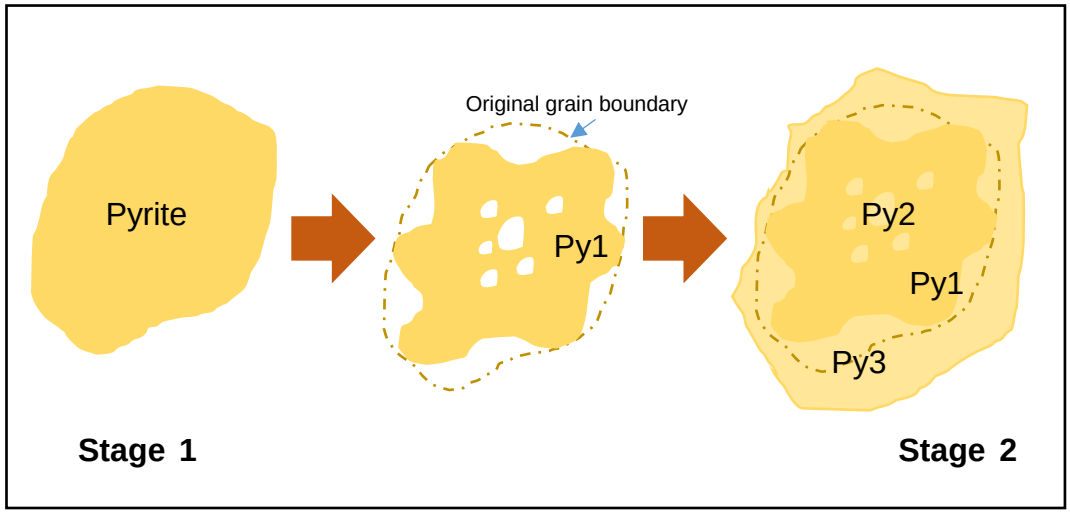

Figure 5.3.2.1: the three stages of growth that could produce a grain with ICRB zoning, based on observations of grain AU57390B_Z1.

Intra, Clean, Planar

There are two theories that could explain the presence of ICP zoning. One is that two grains grow independently of each other and then, fuse together as they continue to grow (Figure 5.3.2.2). Another theory is that a single grain began growth, growth was stopped after a certain point (when the zones change from dark to light) and when growth was re-initiated in the

same grain, the fluid chemistry was different and the physical controls, such as space, on the grain's growth limited it to grow on only one crystal face of the initial grain.

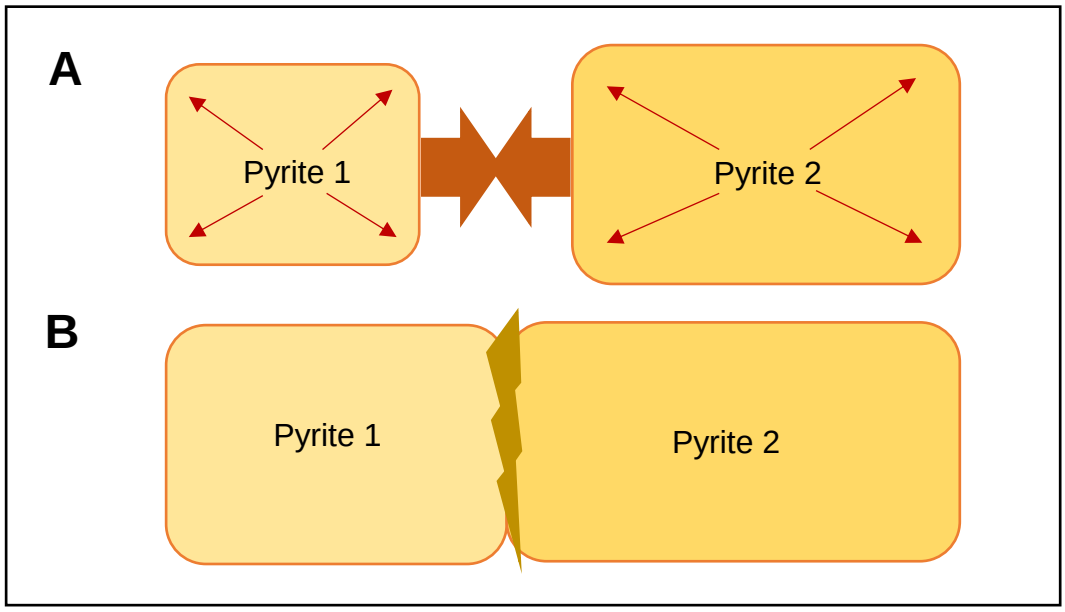

Figure 5.3.2.2: suggested growth history of an ICP grain, where the beginning has two grains, that fuse to one.

Intra, Dirty, Planar

The theories for growth resulting in ICP zoning can also be attributed to the IDP zoning. The difference being that the first of the two zones has a higher level of inclusions or trace elements (Huston et al., 1995, Chouniard et al., 2005).

Intra, Dirty, Planar, Bordered

IDPB zoning is suggestive of an early growth stage that was suddenly stopped. After this initial fluid when little to no trace elements were incorporated, there was a period of new growth from a trace element rich fluid. There do not appear to have been any periods of dissolution during the initial pyrite growth or the secondary dirty grain growth.

5.3.3 Fluid Changes

Inter grain

Inter grain zoning suggests that grains within a single sample grew at different times, with a fluid chemistry change between grain growth rather than during. If the grains formed at the same time, with variable chemistry of the fluid, internal zoning would be observed. This results in the variable colours of grains after bleach etching, and is seen in all samples that also show zoning within individual grains. This is much more common than intra grain type zoning.

Intra, Clean, Radial

ICR zoning exhibits signs of uninterrupted growth, from fluids with variable chemistry. In the case of figure 5.2.2D, there are multiple concentric zoning, most very narrow resulting in the grain resembling an internal tree ring-like structure. These thin zones suggest that while the grain grew there were periods of frequent fluid chemistry change. Each change was only long enough for the growth of a narrow band of pyrite to be added to the growing grain. ICR grains with wider bands have less zones overall, suggesting that there were less fluid chemistry variations during the period of the grain's growth, as seen in figure 5.2.2a. The ICR grains with wider zones are the same size as those with thinner zones, suggesting that zoning thickness and the number of zones in ICR grains is not controlled by grain size.

Intra, Dirty, Radial

IDR zoning shows less zones than ICR. In the case of figure 5.2.3 the grain only has two zones. The dirty texture is found in the centre of the grain, with the cleaner zone surrounding it. IDR grains appear to have had a period of initial growth, with inclusions likely causing the dirty texture. The presence of the clean outer zone suggests the fluid chemistry during that part of the grain's growth was lower in inclusions and resulted in the growth of a cleaner pyrite. The zone boundaries in IDR grains are gradational. This suggests that there was a single fluid whose composition changed progressively, as opposed to two distinct fluid compositions being responsible for pyrite growth, as in the case of ICR grains. IDR grains appear to oxidise much

faster under NaOCl than ICR grains. Inclusions in pyrite can alter polishing quality of the surface of the grain, grains with inclusions appear rougher, providing a larger surface area for oxidation (Thomas et al., 2011). The array of peacock colours associated with over-bleaching was observed in IDR grains in the same sample where ICR grains were found. The ICR grains in the observed sample were subjected to the same degree of bleach etching, yet did not appear to over-oxidise, as can be seen in figure 5.2.3 above.

Intra, Clean, Planar

ICP zoning has both clearly defined boundaries and gradual boundaries. Grains that exhibit ICP zoning are not the regular angular shape of pyrite that is expected. Grains such as in figure 5.2.5 have a side of the grain that is dark and the other side is light. This suggests the fluid chemistry has changed during the grain's growth, but unlike the ICR and IDR grains it hasn't resulted in the standard radial changes. As in the ICR grains, both dark and light zones are clean, with no obvious inclusions.

Intra, Dirty, Planar

IDP zoning is similar to ICP zoning with the exception of the presence of the dirty texture which, like IDR zoning, occurs in one of the two zones, the other being clean and appearing to be the outer, second zone to grow. IDP zoning also results in only two zones (like IDR), but unlike the IDR zoning there are clear defined boundaries between zones. This suggests that the growth of an IDP zoned grain began with a trace element rich fluid, before an instant change to a fluid chemistry of comparatively depleted inclusions.

Intra, Clean, Radial, Bordered

ICRB zoning is visually distinctive. These grains have only two zones, which suggest two stages of growth. The border is the lighter zone in all cases of ICRB zoning found. Boundaries between zones are distinct, which is consistent with the idea of two distinct fluid chemistries. The inner darker zones have a less homogeneous texture than the outer clean zones and this is seen in figure 5.2.1.4.

Intra, Dirty, Planar, Bordered

IDPB zoning is very similar to ICRB zoning. The one difference is the appearance of the dirty texture, which can be seen in figure 5.2.1.7 above. In all IDPB zoning found the dirty zone is the outer zone and the inner zone is the clean one. This is unlike any of the other dirty zoning types. IDPB zoning suggests the fluid chemistry was initially lower in trace elements, with the second stage of grain growth occurring in a fluid with higher trace element concentrations (Large et al., 2009, Chouinard et al., 2005). In the IDPB zoning found, there appeared to be a high rate of oxidation, with the peacock colours visible, as in the IDR zoning (Thomas et al., 2011).

5.3.4 Relationships

Wall Rock vs. Vein Samples

The wall rock samples analysed exhibit ICR, ICP and IDP type zoning. There does not appear to be any relationship between the type of zoning and the location, depth or type (wall or vein) of the sample. Wall rock samples do not stand out based on texture. They have both clean and dirty textures suggesting the wall rock samples experienced the same fluid changes as the vein hosted samples. There were vein samples present with every type of zoning texture, indicating the pyrite growth conditions were the same for the wall rock and the vein.

Alteration

There does not appear to be any relationship between the degree of alteration observed in the sample and the subsequent zoning. The highly altered samples are not confined to one particular type of zoning, nor are they absent from any particular type of zoning. This suggests that the controls on the zoning in the pyrite are not directly related to interactions between hydrothermal fluid and wall rock (Reich et al., 2014). The ICR zoned grains are from intensely altered wall rock samples. However, other grains from within the same sample exhibit other types of zoning. For

example, sample AU56192 has three grains with ICR zoning and one grain with IDR zoning.

Vein Textures

There is no apparent relationship between boiling conditions and pyrite zoning. The samples with colloform and crustiform textures do not have a specific zoning type. However, the IDR zoning occurs only in samples from within crustiform sulfide bands. All the ICP zoned samples are situated in a vein/wall rock sample, with crustiform/colloform textures common in most, along with high grade mineralisation. The samples that exhibited ICP zoning did not exhibit any other type of zoning, suggesting that the boiling conditions resulted in a different growth evolution for the pyrite compared to other zoning types (Vidal et al., 2016). There is only one sample that shows ICRB zoning, and it is a vein sample that consists of colloform banded green clay-sulfides, cross cut by fine colloform banded quartz veins. It is the only sample with the presence of banded green clay-sulfides and is the sample that is to the South of the main cluster of samples.

Mineralisation

The two samples in which visible gold was observed display ICP and IDPB zoning. Most of the samples are clustered close around N643100 E395500, which is within the Martha deposit, with samples further away displaying a variety of zoning types also found in the central group of samples. All samples were referred to in the Fyfe (2014) thesis as high grade samples, and were collected based on their electrum concentration and previous assays. The presence of amethyst quartz could possibly influence the zoning type, with samples containing amethyst quartz displaying only dirty textures. This suggests that amethyst quartz occurs when fluid is inclusion rich, so where amethyst quartz is present, the pyrite will be inclusion rich.

Inclusion-rich vs. Inclusion-poor Pyrite

It appears that the inclusion rich pyrite typically occurs during the initial growth of a grain. With the exception of the IDPB zoned grains, the IDR and IDP grains suggest that the grains began growth in trace element rich

conditions, with the later growth conditions being much lower in trace elements. This indicates that there was a mixing of deep chloride rich fluids with steam heated ground water, producing the high concentration in trace elements in the earlier fluids (Brathwaite & Faure, 2002, Simmons et al., 2005). The shape of the grain does not appear to reflect the inclusion rich/poor state, with both the IDR grains showing regular straight edges, similar to the ICRB grains. Similarly, the ICR grains have a variety of regular straight edges and irregular jagged edges. The inclusion-rich pyrite oxidised at a faster rate than the inclusion-poor pyrite. The different rates of oxidation were expected, and hence the use of the bleach etching method (Craig & Vokes, 1993). The result of varying rates of oxidation and subsequent variable internal textures in the pyrite grains supports the theory that the internal chemistry of the pyrite grains is not homogenous (Large et al., 2009, Chouinard et al., 2005).

5.4 Limitations

The bleach etching methods for showing textural zoning in exposed grains is effective, provided the surfaces of the grains are not already oxidised (Craig & Vokes, 1993). To ensure accurate before and after observations, the samples were re-polished, removing the old, oxidised surface and exposing a fresh new surface. This newly polished surface was observed under reflected light microscopy, the texture of the grains noted and photographed, then the bleach etching was carried out. After the bleach etching, the same observations were made under reflected light microscopy, and the changes to grains was noted and photographed. Before and after observations were made at the same locations on the grains, allowing for direct comparison.

The bleach etching method cannot account for the orientation of grains. The particular orientation of each grain within the sample depends on the direction in which the original core sample was cut at, during the process of making the 1 inch epoxy mounts. Effectively, the grain is being analysed in two dimensions, and may display very different textural characteristics had it been sliced at a different angle. This is a complex problem to solve, as the same individual grain within a sample cannot be cut at multiple angles, due to their microscopic size (30-300 μm) and the logistics of cutting and re-mounting an existing 1 inch epoxy mount. Here, electron backscatter diffraction (EBSD) observations would be helpful, as they give a more detailed image of the crystal structure, potentially indicating a grain's three-dimensional appearance (Baker et al., 2006).

It should also be noted that individual grains of interest are not guaranteed to be representative of every pyrite grain in the Waihi epithermal system. The quartz lodes within the Martha open pit extend for over 1.5 km in a NE-SW direction (Brathwaite et al., 2005). Each pyrite grain is only 30-300 μm in diameter. This means that while several different textures were observed, there may be many more textural varieties that exist that were not observed, due to the scale difference between sample size and the extent of the Waihi epithermal system as a whole.

5.5 Comparisons

Large et al. (2009) and Chouinard et al. (2005) both found zoning in pyrite grains. Chouinard et al. (2005) analysed grains from the high sulfidation, epithermal Au-Ag-Cu Pascua deposit, located in the El Indio belt in north-central Chile. The aim of the study was to identify the presence of trace elements, including invisible gold, in solid solution within the pyrite grains.

They expected, that the trace elements would be distributed concentrically, and that trace element occurrence was a function of the crystallographic nature and growth of the pyrite grains. This could be seen at a textural level under SEM. Figure 5.5.1 below shows X-ray, or, electromagnetic pulse (EMP) maps, with the textural characteristics of the grain displayed. The centre of the grain has a dirty texture, while the outer grain is cleaner. The EMP maps suggest that the trace element distribution is what was expected; focused in the centre of the grain, with the outer part of the grain relatively low in trace elements.

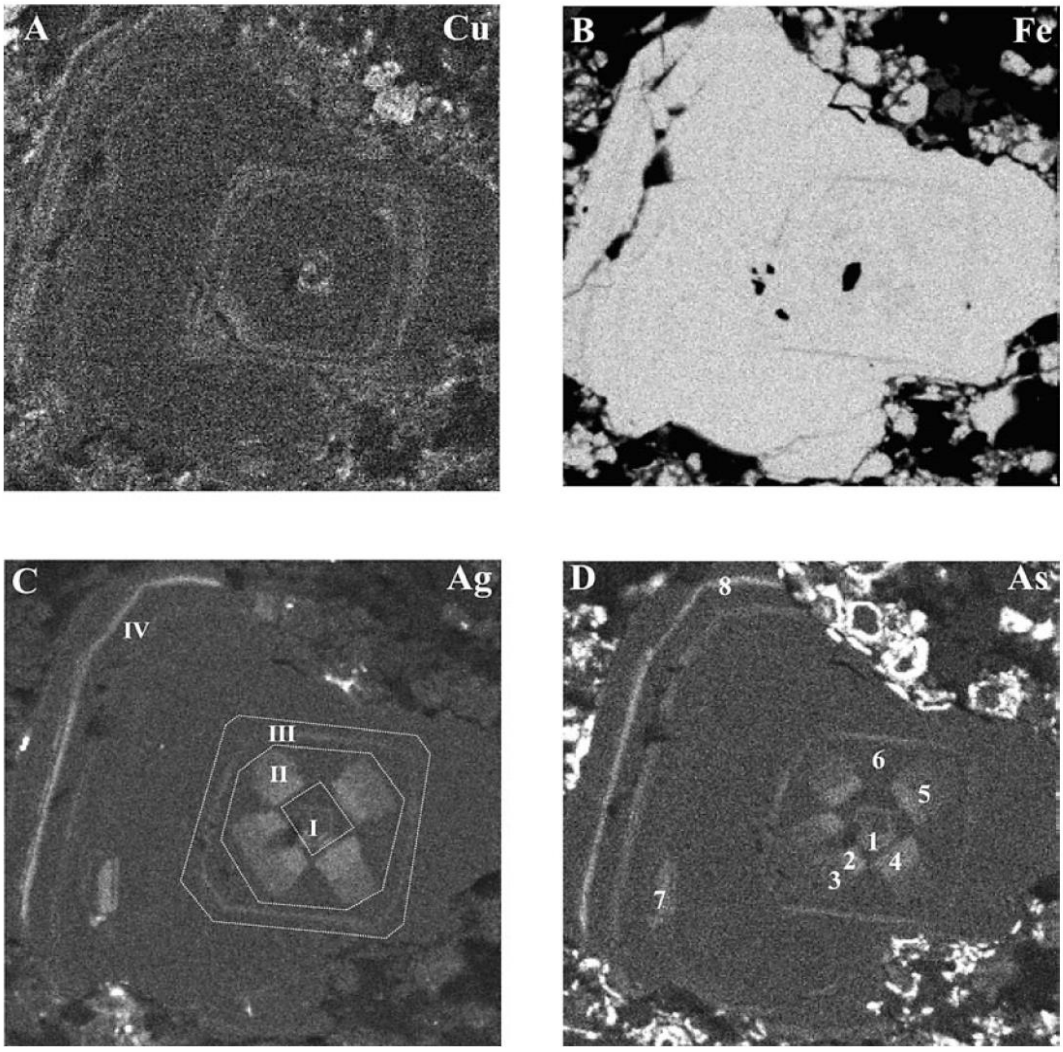

Figure 5.5.1: EMP maps of A- Cu, B- Fe, C- Ag, D- As from pyrite in the Pascua epithermal system. The numbers in C show the various growth zones. The numbers in D indicate EMP spot analyses. The bright spots in A and D are soluble sulfates. The bright spots in C are late iodargyrite and chlorargyrite (Chouinard et al., 2005).

Large et al. (2009) found that pyrite grains from four Carlin-style and orogenic sediment-hosted deposits also held varying textures. The aim of their study was to trace Au and other trace elements through the history of the system, based on the incorporation of Au and trace elements in the pyrite. The pyrite in these settings is a combination of early diagenetic pyrite and a later hydrothermal pyrite that formed growth zones around the earlier, existing pyrite. In all four systems the pyrite texture was dirty in the centre, and surrounded by a cleaner outer zone, as shown in figure 5.5.2. All four grains from all four systems display a dirty, central early diagenetic pyrite

surrounded by the cleaner hydrothermal pyrite. This is the same texture observed by Chouinard et al. (2005).

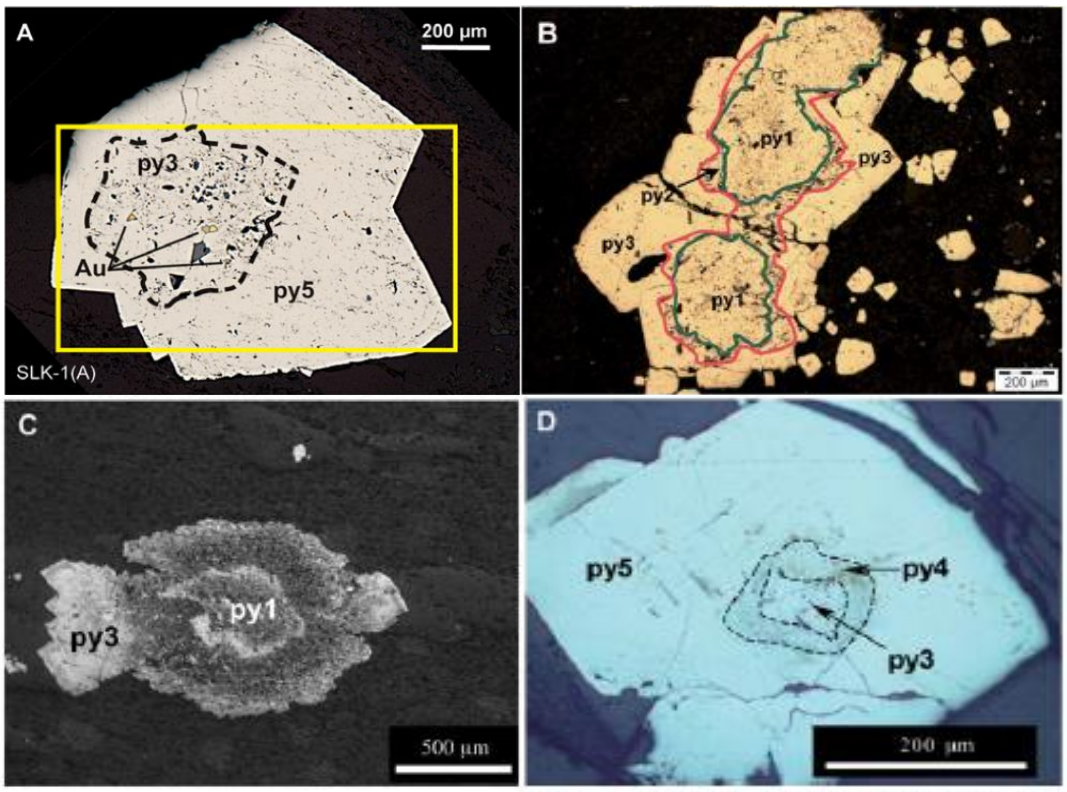

Figure 5.5.2: examples of the zoning found in the various deposits studied by Large et al. (2009). A; the Sukhoi Log deposit with Au inclusions. B; Spanish Mountain. C; Bendigo gold deposit. D; Sukhoi Log gold deposit.

Considering the aforementioned findings, the following question can be posed; Can we see any similarities between the zoning in any of Large et al (2009) and the Chouinard et al. (2005) pyrite, and the pyrite observed at Waihi? If so, can we identify the influences on the formation of zoned pyrite?

There are some textures found in the Waihi pyrite that do resemble textures found by Chouinard et al. (2005) and Large et al. (2009). ICRB zoning describes the textures seen in Spanish Mountain and Sukhoi Log pyrite, as well as the pyrite from the Pascua deposit. This is shown well in figures 5.5.3 and 5.5.4 below.

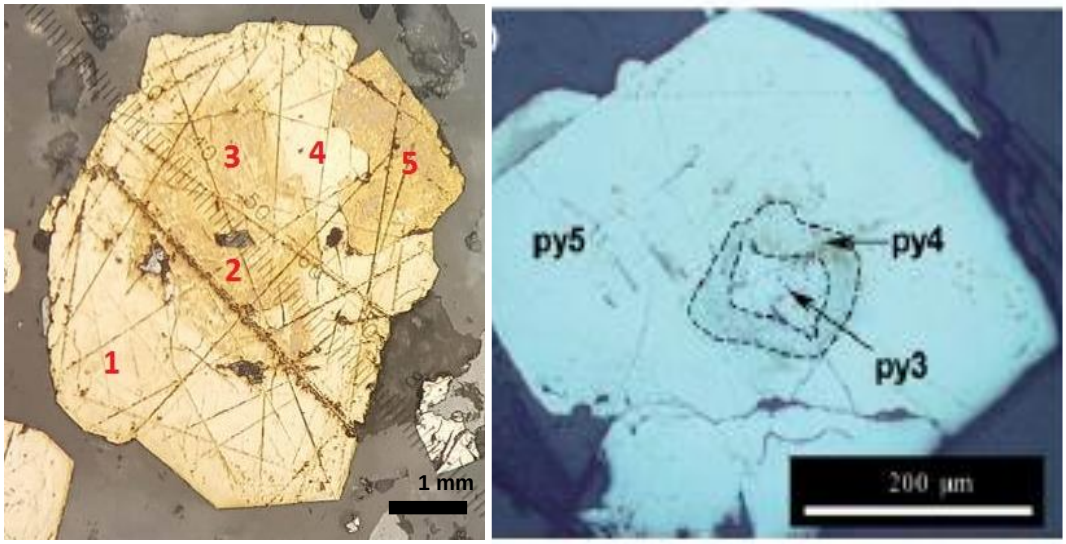

Figure 5.5.3: sample AU57390B_Z2a from Waihi (left) next to pyrite from Sukhoi Log (right) (Large et al., 2009). There are similarities between the grain's central texture and outer cleaner zone.

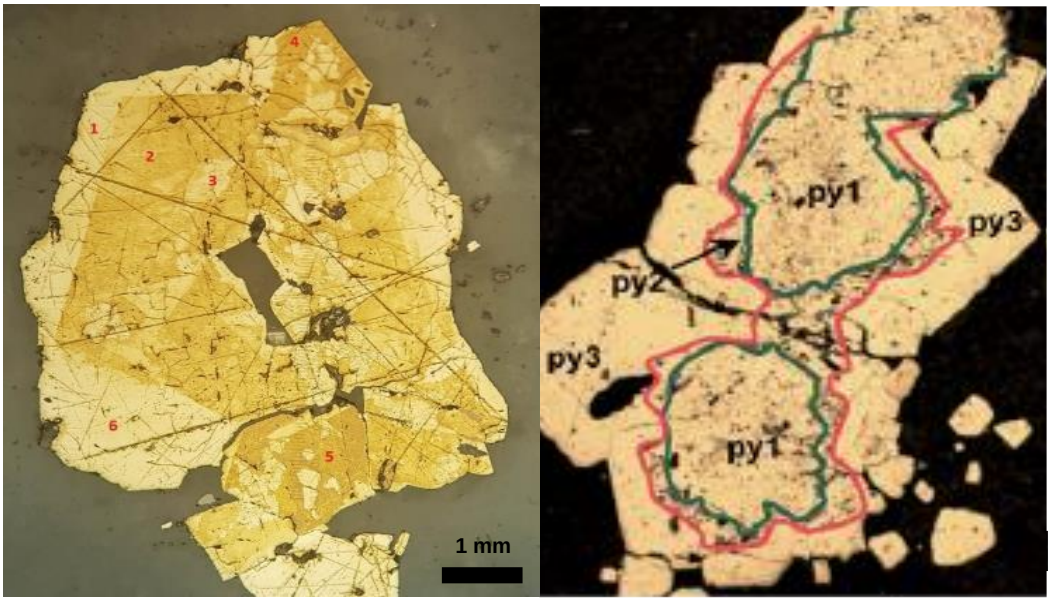

Figure 5.5.4: sample AU57390B_Z1 from Waihi (left), next to pyrite from Spanish Mountain (right) (Large et al., 2009). Similarities between the pyrites can be seen, with the dirty central zoning and clean outer zone.

6. Trace Element Composition of Pyrite

6.1 Trace Element Composition of Pyrite in the Martha Deposit

Trace element analysis of pyrite grains can provide insight into changing hydrothermal system conditions during the grain's growth (Baker, et al., 2006, Large et al., 2009, Barker et al., 2009, Reich et al., 2013, Vidal et al., 2016). This chapter describes the trace element analysis of the samples described in the previous chapter carried out by the microanalytical techniques described in the methods chapter: XFM, EPMA and LA-ICPMS. Firstly, the results of the trace element distribution in the XFM samples is examined, followed by the concentration of trace elements in different zones within pyrite, using EPMA. Finally, the relative concentration of trace elements within individual grains is discussed. At the end of the chapter there is a discussion on the behaviour of trace elements, relationships, and what the trace element analysis suggests regarding the system's history. Results are then compared with other studies of a similar nature.

6.2 XFM analysis – Element Associations

Three hand samples were mapped at the XFM beamline at the Australian Synchrotron. Two were sulfide bands on the edge of quartz veins and the third was a massive sulfide on the edge of a quartz vein. Red, Green, Blue (RGB) images were generated from concentrations calculated from the XFM data across the samples to give an idea of element association. These images show three selected elements, which are assigned a colour (red, green or blue). The intensity of the colour represents the concentration of the specific element.

The red blebs in the image indicate Au is present outside of the pyrite grains, most likely as electrum, which is typical for mineralization at Waihi (Brathwaite & Faure, 2002). The pyrite grains (blue) have varying concentrations of As, as they have green in bands within the grains. The green bands of high As show interesting patterns within grains including multiple bands of varying widths and bands that follow a pattern different to the outermost crystal faces of the grain. As is the only element to appear

distributed in this way. With the relative Fe concentration decreasing where As increases. Selected elements were focussed on for element associations, with the created images illustrating the element distributions in the given sample area. Fe is often included to show the location of the pyrite, as well as highlight internal zoning textures. As, Cu, Zn, Ag and Au results are described below. All images from the XFM can be found in Appendix III, Analysis Images, XFM RGB Maps.

Figure 6.2.1 shows the location of the analysis points on sample AU56187. Images are of quartz slides used at the XFM.

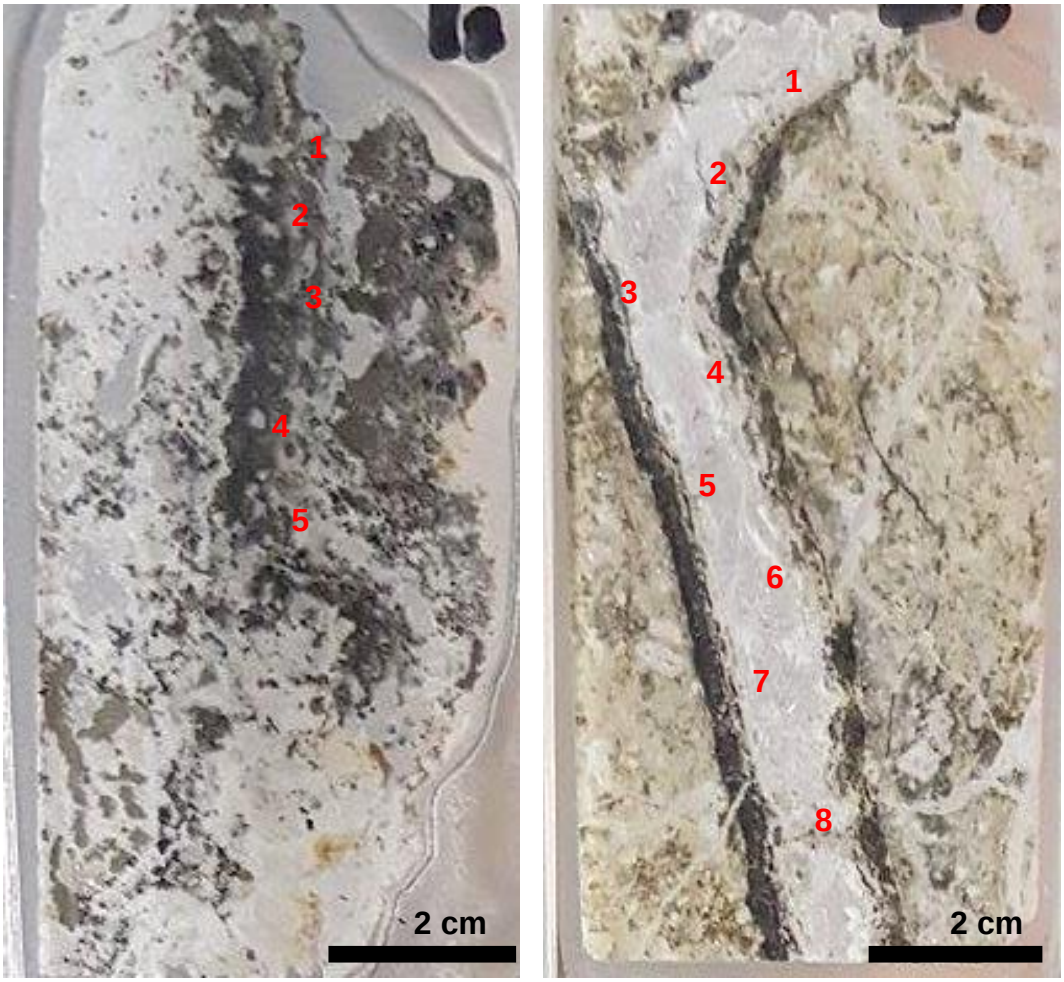

Figure 6.2.1: images of sample AU56187. The hand sample was cut into two thin sections. Left is AU56187A, right is AU56187B. The red numbers show the different XFM analysis points.

Figure 6.2.2 below gives an example of the type of image created when Au, As and Fe were selected to create an RGB map. The intensity of the colour indicates the concentration of the selected element.

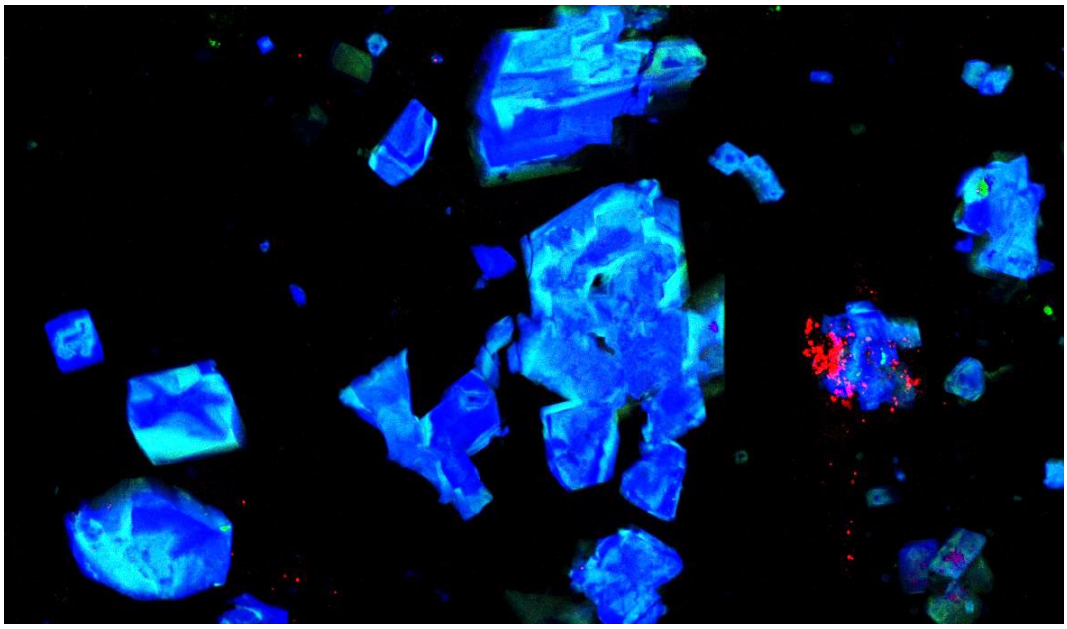

Figure 6.2.2: example of a RGB image of element distribution modelled from the XFM data. Image from sample AU56187A_2. Red: Au, Green: As, Blue: Fe. Field of view (FOV) is 200 x 100 µm.

Arsenic in Pyrite

The textures observed in the previous chapter by use of the bleach etching method which showed radial or concentric zones (seen in the previous chapter) have also been found by use of the XFM images. Figures 6.2.3, 6.2.4, 6.2.5 and 6.2.6 show how there is As banding within pyrite grains similar to what is seen in the previous chapter.

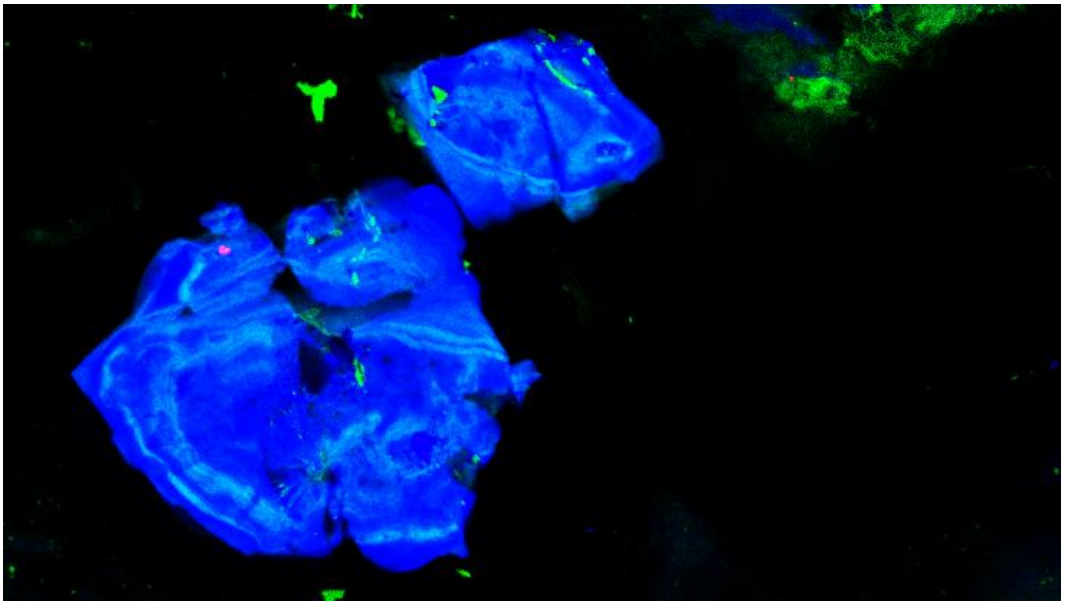

Figure 6.2.3: RGB image AU56187B_5 from the XFM data showing the As bands within pyrite. Red: Au, Green: As, Blue: Fe. FOV 200 x 100 µm.

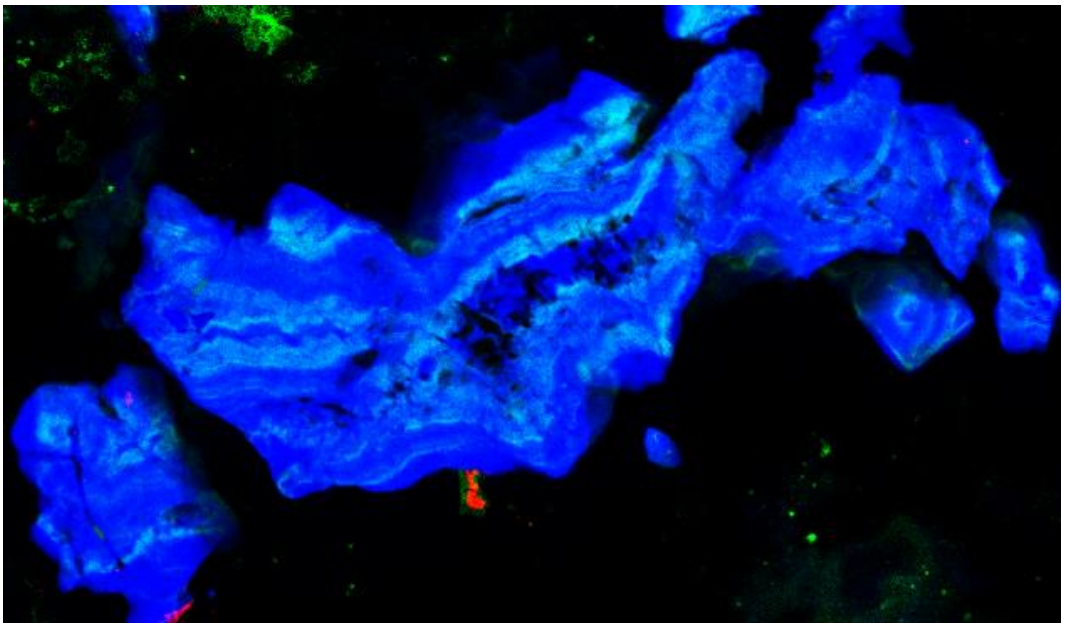

Figure 6.2.4: RGB image from sample AU56187B_4. XFM data showing the As bands within pyrite. Red: Au, Green: As, Blue: Fe. FOV 200 x 100 µm.

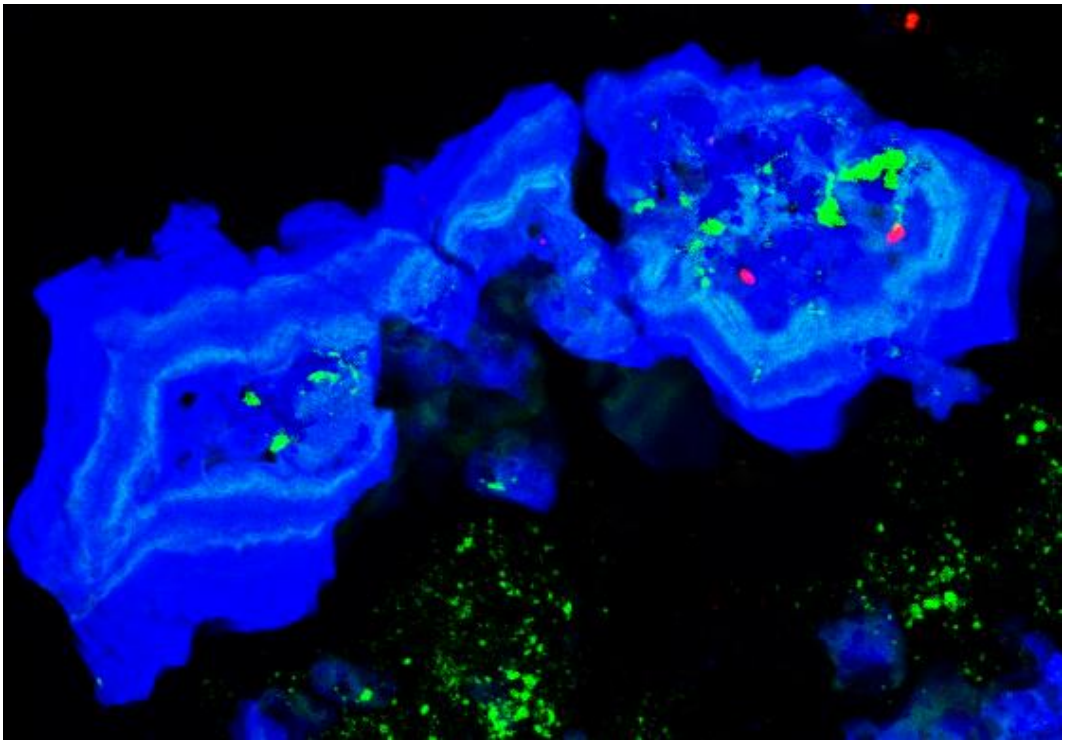

Figure 6.2.5: RGB image from sample AU56187A_3. XFM data showing the As bands within pyrite. Red: Au, Green: As, Blue: Fe. FOV 200 x 150 µm.

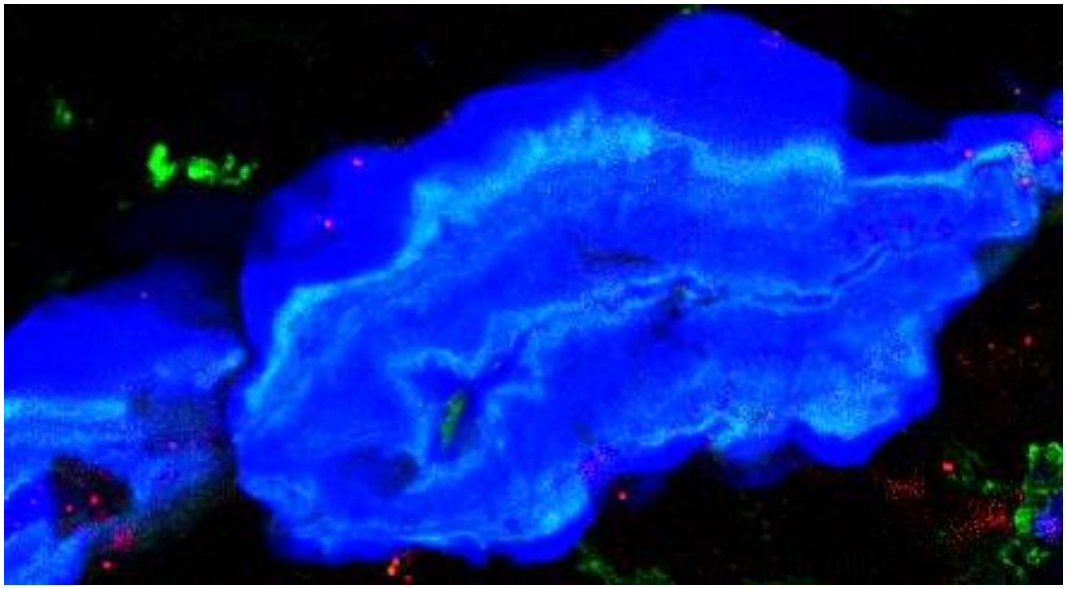

Figure 6.2.6: RGB image from sample AU56187B_7. XFM data showing the As bands (paler blue) within pyrite. Red: Au, Green: As, Blue: Fe. FOV 200 x 100 µm.

In all the above figures, there are multiple As rich bands within pyrite grains. There appears to be no presence of Au within the grain detectable using the XFM techique. Lack of Au detection could be influenced by the XFM resolution. Where the detection limit was not low enough to detect all the Au in the sample. The low Au concentration could also be the As peaks strongly overlapping the Au due to the similar energy of As and Au. This means that high enough concentrations of As can result in the software mis-attributing Au for As, producing a falsely high As peak, and a low, or absent, Au peak, or showing high Au concentration where none is present. Most of the Au is known to be present in the Waihi ore in the form of electrum (Simmons et al., 2005), and the XFM analyses for Au and Au containing electrum. While there is some Au expected in the pyrite, a majority of the Au is expected to be found in electrum, mostly in the quartz vein (Brathwaite & Faure, 2002). The limitations associated with low Au concentrations are discussed in further detail in the following discussion section.

Copper in Pyrite

Figure 6.2.7 below shows how the As-rich grain is bordered with a clear blue edge of Cu. The grain appears to contain flecks of Au, however these are probably mis-attributed As, as the brightness of the green in the RGB image indicates this is a high-As pyrite grain. The Cu border is unusual, and not observed in other areas of the sample.

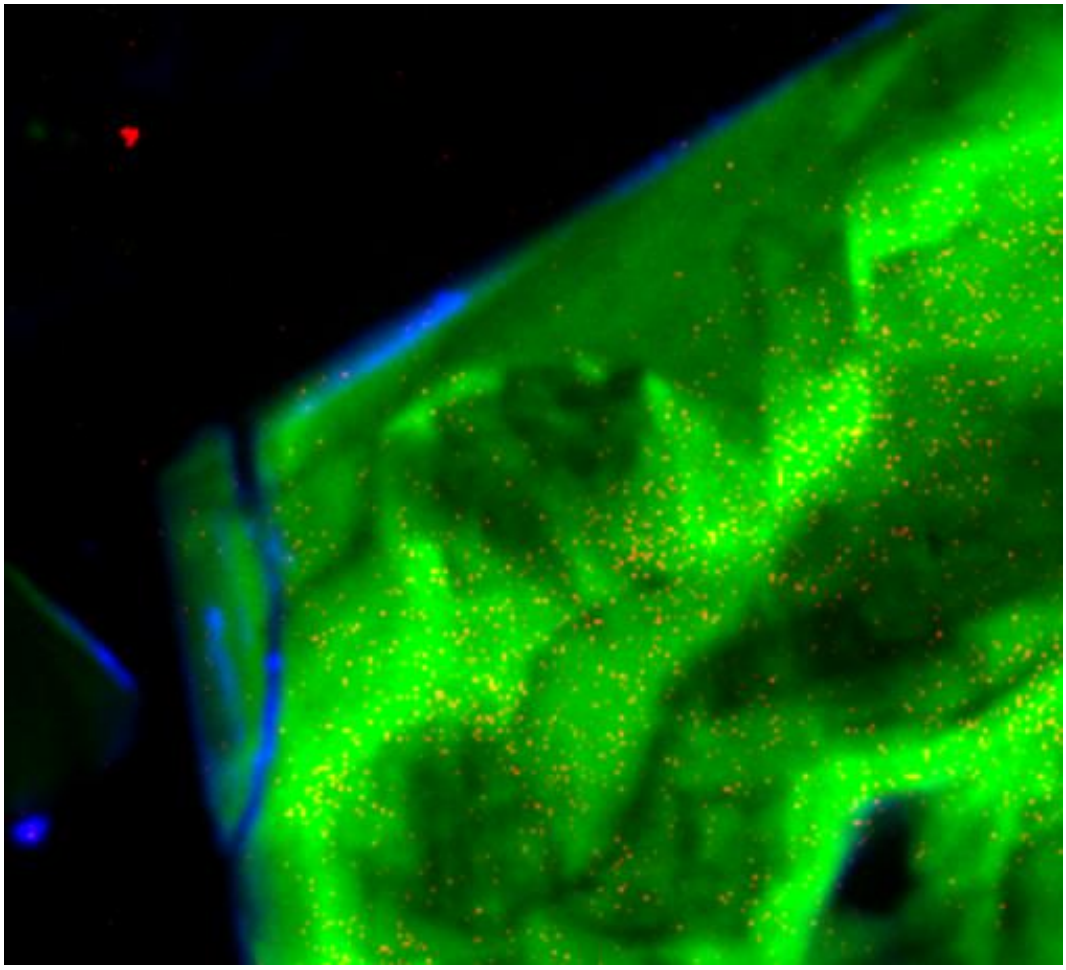

Figure 6.2.7: RGB image from sample AU56187A_5 showing an arsenic-rich pyrite grain with gold inclusions. The blue edge of the grain is Cu-rich. Red: Au, Green: As, Blue: Cu. FOV 200 x 200 µm.

Gold and Silver in Pyrite

Gold occurs in the quartz veins in the all the samples, as well as within the pyrite grains. Figures 6.2.8, 6.2.9, 6.2.10 and 6.2.11 below show how the Au is situated in the quartz, outside of the pyrite grains. The Au and Ag in these images includes electrum, which is also assumed present in these samples (Brathwaite & Faure, 2002). The electrum appears to be presented as mostly Ag with lower concentrations of Ag. There is some Ag present without Au, and this is assumed to be acanthite. Figure 6.2.11 is an example of the Au and Ag occurring outside the grains, and is the best display of possible electrum in the quartz vein.

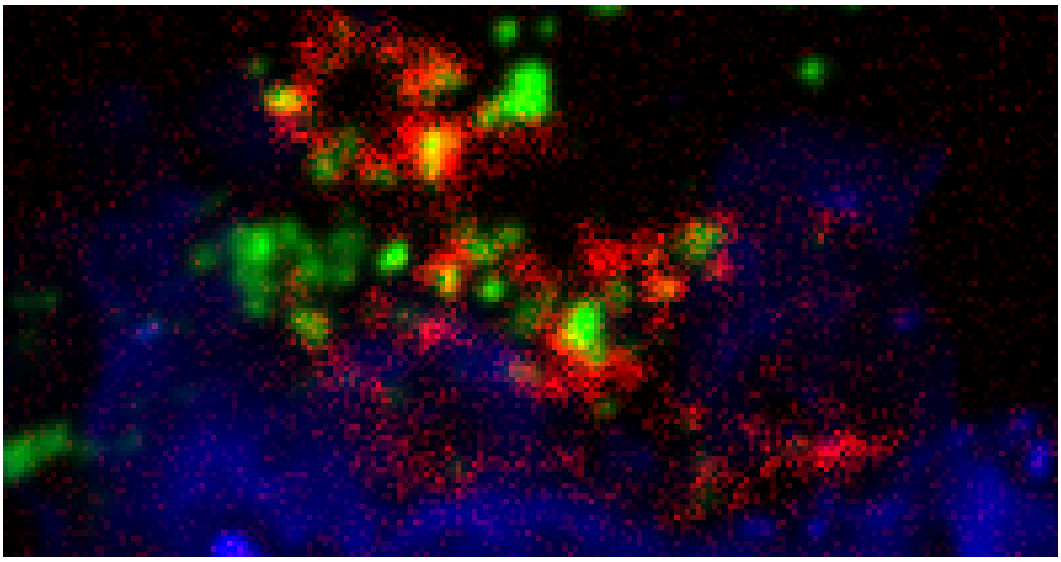

Figure 6.2.8: RGB image from sample AU56187A_5 showing the occurrence of Au (green) and Ag (red) outside of the As-rich pyrite grain (blue). Red: Ag, Green: Au, Blue: As. FOV 200 x 100 µm.

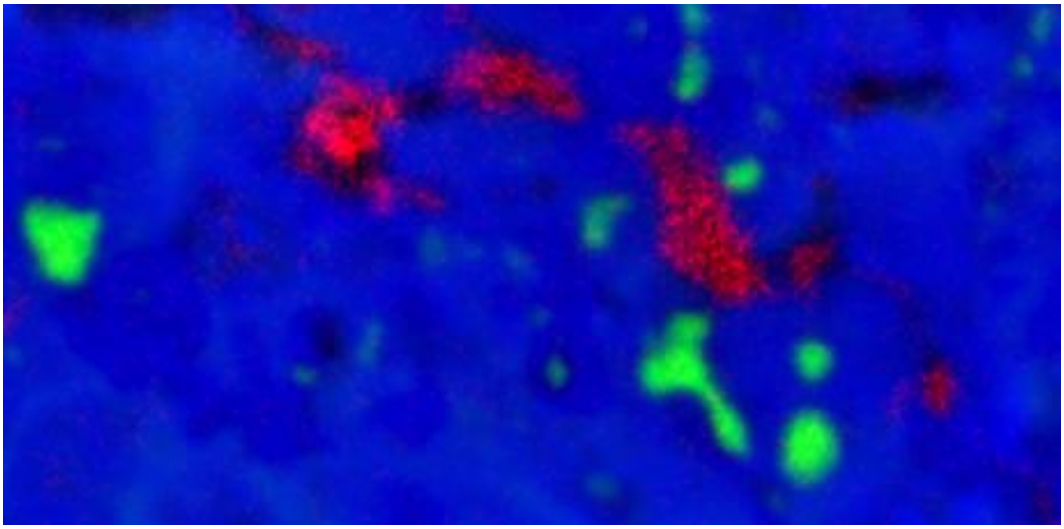

Figure 6.2.9: RGB image from sample AU56187A_4 showing the occurrence of Ag (red) outside of the pyrite grain. Red: Ag, Green: As, Blue: Fe. FOV 200 x 100 µm.

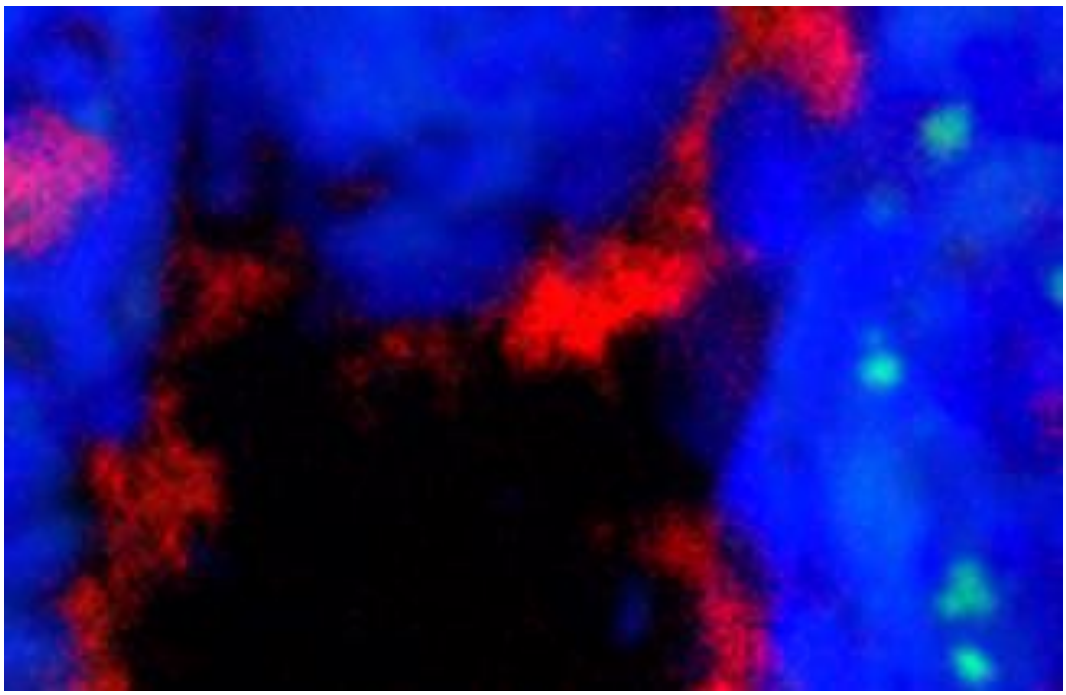

Figure 6.2.10: RGB image from sample AU56187A_4 showing the occurrence of Ag (red) outside of the pyrite grain. Red: Ag, Green: As, Blue: Fe. FOV 200 x 100 µm.

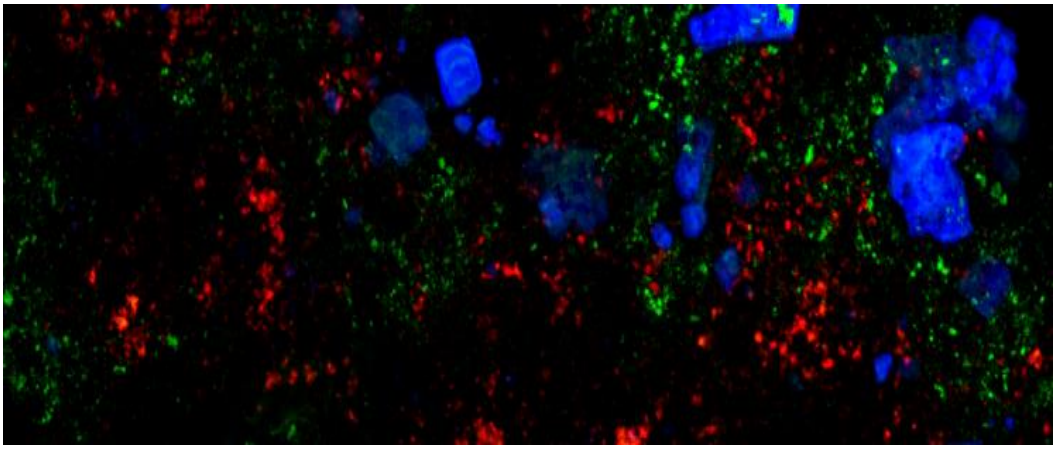

Figure 6.2.11: RGB image from sample AU56187A_4 showing the occurrence of Au (red) outside of the pyrite grain. Red: Au, Green: As, Blue: Fe. As is present in this sample in the matrix, coating the quartz grains, as well as present in the pyrite grains. FOV 300 x 100 µm.

Interesting Textures

A bubble shaped texture was observed in sample AU56187B in the quartz vein. The bubble wall appears to be mostly Mn and Fe, with a fleck of gold in the rim, as seen in figure 6.2.12 below. There are bands visible within the bubble wall that are low in Mn and Fe. It is not clear what this texture indicates.

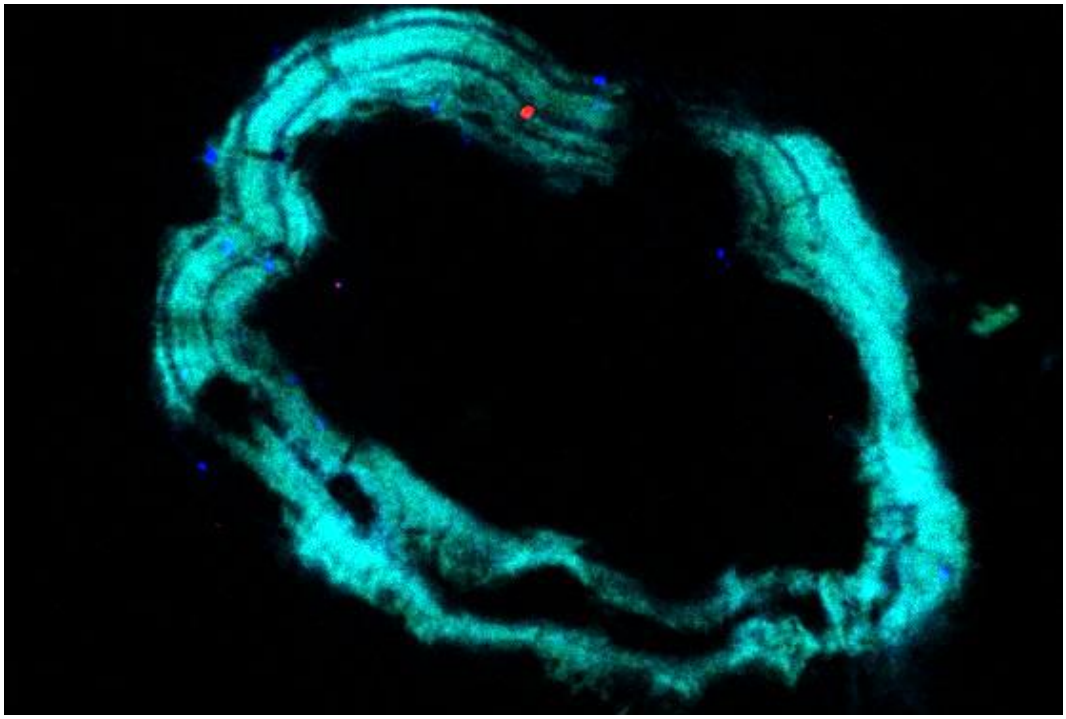

Figure 6.2.12: RGB image from sample AU56187B_6 showing the appearance of a bubble with a Mn and Fe-rich wall, containing a fleck of gold. Red: Au, Green: Mn, Blue: Fe. FOV 200 x 150 µm.

6.3 EPMA

The different zones observed under reflected light, described in the previous chapter, were analysed using point analysis to measure the concentration of a suite of major, minor and trace elements at a given point. In this case, each zone was analysed from individual grains to identify the chemical variation between visible zones. Table 6.3.1 below shows the median of concentrations from samples. Table 6.3.2 shows the maximum values, and table 6.3.3 shows the minimum values from the EPMA analysis. Detection limits are based on count rates and are estimated at around 50 ppm (0.005 mass%) for trace elements.

There is a distinct variation in As concentration in all of the grains, as demonstrated in the figures 6.2.3, 6.2.4, 6.2.5 and 6.2.6 from the XFM section above. Au levels are generally high in one or two zones and absent in the rest of the zones within the grain. Ag levels are low, with no association between Au and Ag concentration. Figure 6.3.2 below shows the variable concentration of As between zones in a grain from sample AU57390B. There appears to be an increase in As in the darker zones. Figure 6.3.7 shows how trace element concentration changes with depth. All images from the EPMA analysis can be found in Appendix III, Analysis Images, EPMA Backscatter.

Table 6.3.1: Element concentration medians in mass% from EPMA analysis.

Sample	Au	As	Te	Ag	Zn	Cu	Pb	Fe	Si	Co	Se	Sn	V	S
AU57417	0.01	0.21	BDL	BDL	BDL	BDL	BDL	49.31	0.07	0.09	BDL	BDL	BDL	49.28
AU58203	0.01	0.30	BDL	BDL	0.02	0.01	0.07	49.31	0.02	0.08	BDL	BDL	BDL	46.95
AU60281	0.01	0.16	BDL	BDL	0.04	BDL	BDL	38.78	0.13	0.08	BDL	BDL	BDL	41.10
AU56192	0.01	1.00	BDL	BDL	BDL	0.01	BDL	49.77	0.03	0.10	BDL	BDL	0.01	42.26
AU56202	0.02	0.12	BDL	0.02	0.01	0.02	BDL	52.19	0.06	0.09	BDL	BDL	BDL	47.51
AU58148	0.01	0.49	BDL	BDL	BDL	BDL	0.07	52.73	0.02	0.09	BDL	BDL	BDL	47.67
AU57390B	0.01	0.72	BDL	BDL	0.01	0.02	BDL	46.42	0.02	0.08	BDL	BDL	BDL	44.65
AU56196	0.01	0.52	BDL	BDL	BDL	0.01	0.03	51.29	0.02	0.07	BDL	BDL	BDL	43.02
AU58144	0.01	0.55	BDL	BDL	BDL	0.02	BDL	49.59	0.02	0.08	BDL	BDL	BDL	44.26

Table 6.3.2: Element concentration maximums in mass% from EPMA analysis.

Sample	Au	As	Te	Ag	Zn	Cu	Pb	Fe	Si	Co	Se	Sn	V	S
AU57417	0.02	0.58	BDL	0.01	0.04	0.01	0.09	49.50	0.15	0.09	0.05	0.01	0.02	50.51
AU58203	0.03	2.39	BDL	0.02	0.26	0.44	0.42	49.74	0.18	0.10	0.03	0.03	0.02	50.98
AU60281	0.10	1.07	0.01	0.07	1.81	4.55	1.81	48.78	11.71	1.02	1.57	6.26	0.11	44.52
AU56192	0.03	2.23	0.01	0.03	0.04	0.03	0.10	51.12	0.27	0.12	BDL	0.02	0.02	45.88
AU56202	0.03	0.31	BDL	0.09	0.02	0.03	BDL	52.39	0.08	0.12	0.11	BDL	BDL	47.73
AU58148	0.02	1.62	BDL	0.01	0.02	0.02	0.21	53.05	0.03	0.10	0.02	0.01	0.02	48.56
AU57390B	0.04	1.88	BDL	0.01	0.07	0.12	0.20	52.94	0.13	0.11	BDL	0.01	0.02	47.50
AU56196	0.02	1.48	BDL	0.02	0.38	0.02	0.26	52.74	0.13	0.09	BDL	0.01	0.01	45.07
AU58144	0.02	1.37	0.01	0.01	0.02	0.04	BDL	53.14	0.05	0.09	BDL	BDL	0.01	45.50

Table 6.3.3: Element concentration minimums in mass% from EPMA analysis.

Sample	Au	As	Te	Ag	Zn	Cu	Pb	Fe	Si	Co	Se	Sn	V	S
AU57417	BDL	BDL	BDL	BDL	BDL	BDL	BDL	48.73	0.01	0.07	BDL	BDL	BDL	48.07
AU58203	BDL	BDL	BDL	BDL	BDL	BDL	BDL	48.14	BDL	0.06	BDL	BDL	BDL	45.62
AU60281	BDL	BDL	BDL	BDL	BDL	BDL	BDL	0.32	0.02	BDL	BDL	BDL	BDL	0.28
AU56192	BDL	0.32	BDL	BDL	BDL	BDL	BDL	48.22	0.01	0.07	BDL	BDL	BDL	40.84
AU56202	0.01	BDL	BDL	BDL	BDL	BDL	BDL	52.03	0.03	0.08	BDL	BDL	BDL	46.30
AU58148	BDL	BDL	BDL	BDL	BDL	BDL	BDL	50.02	BDL	0.06	BDL	BDL	BDL	45.91
AU57390B	BDL	BDL	BDL	BDL	BDL	BDL	BDL	BDL	0.01	0.06	BDL	BDL	BDL	39.01
AU56196	BDL	0.11	BDL	BDL	BDL	BDL	BDL	BDL	0.01	0.07	BDL	BDL	BDL	39.19
AU58144	0.01	BDL	BDL	BDL	BDL	BDL	BDL	BDL	0.01	0.05	BDL	BDL	BDL	38.89

Figure 6.3.1: image of grain from sample AU57390B_Z1. The red numbers indicate the location of point analysis. The maximum, average and minimum As values are annotated on the corresponding zones in blue.

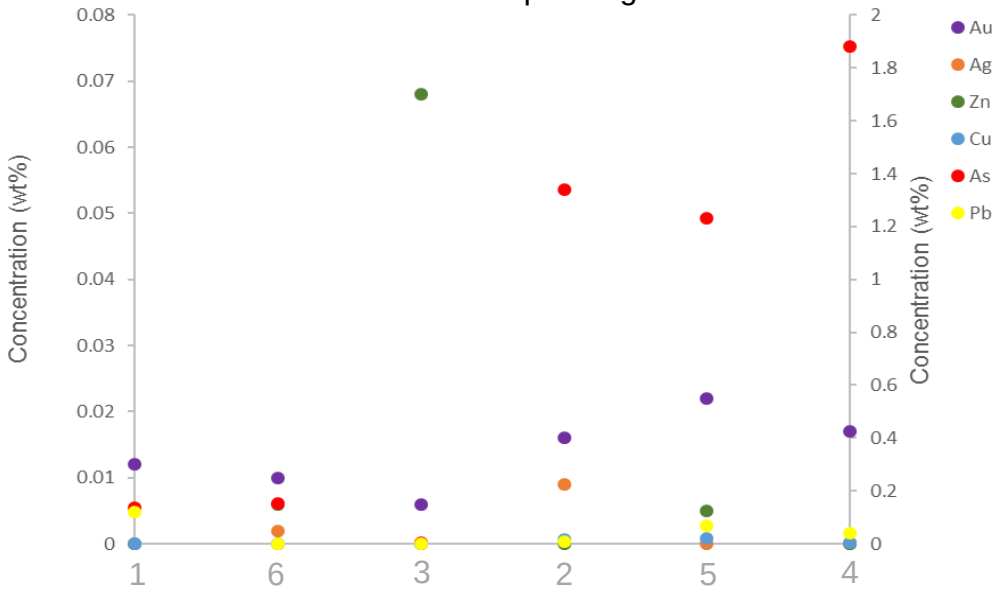

Figure 6.3.2: graph of As, Au, Ag, Zn and Cu concentration across zones 1-6 on sample AU57390B_Z1. The numbers correspond to numbered points on figure 6.3.1 above and are ordered on the X axis from lightest coloured to darkest coloured zones. Au, Ag, Zn, Cu, Pb on Y axis. As on Z axis.

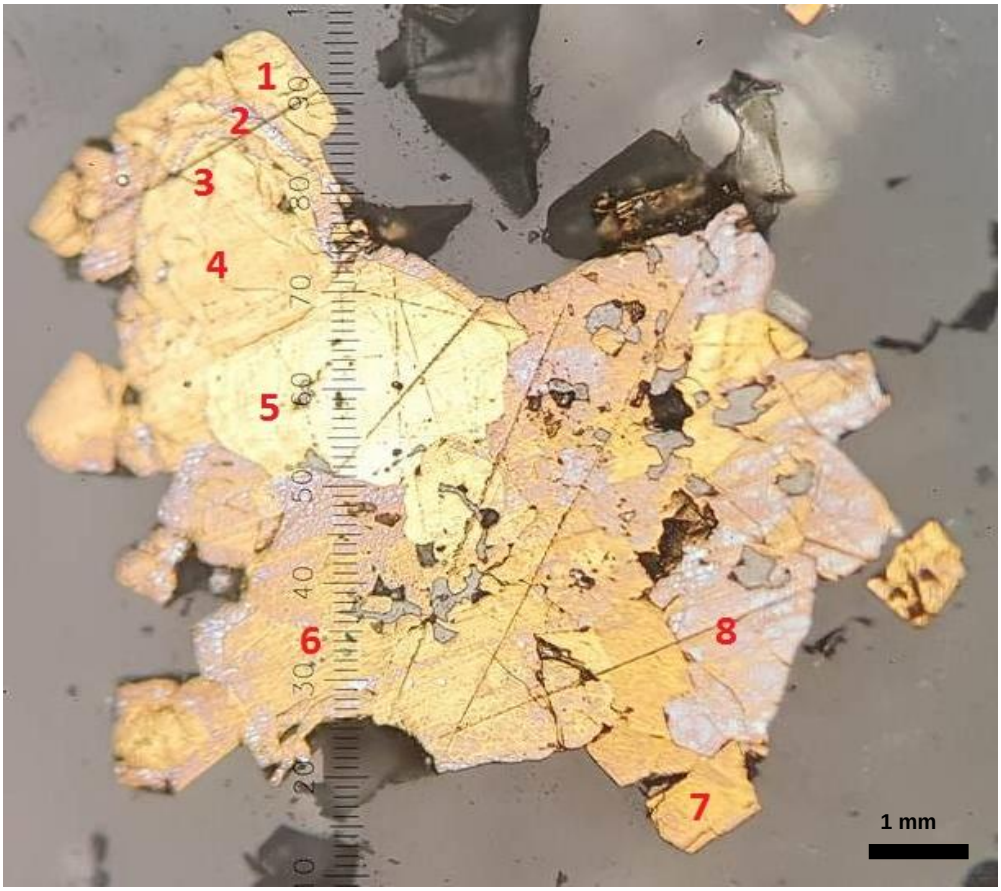

Figure 6.3.3: image of grain from sample AU60281_Z3. The red numbers indicate the location of point analysis.

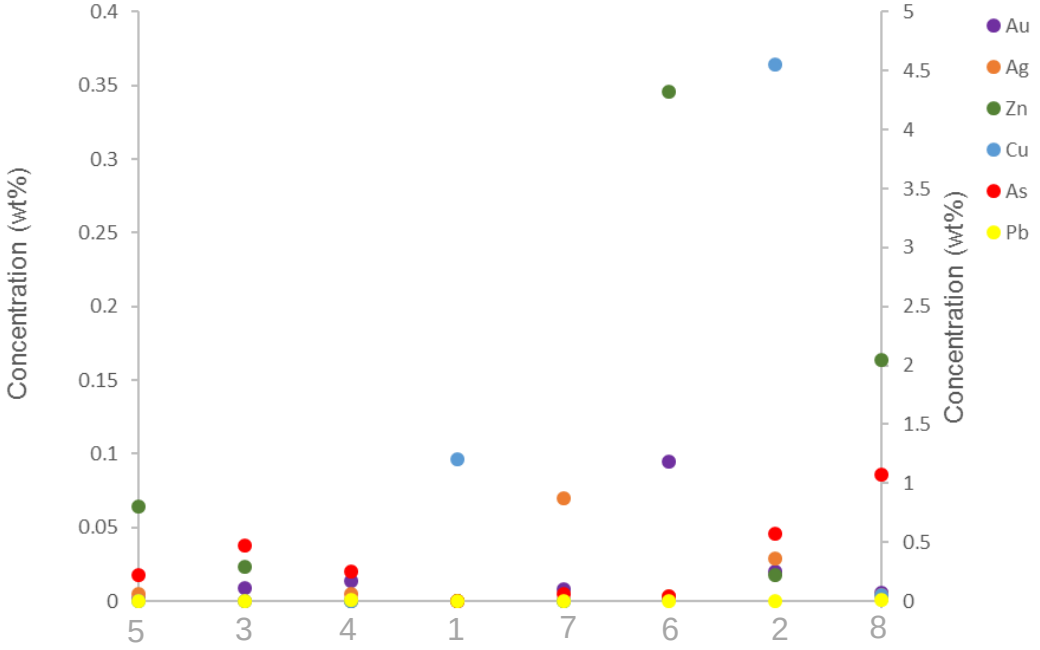

Figure 6.3.4: graph of element concentration across zones 1-8 on sample AU60281_Z3. The numbers correspond to numbered points on figure 6.3.4 above and are ordered on the X axis from lightest coloured to darkest coloured zones. Y axis: Au, Ag, Zn, Pb. Z axis: As, Cu.

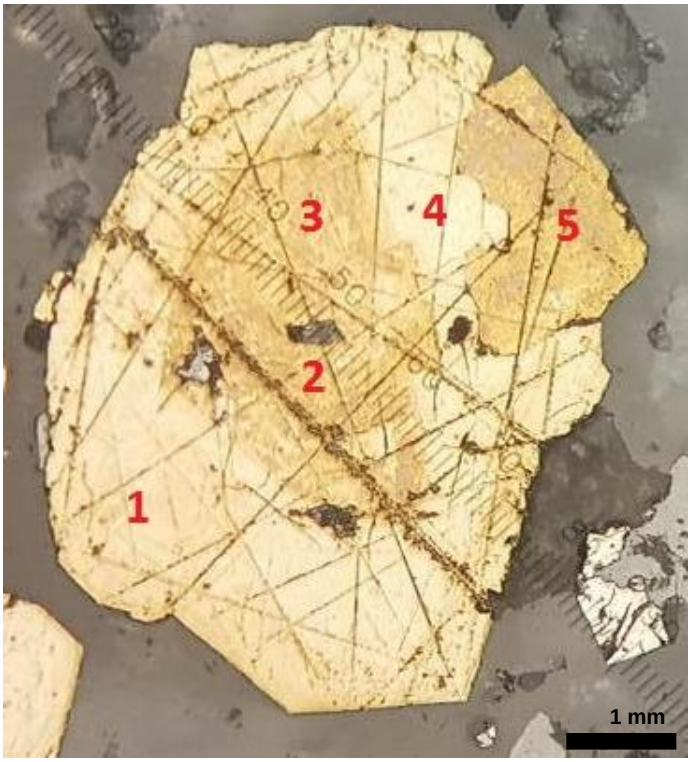

Figure 6.3.5: image of grain from sample AU57390B_Z2. The red numbers indicate the location of point analysis.

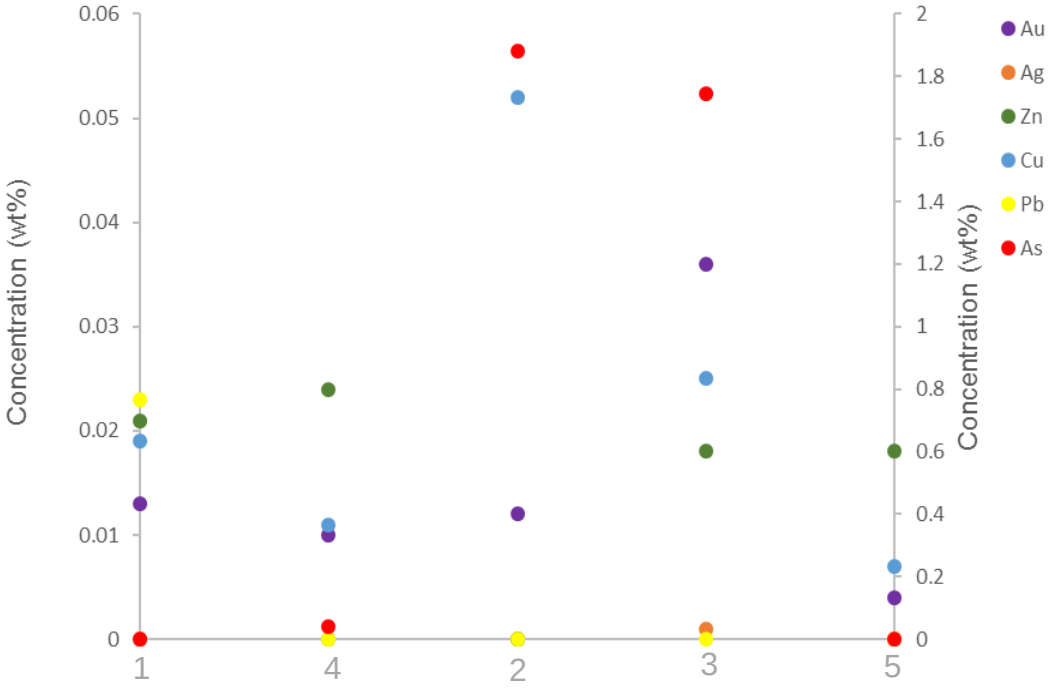

Figure 6.3.6: graph of element concentration across zones 1-7 on sample AU57390B_Z2. The numbers on the X axis correspond to numbered points on figure 6.3.5 above and are ordered on the X axis from lightest coloured to darkest coloured zones. As is on the Y axis, Au, Ag, Zn, Cu and Pb on X axis.

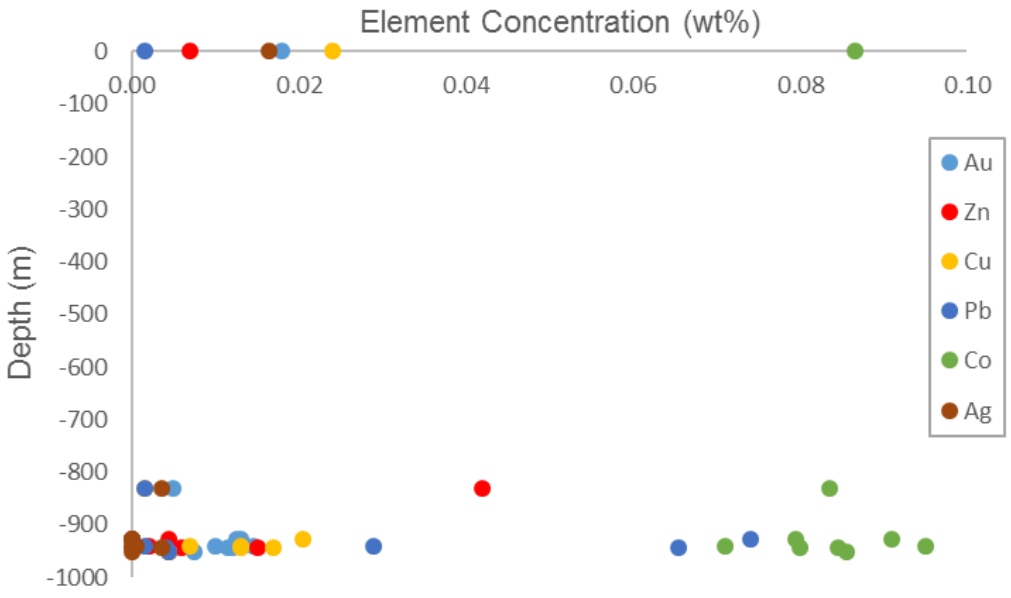

Figure 6.3.7: graph of the distribution of trace element concentrations with depth.

6.4 LA-ICPMS

Maps were made of trace element concentrations relative to Fe^{57} concentrations, assuming a pyrite matrix and concentrations of Fe 55.85 $gmol^{-1}$ and S_2 (32.07x2) $gmol^{-1}$. Samples were chosen based on the strength of their visual zoning seen in the textures. Each grain with internal zoning was analysed using LA-ICPMS to produce the images seen below. Some of the elements analysed appear to follow the same pattern as is seen in the reflected light microscope image. Yellow represents areas of high concentration, red represents areas of low concentration. All concentrations are relative to Fe^{57} concentration within the given sample. Areas of interest have been identified by blue circles on each grain photo, and corresponding location on the maps has been shown. Images are vertically squashed as a result of data processing by the software used. The data collected is semi-quantitative, as no sulfide standard was available at the time of analysis. A full table of data can be found in Appendix II, Raw Data, LA-ICPMS folder. The data has been interpreted based on relative concentrations, and is only compared within individual samples. Interest is focussed on the association of element distribution within individual grains, and is compared to the textural images from chapter 5, following bleach etching.

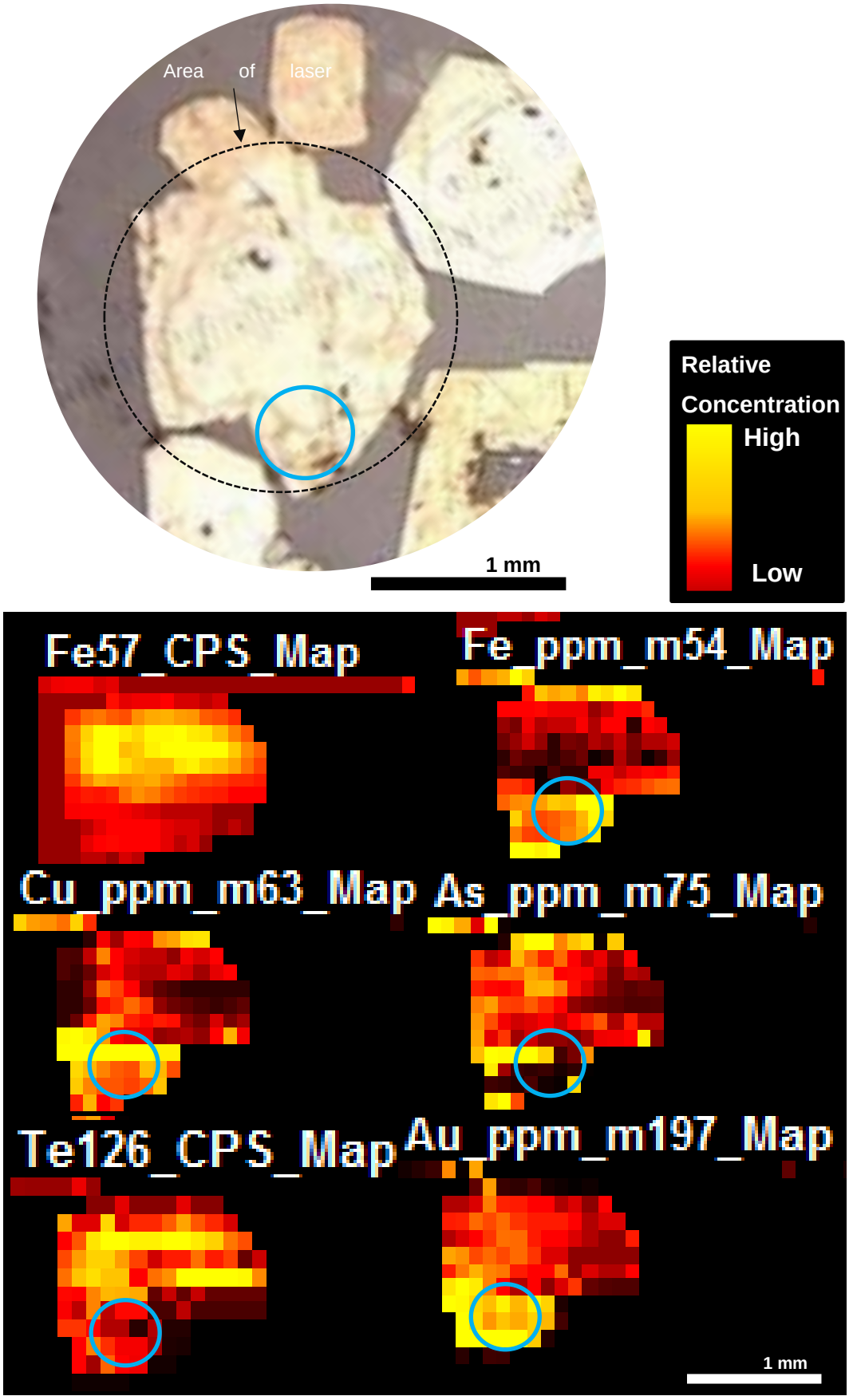

Figure 6.4.1: image of grain AU56192_Z1 and cell space maps produced from the LA-ICPMS analysis.

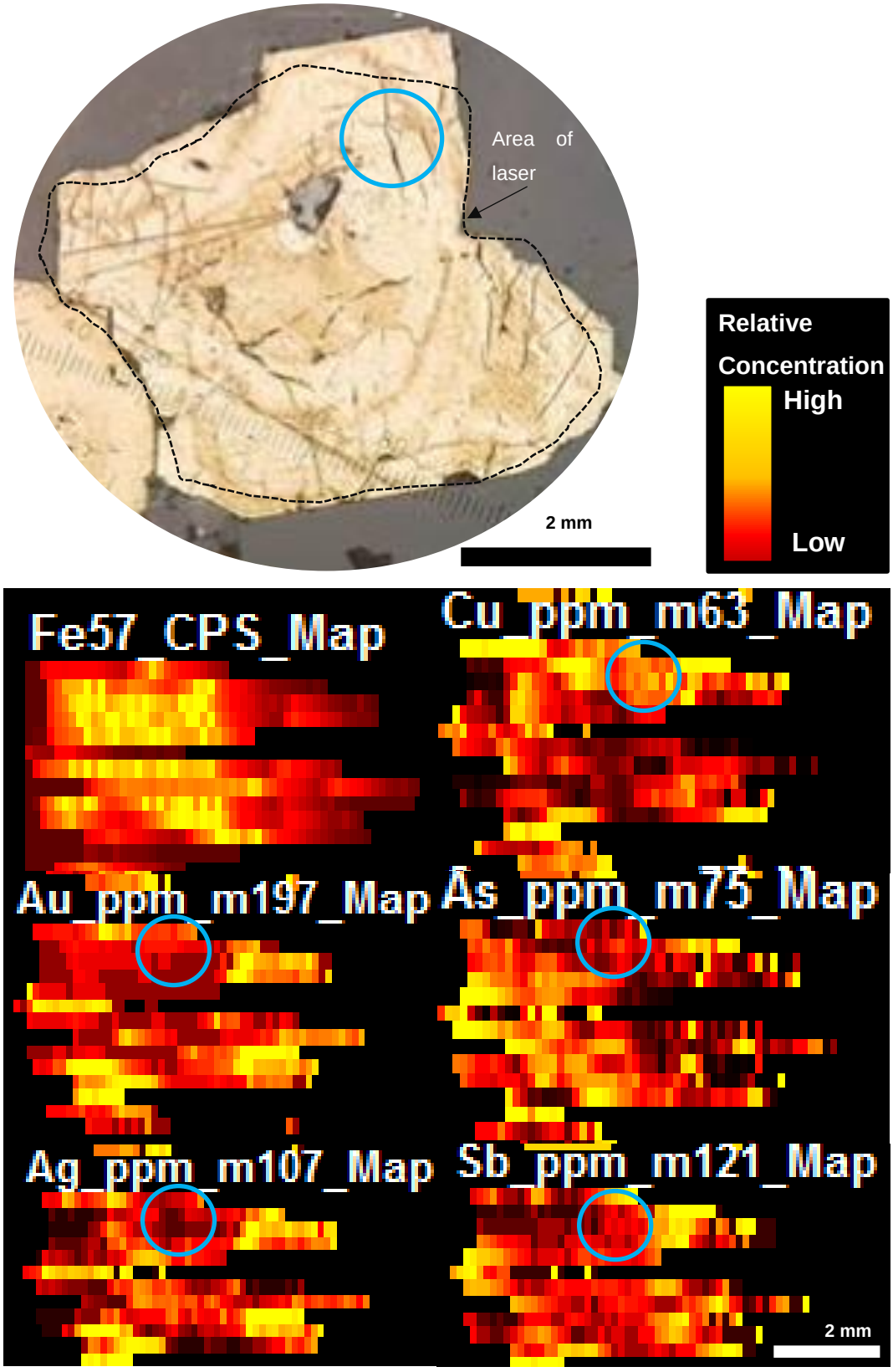

Figure 6.4.2: image of grain AU56192_Z2 and cell space maps produced from the LA-ICPMS analysis.

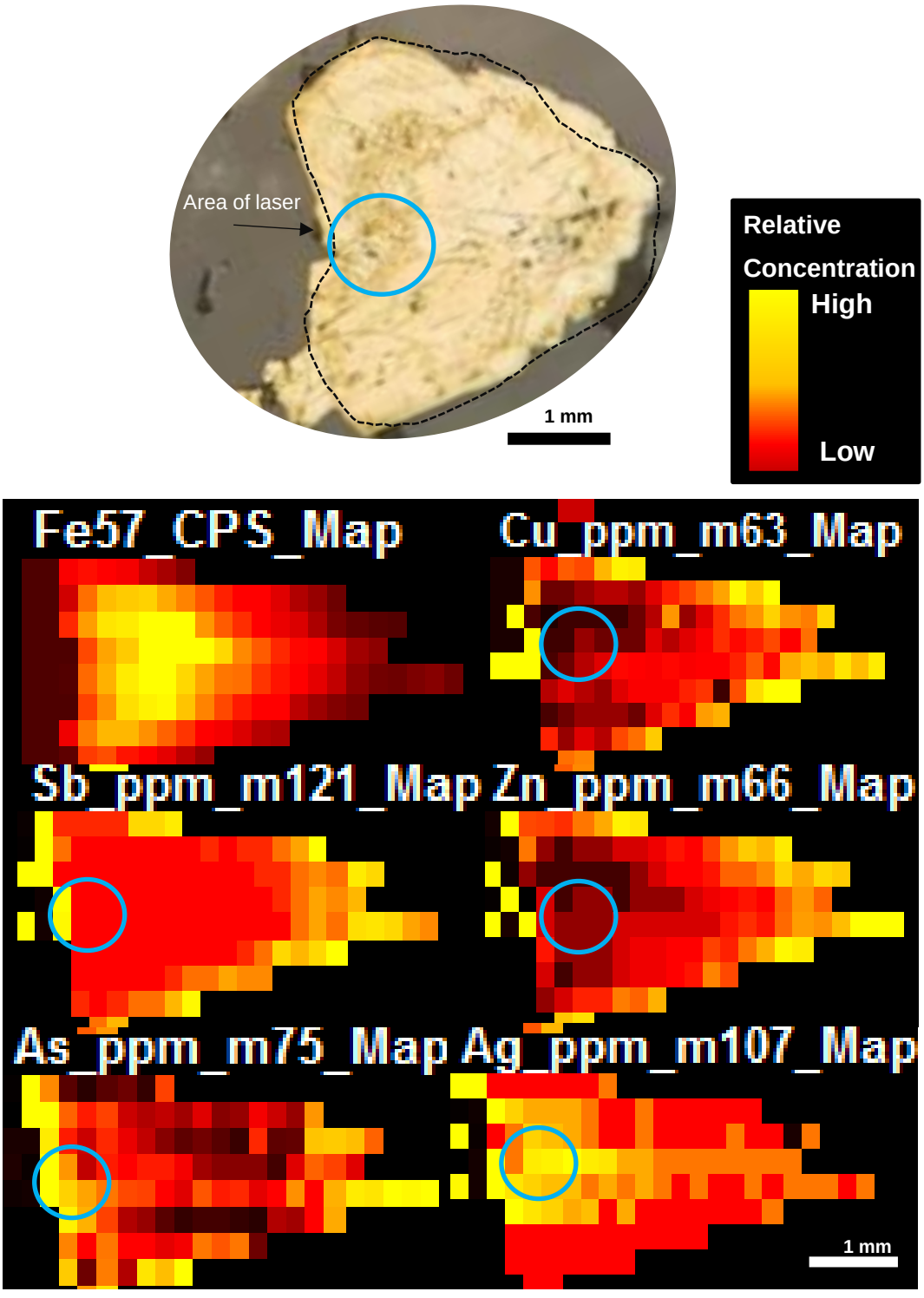

Figure 6.4.3: image of grain AU56192_Z3b and cell space maps produced from the LA-ICPMS analysis.

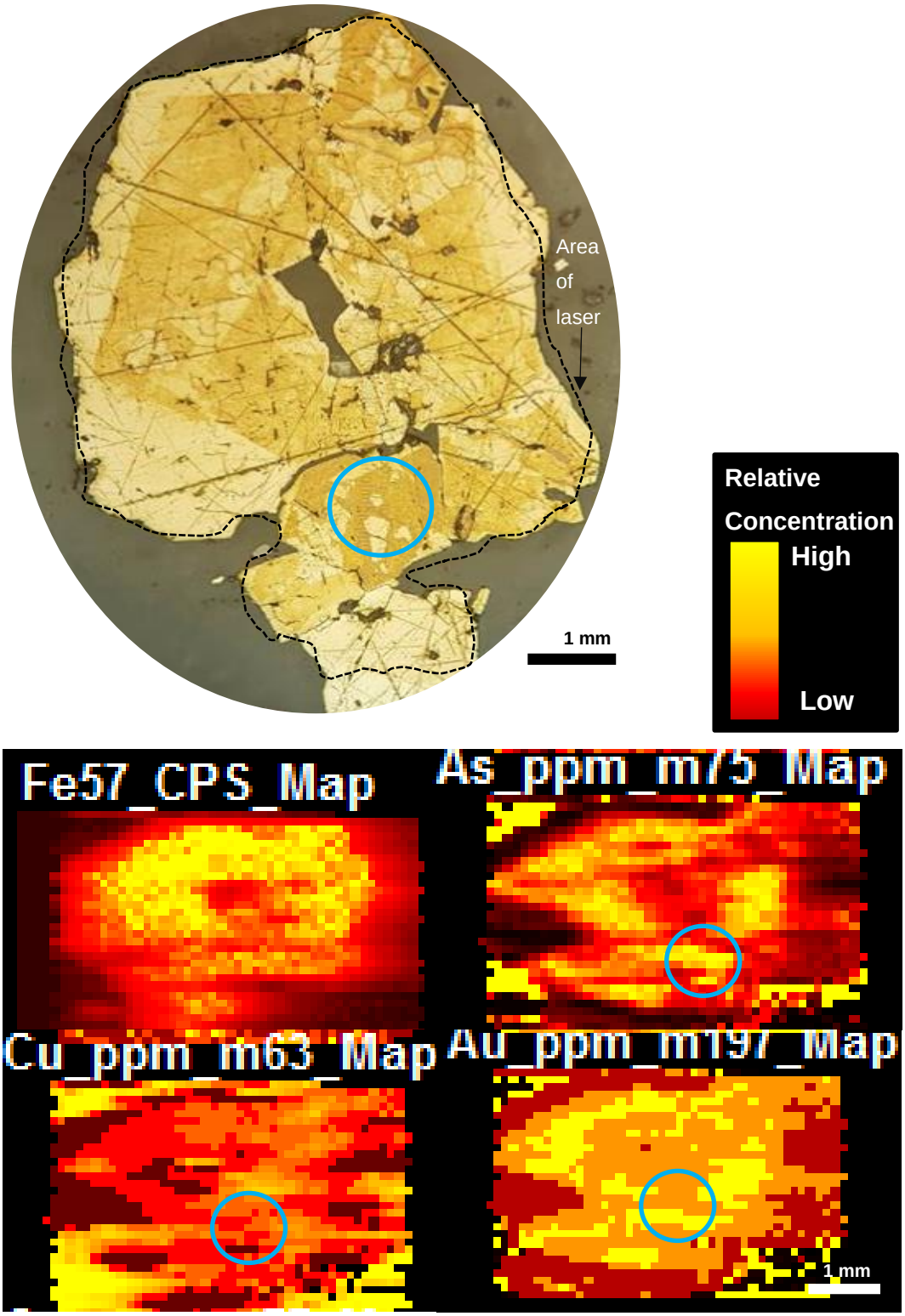

Figure 6.4.4: image of grain AU57390B_Z1 and cell space maps produced from the LA-ICPMS analysis.

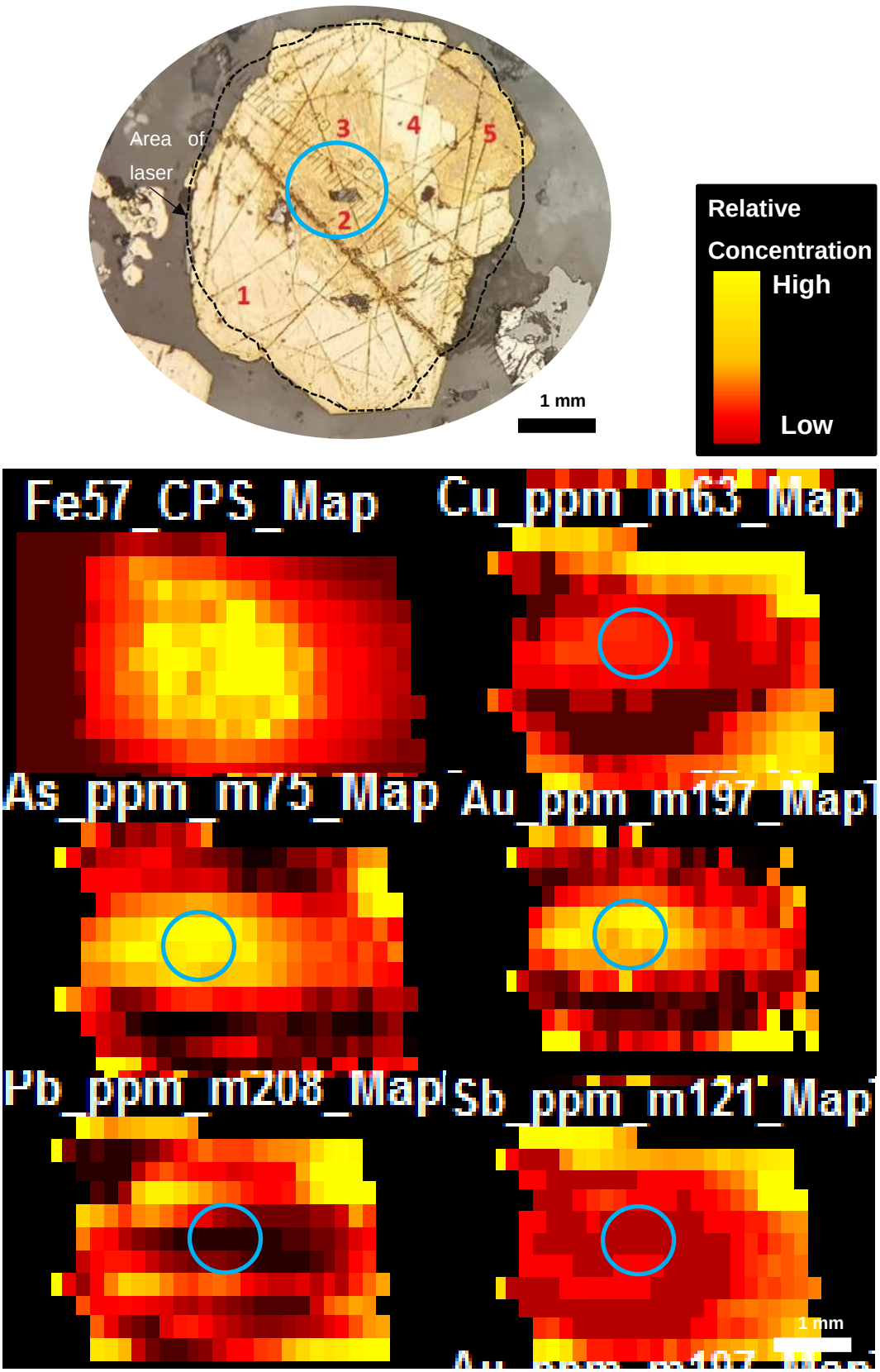

Figure 6.4.5: image of grain AU57390B_Z2 and cell space maps produced from the LA-ICPMS analysis.

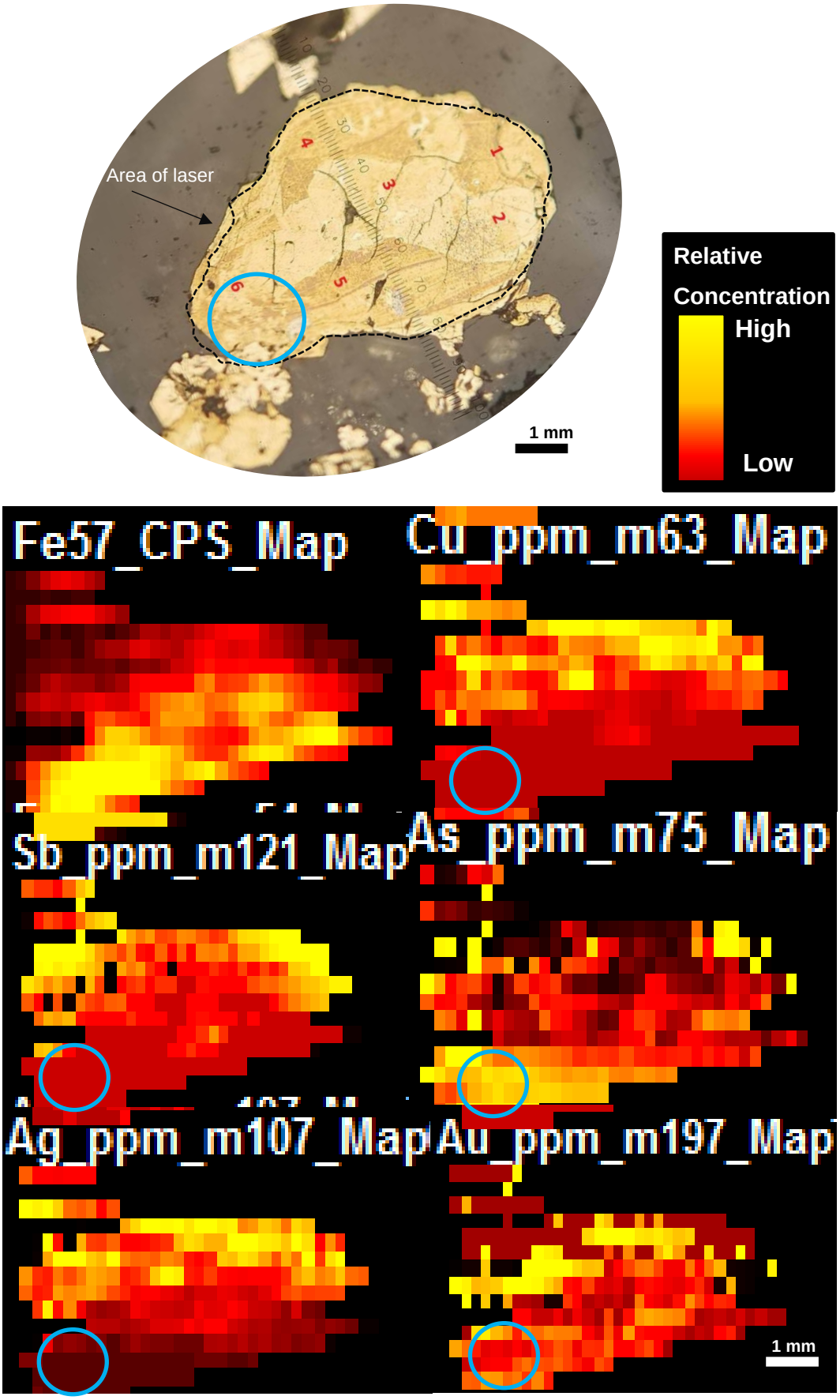

Figure 6.4.6: image of grain AU58144_Z1 and cell space maps produced from the LA-ICPMS analysis.

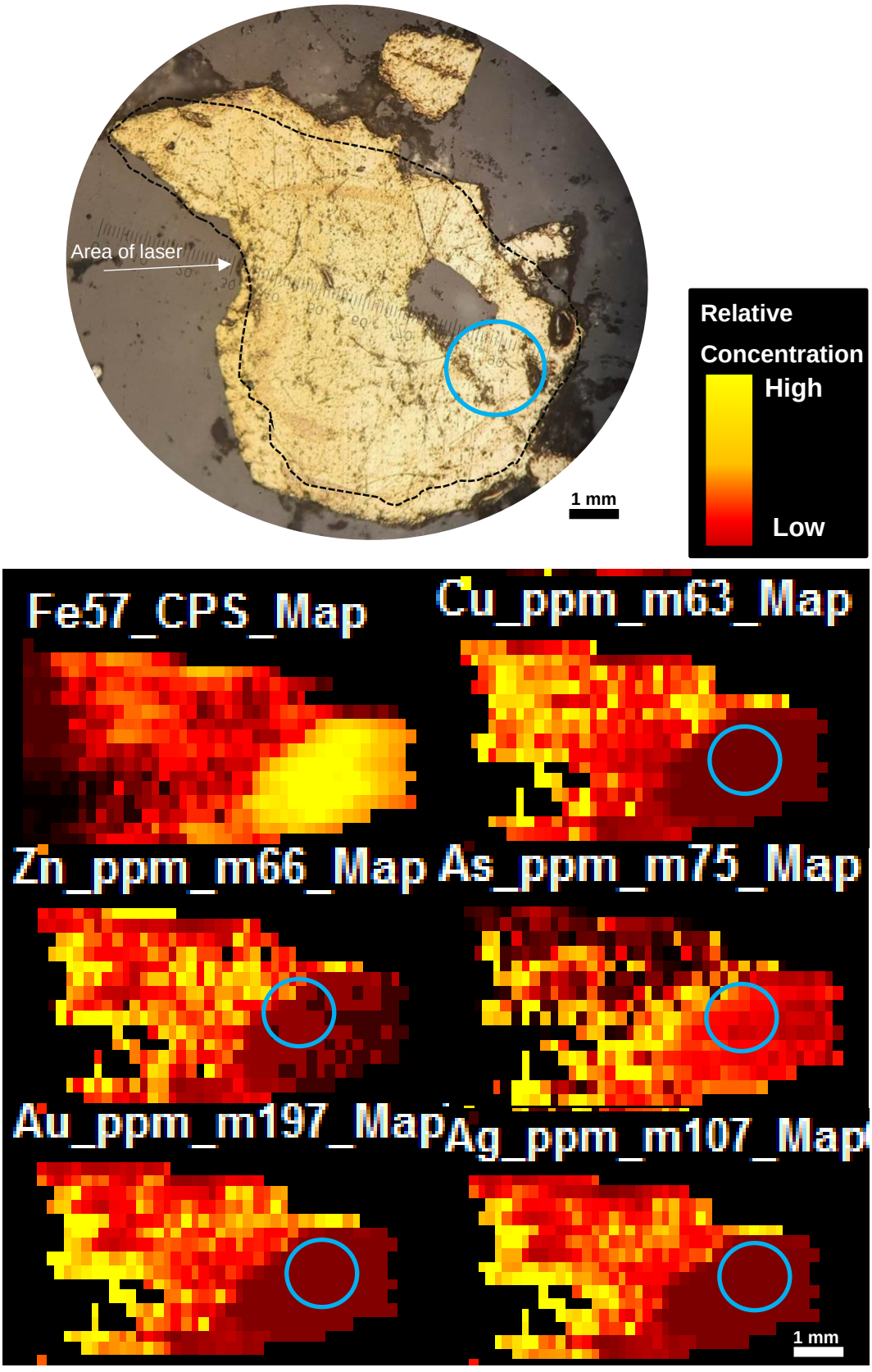

Figure 6.4.7: image of grain AU57414_Z1 and cell space maps produced from the LA-ICPMS analysis.

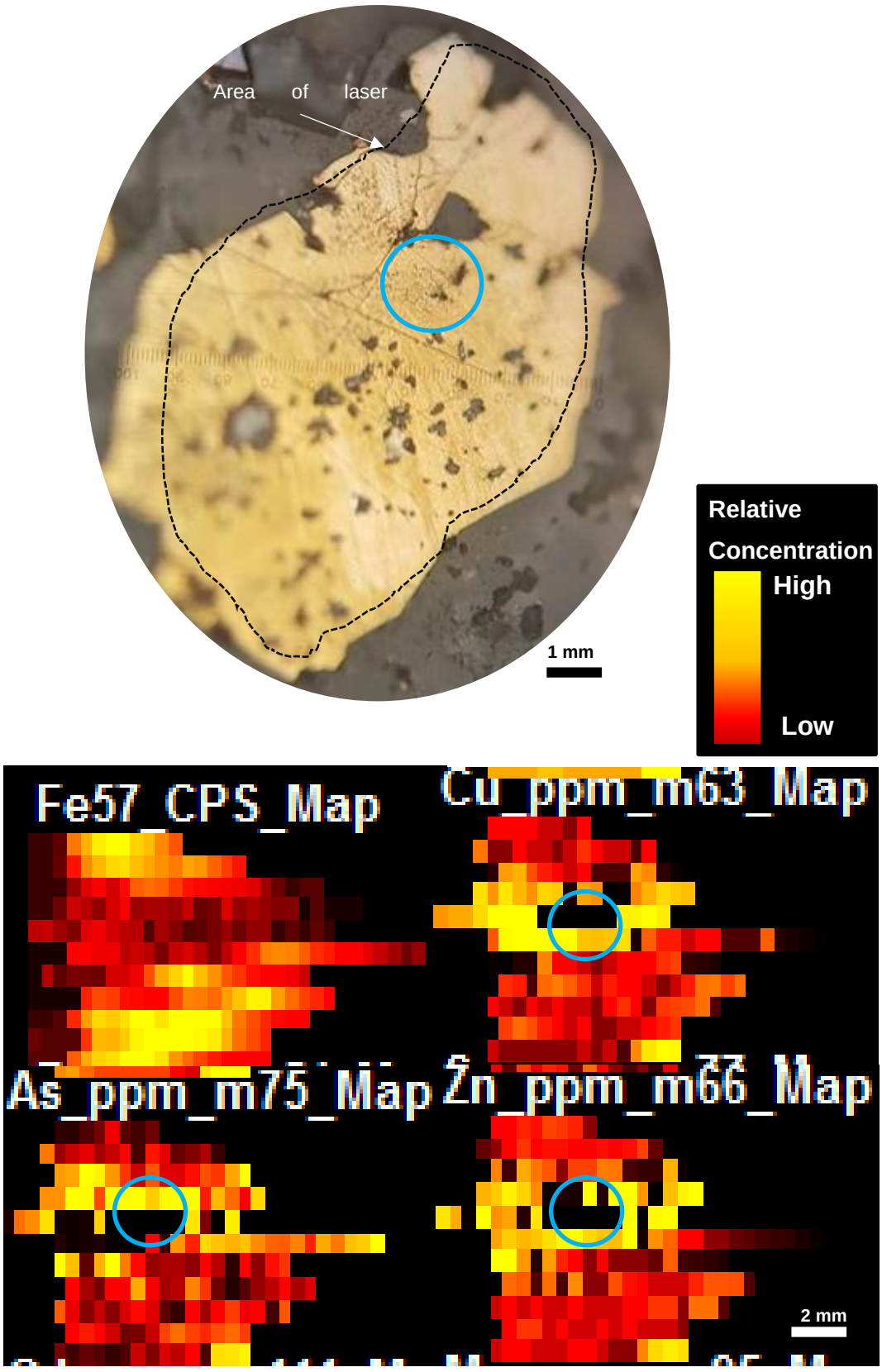

Figure 6.4.8: image of grain AU57417_Z1 and cell space maps produced from the LA-ICPMS analysis.

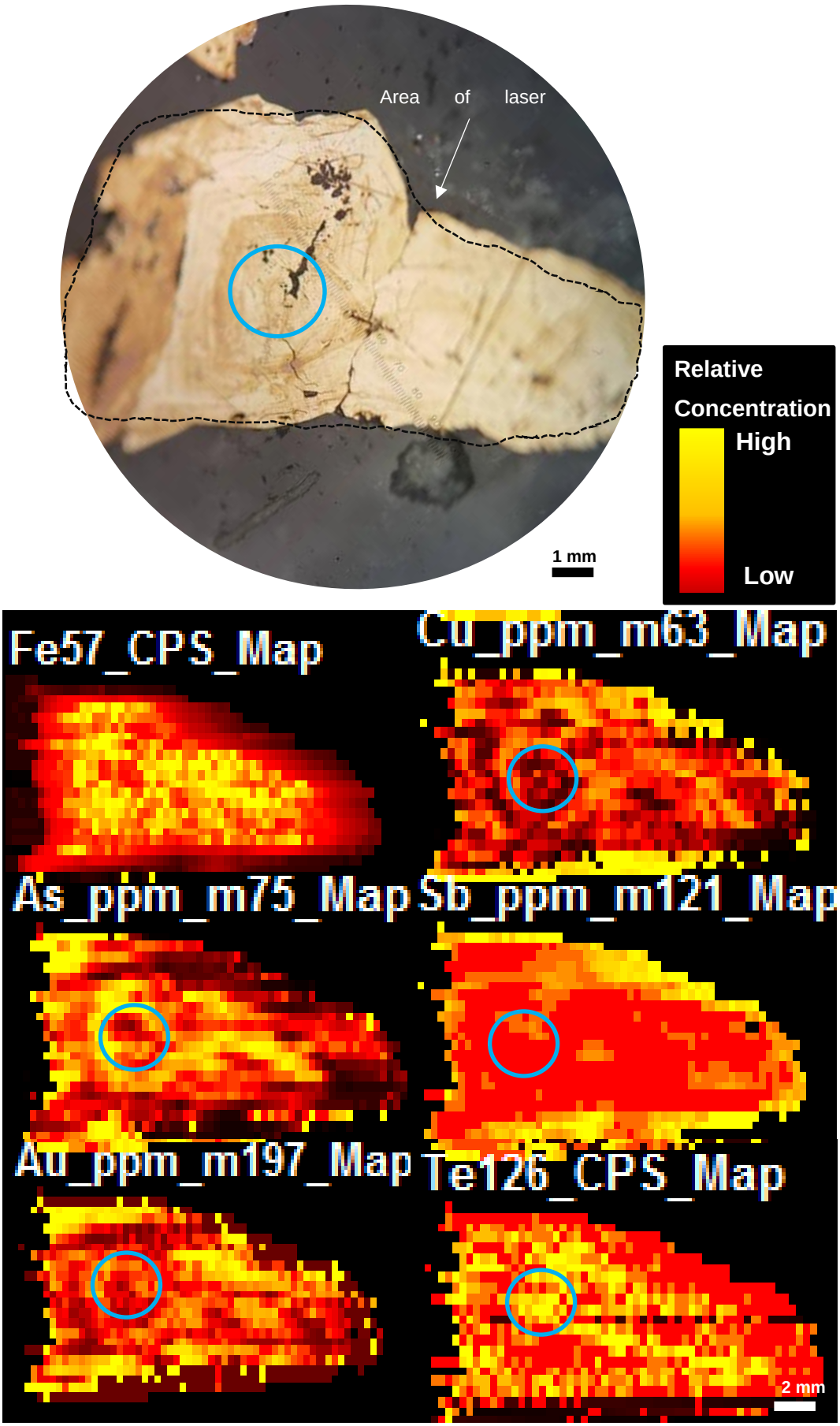

Figure 6.4.9: image of grain AU58148_Z2 and cell space maps produced from the LA-ICPMS analysis.

6.5 Discussion

Several applied methods of geochemical analysis on the pyrite grains showed that the pyrite at Waihi contained a wide range of trace elements, often associated with zoning patterns. Both the XFM and EPMA analyses showed there was a significant change in trace elements, including Au and Ag, between zones in some of the pyrite grains. The concentration of As, Zn, Cu, Te, Au and Ag varied within grains that showed textural variation under reflected light. The LA-ICPMS analysis revealed the variation in trace element concentration across individual pyrite grains, with As, Au and in some cases Zn and Cu, appearing to influence the textures observed under reflected light. Figure 6.4.9 shows the strong visual relationship between the relative concentrations of As and the textural characteristics. Figure 6.4.5 shows how Au and Cu influence different zones with an apparent negative relationship.

The XFM data showed that multiple As-rich and As-poor bands occur within individual grains of pyrite. The XFM data did not show high amounts of Au within grains, with the Au-rich regions occurring in the quartz matrix, outside the pyrite grains. This was expected, as the known metallurgy of the epithermal veins at Waihi states the bulk of Au is found in electrum (Brathwaite & Faure, 2002), and is recovered via the cyanide extraction process to the 93% level (Castendyk et al., 2005). However, both EPMA and LA-ICPMS mapping (although not fine enough to resolve all features) indicate that gold concentrations vary significantly between grains.

The EPMA results show that there is a chemical variation between the visible textural zones seen under reflected light microscopy. In all samples shown, the numbered zone in each grain that appeared the darkest in colour (i.e. least reflective or pyrite that takes the poorest polish) also had the highest trace element concentration. Most of the minor trace elements analysed for (such as Mo, Se and W) showed little variation between zones within samples.

The LA-ICPMS results showed the degree to which different elements affected the visible zoning of whole grains, seen under reflected light. The

changes in elemental concentrations generally correlate with one another. In all samples, As, Cu, Zn and Ag distributions correlated with the textures of the pyrite grain under reflected light. Some samples also showed Te, Sb and Pb in variable concentrations that also reflected the textural zones, as As does. Zones were either relatively high in all trace elements, or relatively low in all trace elements.

6.5.1 Element Behaviour

Other Elements

Other trace elements including Sb, Tl, Ga, Ni, Co, Mo, Bi, W, Se, Pb, Ca, Cr and Hg were also analysed by either EPMA or LA-ICPMS or both. The data for these can be found in Appendix II, Raw Data, EPMA and LA-ICPMS folders. The results are not mentioned here as in most cases they varied only slightly, or below detection limits.

Arsenic in pyrite

In all grains analysed, As appears to be the key influence for the zoning characteristics observed under reflected light that appeared as varying colour within the grain. Arsenic is also the element that varies the most in absolute abundance compared to all other major and minor elements found in pyrite (excluding the Fe and S). The same textural characteristics observed in the pyrite under reflected light are observed in the RGB images from the synchrotron data. The grains generally have a centre of As-rich pyrite, with an outer zone of As-poor. This zoning of As is seen in the previous chapter, as low As pyrite has better polishing quality than high As pyrite (Reich et al., 2013). The images in figures 6.4.4 and 6.4.5 above suggest that the pyrite grains examined had a trace element rich fluid during early growth, followed by a period of low trace element concentration for the later stages of grain growth.

As with the EPMA results discussed in the previous paragraph, the relative As concentration reflects the texture seen under reflected light better than any other element. Figures 6.4.4, 6.4.5 and 6.4.9 show that the map of As concentration relative to Fe^{57} concentration bears the closest resemblance to the image taken under reflected light. Again, the As concentration

appears to be highest in the centre of the grain, with a depleted As outer zone.

Out of all the elements analysed, As varied the most in concentration, with relative polish within a grain reflecting the As variation. However, between grains, the relative As concentration varies; polish only correlates within a grain and cannot be compared between grains. The EPMA analysis showed that the As occurred in poorly polished zones within grains. Figure 6.3.1 and 6.3.2 show that the As concentration in sample AU57390B_Z1 is highest in zone 4 at 1.9 wt% and lowest (BDL) in zones 1, 3 and 6. All zones of little to no detectable As are the paler, well polished zones. All zones of highest As are the darker, poorly polished zones. Cline (2001), Large et al., (2009) and Deditius et al., (2014) also found that high As in samples gave a poor polishing character, with high As grains polishing to a darker brown compared to the pale yellow expected of pyrite under reflected light microscopy.

Baker et al. (2006) found similar As zoning in pyrite from Pajingo (seen in figure 6.5.1.1 below), another low sulfidation epithermal system. The type of zoning is similar to the zoning seen in the backscatter image from sample AU56192_Z1.

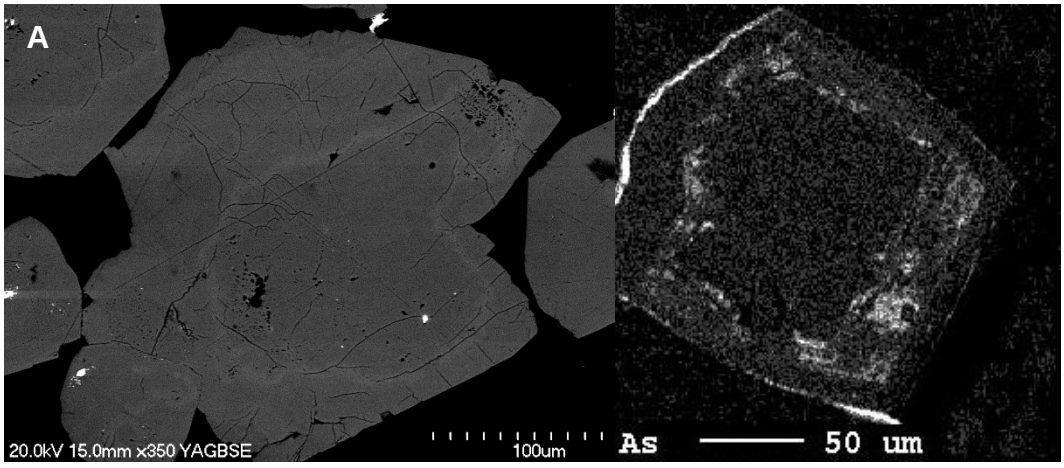

Figure 6.5.1.1: A- SEM backscatter image of zoning in sample AU56192_Z1. B- Microprobe image of As zoning in a pyrite from Pajingo (Baker et al., 2006).

Baker et al. (2006) found that within the Pajingo system, Mo and Ag displayed a systematic pattern of variation between different alteration zones. They suggest that Mo could be transported in a similar way into pyrite as As, Au and Sb is. Baker et al. (2006) suggest that the trace element analysis indicates that the Mo and Ag in the pyrite came from the fluid, while the Pb came from host rock. They do not mention As variations within grains, other than in the example given above (Figure 6.5.1.1).

Copper, Zinc and Lead in pyrite

Overall, Cu and Zn concentrations are much lower than As. Waihi is an unusual gold-silver base metal sulfide-quartz vein system due to the large vertical extent of 575 m that economic Au-Ag ore is found at (Brathwaite & Faure, 2002). With a decrease in depth there is a change from Zn-Pb sulfides to Zn-Pb-Cu-Ag sulfides and electrum. In higher salinity fluids, Zn, Pb, Cu and Ag are known to be transported as chloride complexes at 350 - 200°C. In lower salinity fluids, Au, Ag and Cu are transported as hydrosulfide complexes between 250 - 200°C (Brathwaite & Faure, 2002). All the samples in this study were taken between 927.5 m RL and 952 m RL, with the exception of AU56202 which was at 0 m RL and AU60281 which was 830 m RL. Sample AU60281 which was shallower at 830 m RL, and the sample from Cowshed, contained the highest Cu concentrations of 4.5 wt%, with every other sample's Cu concentrations well below 1 wt%. Sample AU60281 also contained the highest Zn concentrations, with a maximum of 1.8 wt% which is 0.8 wt% higher than any other sample. AU60281 also contained the highest Pb readings of 1.8 wt%, with all other samples below BDL. The deepest sample, AU57417, contained average concentrations of all elements. As suggested by previous studies, the shallowest non-surface sample showed the highest Cu concentration (Brathwaite & Faure, 2002). Brathwaite & Faure (2002) show that with a decrease in depth, Cu and Ag sulfides, and electrum, begin to form along with the Zn and Pb sulfides from deeper regions. The Cu and Ag sulfides can form as a decrease in depth stabilises the hydrosulfide complexes as they mix with a more saline fluid (the result of deep chloride fluid and steam

heated meteoric water). The deepest sample had Cu concentrations below the BDL, and very low (near BDL) concentrations of Au and Zn.

The Cu in pyrite is likely to substitute the Fe in octahedral sites, where the crystal structure of the pyrite has previously been distorted by the presence of other elements such as As, Sb or Co (Reich et al., 2013). The Waihi system is known to have a high concentration of Cu (Brathwaite & Faure, 2002, Fyfe, 2014) and chalcopyrite was very common in a lot of the samples analysed. Chalcopyrite is known to have formed alongside quartz, galena, pyrite and sphalerite during the early to mid hypogene stages of the Waihi epithermal system (Fyfe, 2014). Electrum-poor mineralisation at Waihi includes sphalerite, galena, pyrite and chlorite, and little or no chalcopyrite, and occur at depth (Christie et al., 2007, Fyfe, 2014). Therefore, samples with higher Cu present can be assumed likely to also be Au-Ag rich (Brathwaite et al., 2005, Fyfe, 2014).

The zones in pyrite containing the highest Zn concentrations are the darker, dirtier zones seen under reflected light. Figure 6.3.4 shows that the highest Zn concentration observed in sample AU58203_Z1 is 2500 ppm (0.25 wt%), one of the darker, dirtier zones of pyrite. All other EPMA points are below detection limit (BDL) and are in zones that are lighter and do not have the dirty texture seen in the zone labelled point 4.

In sample AU56192_Z3b, the Zn occurs in the same distribution as the Cu. In some cases, the Zn and Cu appear to have a positive relationship. However, in other grains such as in figure 6.3.6, the Zn levels are constant across the whole grain, while the Cu levels change with the textures observed under reflected light.

Current knowledge of the Waihi mineralogy may be reflected in the trace element chemistry of the pyrite grains observed. Figure 6.5.1.2 below shows the distribution of Zn, Cu and Pb maximums from all the samples relative to their depth. The result of the Cowshed sample (also the shallowest sample) AU60281 with the highest Cu concentration, and the deepest sample AU57417 with no Cu provides the evidence for the theory that there is a relationship between the base metals in the pyrite on a vertical level within

the Waihi system. However, to further support this statement, more samples should be taken with special interest to sample context.

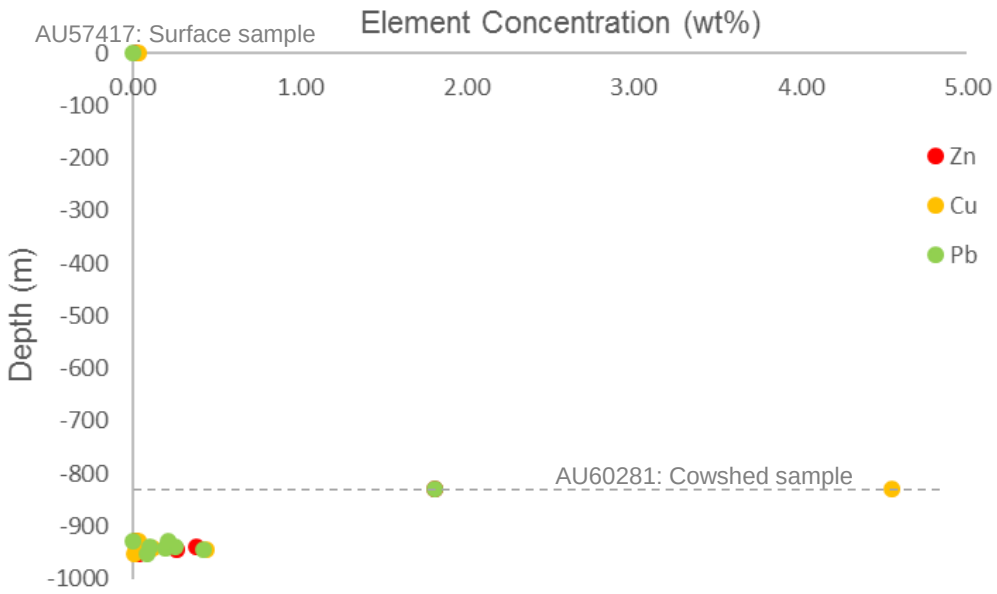

Figure 6.5.1.2: graph showing the maximum concentrations of Zn, Cu and Pb against depth. The dotted line indicates the Cowshed sample.

The fact that the Cowshed sample is highest in Cu suggests different mineralisation between the Martha deposit and the Cowshed. Samples need to be taken down individual drill holes at specified depths to allow for comparison between drill holes as well as within the drill holes themselves. Multiple drill holes allows for replication of results and will tell local versus regional conditions.

Trace element analysis can be used to determine whether the pyrite grains formed from fluid that was either high temperature and a chloride complex, or low temperature and hydrosulfide complex. Grains with a higher concentration of Zn, Pb, Cu, Ag and electrum indicate deep chloride rich fluids have been mixed with steam heated ground water. This is due to the increased stability of hydrosulfide complexes as a result of this mixing process (Brathwaite & Faure, 2002).

Silver in pyrite

The RGB images indicate the behaviour of Ag within the sample. In figures 6.2.8, 6.2.9, 6.2.10 and 6.2.11 the Ag is sitting outside of the pyrite grains, in the quartz matrix surrounding the pyrite crystals. Unike As, the Ag does not occur within the pyrite, as part of the crystal.

The EPMA showed that the Ag was highest in dirty zones, with a concentration of 1.8 wt% Ag in zone 5, which appears to be a very dirty, grey zone within a grain.

Overall Ag concentrations from the EPMA analysis were low, mostly below BDL.

The LA-ICPMS also showed low overall concentrations of Ag in the pyrite. The maps of Ag in figures X, Y and Z slightly resemble the Au maps in the same figures, but with a much lower overall concentration.

Gold in pyrite

The RGB images from the synchrotron show that the highest concentration of Au appears to be outside the pyrite, in the quartz vein, which is expected as most of the Au and Ag occurs as electrum in the Waihi system (Brathwaite et al., 2005). The Au is also present in some of the more irregular shaped pyrite grains, occurring in blebs, but not common.

The Au occurs with the Ag, outside the pyrite grains. The Au does not occur with the As in the quartz matrix. As figures X and Y show, where Au is present outside of the pyrite, As is absent.

EPMA analysis shows that the Au occurs in certain zones observed under reflected light. The Au found within pyrite occurs in highest concentrations in the dirty, darker coloured zones within the grains. The palest zones hold the least Au.

The relationship between As and Au in pyrite has been looked at in a variety of settings, including hydrothermal ore deposits. Deditius et al. (2014) suggest that Au-bearing pyrite is common due to its ability to form in many different physio-chemical conditions. Deditius et al. (2014) look at data from

samples from a wide range of deposit types including Carlin-type, epithermal, porphyry Cu, Cu-Au and orogenic Au, volcanic hosted massive sulfide (VHMS) and iron oxide copper gold (IOCG) deposits. In Carlin-type deposits, arsenian pyrite is the main host for Au (Deditius et al., 2014), with invisible Au concentrated in pyrite grains less than 10 μm wide, and significant amounts of Cu, Hg, Sb and Tl (Barker et al., 2009). Unlike the Waihi pyrite, the Au-As rich zones of pyrite are precipitated onto trace element poor, pre ore pyrite (Deditius et al., 2014). The pyrite at Waihi can be assumed as a representation of the Au/As signature of the mineralising magmatic-hydrothermal fluids present during the systems active period, also influencing the metal ratios in the Waihi system (Deditius et al., 2014).

In the work done by Reich et al., (2010) it is suggested that the deposits of invisible gold are in pyrite with a high As concentration. The EPMA and LA-ICPM results also suggest this, as in the case of the EPMA data, no pale zones within grains had high concentrations of As or Au, indicating the Au is correlated with the As. The LA-ICPMS maps also show that where Au concentration is relatively high within the grain, the distribution resembles the texture observed under reflected light (see figure 6.4.4 and 6.4.5). The LA-ICPMS results show grains with high relative As and Au concentrations show strong resemblance to reflected light microscopy zones. This can support two theories; the first being that As concentration affects the presence/deposition of Au and Ag in a system (Reich et al., 2010). The second being the Au and other trace metals are controlled by abundance of supply in the hydrothermal fluid (Simmons et al., 2016).

6.5.2 Chemistry and Growth

During the growth of the pyrite grains, the chemistry of the fluid has altered, changing the internal chemistry of the pyrite crystals growing from that fluid (Huston et al., 1995). The pyrite analysed is dominated by grains with an As-rich early growth stage. The inner, As-rich zone is observed in grains from the XFM, and in several of the EPMA and LA-ICPMS analyses.

The grains analysed all display different chemistries. There is As present in all the zoned grains, while other trace elements such as Cu, Zn, Te, Ag and Au are absent in some.

Unlike in other systems, the Waihi pyrite does not appear to have a consistent pattern of trace element zoning (Large et al., 2009). Almost every grain is different to some degree, with no noted correlation with depth, wall versus vein pyrite, crystal form and pattern. As mentioned in chapter two, the enrichment of Tl in colloform pyrite often indicates rapid precipitation, with increased concentrations of Au and As incorporation (Huston et al., 1995). However, the LA-ICPMS data for Tl, which can be found in Appendix II, Raw Data, was not in high enough resolution to determine whether this trend was observed in the colloform pyrite in the Martha deposit.

In the previous chapter distinctions were made highlighting the different types of zoning. Some zoning was radial and inclusion-rich such as the concentric zoning described in Chouinard et al. (2005) where there was an internal zone of high As and other trace elements surrounded by an outer, low trace element pyrite. Chouinard et al. (2005) also observed sector zoning, where crystal faces of the same grain had varying trace element concentrations. Figure 6.5.2.1 shows a pyrite grain with sector zoning from the Pascua deposit (Chouinard et al., 2005). The zones of higher trace element concentration are paler in colour. There appears to have been favourable crystal faces for trace element incorporation, along with unfavourable faces, producing sector zoning in the grain. Chouinard et al. (2005) suggest that there is a favoured orientation of grain to fluid flow that aids in trace element incorporation. The comparison of the same zoning type observed in both the Pascua pyrite and the Waihi pyrite suggests that

sector zoning is the result of pyrite forming with trace element rich fluid, in an epithermal setting.

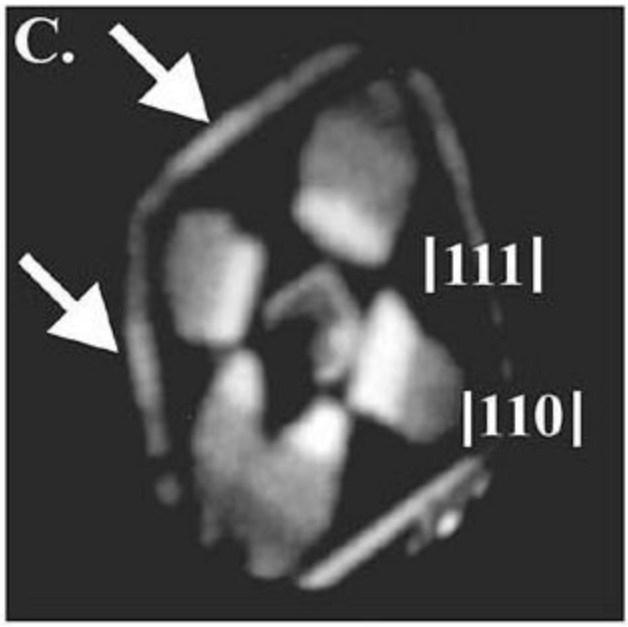

Figure 6.5.2.1: image of a pyrite grain from the Pascua deposit that exhibits sector zoning. The white arrows are suggesting a favoured orientation for the incorporation of As into the [111] stage pyrite (Chouinard et al., 2005).

In the studies by Chouinard et al. (2005), Baker et al. (2006) and Large et al., (2009) pyrite is described as having two zones, one high As and one low As, suggesting hydrothermal fluid supply is the main control on trace element chemistry (Reich et al., 2013). The samples analysed at Waihi have shown to be more complex, with varying amounts of zones in different grains. Sector zoning clearly illustrates crystal face control on the uptake of trace elements by the erratic and irregular nature of the zones found in the Waihi pyrite, compared to those analysed by Chouinard et al. (2005) and Large et al. (2009). Trace element distribution reflects the restrictions on the grain during growth in a trace element rich fluid period. Grains with a favoured side of trace element rich zones could have experienced constricted growth on the opposing side, otherwise there would be a more regular distribution of trace elements across the grain. A favoured crystal face for trace element incorporation could also be due to porosity at the location of the grain during growth, reflecting growth into an open space.

6.5.3 The Independence of Gold

in comparison to what Deditius et al., (2014) found in other hydrothermal systems, there appears to be no coupling between Au and As incorporation, or Au and Ag with Cu, Zn, and Pb in pyrite at Waihi. Where there is As in the pyrite, Au is also present. However, as the As concentration increases, the Au concentration remains the same, as seen in Figure 6.5.3.1. There is also Au present where there is no As.

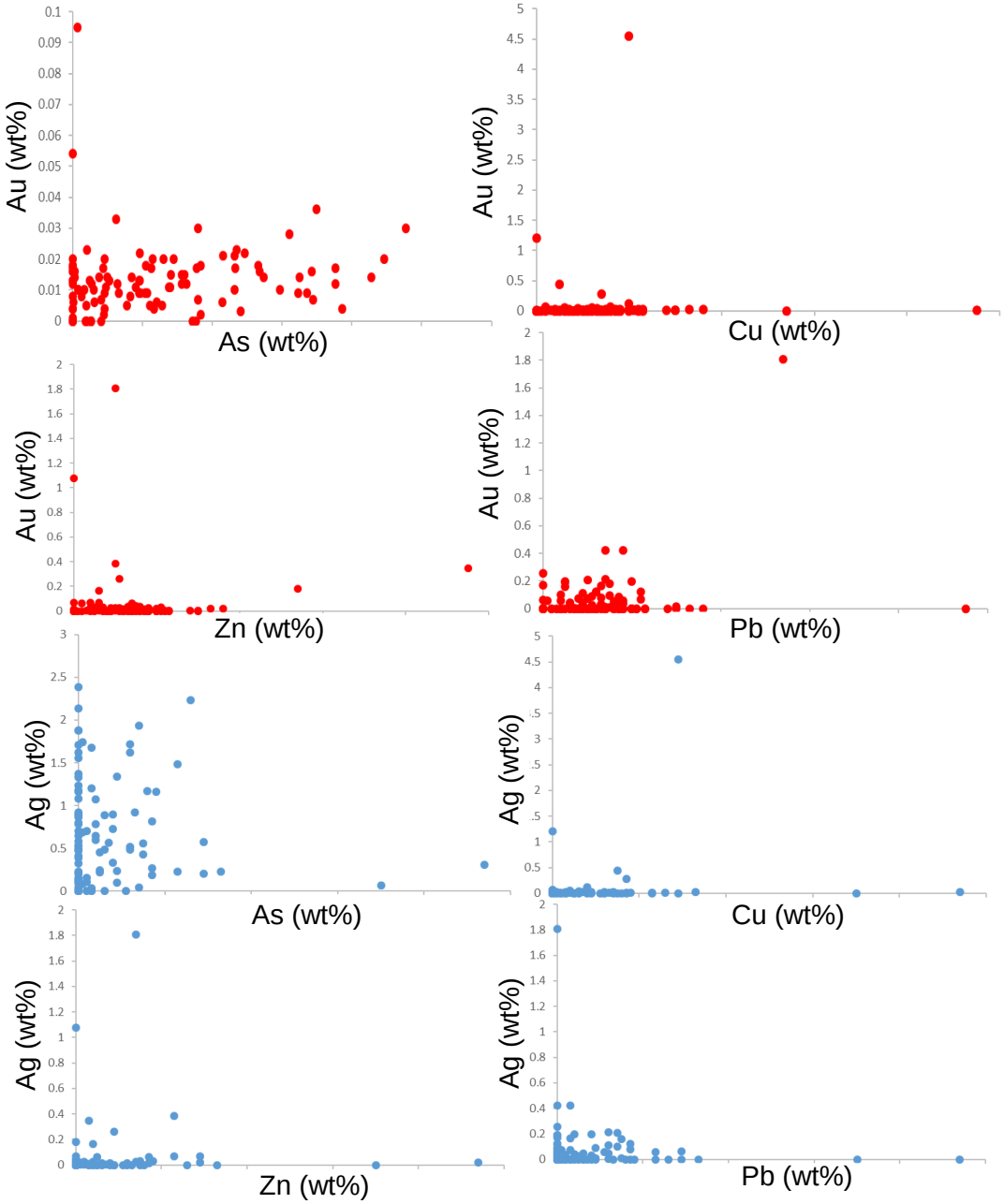

Figure 6.5.3.1: Graphs of the relationship between Au and As, Cu, Zn, Pb and Ag and As, Cu, Zn, Pb.

In high sulfidation epithermal systems oxidised As and Au are incorporated due to the higher fO_2 conditions (Simmons et al., 2005). Au occurs mostly as nano-particles of native metal, while As occurs mostly as the form As^{-1} in pyrite, with $As^{2+, 3+}$ forming also due to the favouring oxidising conditions of high sulfidation systems (Deditius et al., 2014). In low sulfidation epithermal systems, there is a lower oxidation state, with H_2S being the main transporter and facilitator for gold formation (Simmons & Browne, 2000).

Au does not appear to be affected by the presence or absence of other trace elements. There is no positive relationship between Au and As, which has been seen in other studies (Chouinard et al., 2005) nor is there a negative relationship. The Au distribution in the LA-ICPMS maps appeared in some grains to reflect the textures observed under reflected light, but not in all cases. This could be due to the resolution of the LA-ICPMS analysis. A smaller spot size would be able to produce maps of a higher resolution, showing in more detail the Au distribution (Deol et al., 2012).

The unexpected behaviour of Au could be due to a number of reasons, and the possible theories are outlined below. The key questions to be answered are; why does there appear to be a limited amount of Au? Does any element play a role in Au presence or concentration? Can conditions from other system types be applied? Firstly, any crystallographic controls on Au presence will be considered, followed by a discussion on the limitations of temperature and the original Au concentration at the Au source.

Crystallographic Controls

The coupled theory of As and Au in pyrite. This theory suggests that the presence of Au is due to the presence of As. As and Au are favourably incorporated into pyrite when As incorporation distorts the pyrite (Deditius et al., 2014). However, in the results shown above in figure 6.5.3.1, Au occurs in some samples without any As, and there is no positive or negative relationship between Au and As, possibly a very weak positive relationship. This coupling theory can be rejected based on the lack of relationship displayed in the data above(Simmons & Browne, 2000).

The theory based on crystallographic controls has been documented to occur in the ore-stage pyrite from the Pascua high-sulfidation epithermal deposit in Chile. In the pyrite from Pascua, almost identical zoning patterns of As and Ag has been interpreted as occurring as a coupled substitution (Chouinard et al., 2005). Chouinard et al. (2005) also found that the zonation of Au and other trace elements was evidence that there was crystallographic structural controls on the pyrite grain surface during trace element incorporation. In the Au-bearing pyrite from the Pascua deposit, the Fe^{2+} is substituted with an As cation, and incorporation is coupled with Ag (Chouinard et al., 2005). This has also been documented as occurring in other systems (Chouinard et al., 2005). In the pyrite from Waihi, a strong sectoral correlation between As and Ag is not seen, further supporting the idea that trace element incorporation is not under crystallographic control. However, there are strong correlations between sectoral zoning and As alone, as demonstrated in the XFM section above, (figures X, Y and Z). This suggests that something other than As is controlling the incorporation of Ag.

Temperature Controls

The temperature of the system limits Au concentration (Deditius & Reich, 2016). The solubility of As in pyrite is negatively affected with an increasing temperature. This means that Au concentration must also decrease with increasing temperature, as Au is incorporated when the pyrite is distorted by the incorporation of As (Reich et al., 2012). The results above show a range of concentrations of Au across the samples from BDL to 500 ppm. The Waihi system is known to have experienced temperatures of around 200 – 350°C (Brathwaite & Faure, 2002) which are considered moderate to low temperatures. This theory of temperature control can be considered plausible, as there are varying concentrations of Au in the pyrite. It is also interesting to note the electrum bearing sulfides at Waihi are known to have formed between 215 – 255° C (Brathwaite et al., 2005), implying the variation in Au reflects a change of no more than 40°C.

Boiling Controls

Boiling conditions limit Au incorporation. The mechanism for the deposition of Au is the change in state of the fluid due to mixing, or encountering a permeable zone inducing boiling and/or volatile phase separation. Au is deposited depending on the stability of the Au containing ions in the new conditions (Seward, 1993). The colloform and crustiform textures in the quartz found in these samples is indicative of boiling having occurred (Brathwaite & Faure, 2002). Therefore, the variations in Au in pyrite may be a reflection of the changes in boiling horizon over time. For example, at or above the boiling horizon more Au is incorporated into electrum, while below the boiling horizon there is likely to be enhanced Au incorporation into pyrite (Simmons et al., 2005). As a variable concentration of Au is observed, this hypothesis cannot be rejected.

Source Controls

Au supply is limited. It is possible that the amount of Au in the system is limited. In this case the variations in Au concentration seen in the pyrite are due to the varying Au concentrations in the supply fluid. It can be assumed that there was enough As present during the pyrite growth in all the samples to encourage Au incorporation, as Au incorporation is seen in all samples with As present (Deditius et al., 2014). Therefore, assuming this theory cannot be discounted, the pyrite is an accurate record of the Au concentration in the fluid during the pyrite formation, something which has been suggested to be possible in porphyry copper systems using similar research methods (Reich et al., 2012).

Chouinard et al. (2005) suggest the mechanisms behind Au incorporation are influenced by Au atom size relative to As atom size. Au^{+} has a radius of 151 pm while Au^{3+} has a radius of 99 pm. The radius of the Fe^{2+} ion being replaced is only 75 pm. Chouinard et al. (2005) suggest that for Au to be incorporated into the pyrite structure, it must be coupled with Cu^{+} (91 pm), as then Au^{3+} (99 pm) + (91 pm) $\leftrightarrow$ $2Fe^{2+}$ (150 pm). At Waihi there are varying concentrations of Cu; some grains with BDL in all zones. The possibility of the high oxidation conditions favouring this reaction needs to

be taken into account in high sulfidation systems. Waihi is a low sulfidation system so that can explain why different element associations are observed (Brathwaite & Faure, 2002).

Added to this is the recent account of the Marianas-San Marco low sulfidation epithermal system in Argentina. Vidal et al. (2016) found that multiple episodes of vein infill occurred during the system's active lifetime; An initial low volume metal-rich episode followed by an extended quartz episode with minimal mineralisation, followed by a barren episode before finally an Ag-rich episode. Considering the evidence of Vidal et al. (2016) and the theories discussed above, the chemical evolution of the Waihi system during pyrite formation can be assumed to be much more complex than others such as Bendigo and Carlin-type (Large et al., 2009). As Baker et al. (2006) show, S plays an important role in Au transport in low sulfidation epithermal systems such as Pajingo and Waihi. It may be that the varying H_2S gas concentrations contribute to the complexity of the Waihi system, instigating and repressing sulfidation and growth of pyrite whether it is abundant or rare (Baker et al., 2006). The variety of textures observed and resulting chemistry of zones suggests multiple phases of fluid chemistries occurred during the evolution of the Waihi system. It has been demonstrated that the same conditions did not affect all the pyrite grains studied. A more in depth study into local conditions at the time of the pyrite formation would provide answers to the questions asked in this study. Samples taken down drill holes at specified depths would show the trace element variation with depth, while comparison across drill holes would highlight any unique local textures. Samples should be taken as far out from the alteration halo as zoned pyrite can be found, as the trace element chemistry from the grains may indicate untapped Au-Ag deposits.

To prove the theory that Au is limited by boiling conditions, an in depth study into the boiling textures and their vertical extent within the Martha lode needs to be done. Identifying the extent of the boiling horizon would allow for comparison with Au concentration in pyrite versus electrum, providing evidence that changing boiling conditions affected incorporation of Au.

In support of the fluid supply control theory, the source of hydrothermal fluid during the Waihi system's evolution needs to be identified and more samples need their Au concentrations quantified. This would allow for an accurate mass balance transfer model to be produced that demonstrates the amount of fluid needed to pass through with a given Au concentration to create the pyrite Au-zoning seen today.

7. Discussion

7.1 Summary of Findings

The focus of the research was to identify variable textures in the pyrite grains from Waihi, and analyse the internal pyrite grain chemistry, to show possible controls on Au-Ag mineralisation, and potential mining and environmental management impacts. There are many low sulfidation high grade ore deposits throughout the world. This case study of the textural and chemical variation within individual pyrite grains in the Waihi epithermal system has shown that the Waihi system history is complex, with possible ore deposits yet to be assayed. Many different types of textural zoning were observed. The controls on the type of texture in a given grain likely include; whether the pyrite was in the vein or was replacement pyrite, how many fluid chemistry changes occurred during the grain's formation, whether there were periods of dissolution, and whether there was preferential incorporation of trace elements on certain crystal faces of a grain. With the increasing demand on precious metals in the last decade, it is becoming imperative to find more deposits and make the mining of current known deposits more efficient (Min et al., 2016).

The gold and Ag in the pyrite grains did not appear to be dependent on the presence of any other trace elements, even As. Inclusion rich grains indicate the deep chloride rich fluids mixed with steam heated ground water, during the time of the grain's formation.

7.2 Theories on Au-Ag Mineralisation

The independence of Au and Ag from other elements within the pyrite, as demonstrated in the previous chapter, suggests a sudden Au precipitation mechanism (such as boiling) or changes in the concentration of Au in the hydrothermal fluid that would control Au concentrations in pyrite in the Waihi system. Considering the source supply control theory (Deditius et al., 2014), studies have yet to provide sufficient evidence from active hydrothermal systems to suggest ligands such as Cl^- and HS^-, along with fluid-mineral equilibria, could limit the amount of trace elements present in the fluid. This is based on the modelling of metal saturation in fluid samples, and evidence is limited due to the lack of metals present in samples of fluid (Simmons et

al., 2016). Although, it must be considered that Au and other metals do remain largely undersaturated in deep hydrothermal fluids (Simmons et al., 2016). Instead, the trace element concentration in the hydrothermal fluid is limited by the relative availabilities from magmatic intrusions and country rock (Simmons et al., 2016). The implication of this is; determining the concentration of metals such as Au, Ag, As, Zn, Cu and Pb within the Waihi pyrite, could produce an estimate of the minimum fluid volume needed to pass through the system, producing the tonnage of Au observed in veins today (Cline, 2001). There is likely to be a significant amount of low grade Au outside the veins, but the exact Au amount would be difficult to accurately quantify without large scale sampling and analyses, owing to the large extent of the Waihi deposit (Brathwaite & Faure, 2002).

Considering the boiling theory, boiling is known to cause metal precipitation (including Au and Ag) inside geothermal wells (Simmons & Browne, 2000). This precipitation and subsequent ore deposit formation could explain why zones within the pyrite at Waihi are sometimes Au and Ag -poor. This is because during the low Au and Ag pyrite formation, ore deposition (as electrum) is occurring, limiting the amount of Au available to be incorporated into pyrite. During boiling, metal bisulfide complexes are destabilised, ideally when proton concentration decrease is slower than the loss of H_2S (Drummond et al., 1985). By the time boiling has produced equal volumes of liquid and vapour phases, metals have been deposited in mineral phase. The efficiency of metal deposition depends on the amount of available H_2S, which is also needed in sulfidation to produce pyrite (Simmons et al., 2016). The result of more H_2S due to boiling could also be conducive to pyrite formation, as once the H_2S is in vapour phase it is available for interacting with the Fe in the wall rock to form pyrite (Blanchard et al., 2007). This suggests that first, ore deposition occurs and then as an indirect result, pyrite formation is possible, due to the presence of H_2S. The equation for this is expressed below. The H produced bonds with S present in the fluid to form more H_2S (Blanchard et al., 2007).

$$2H_2S_{(g)} + Fe \rightarrow FeS_2 + H_{2(g)}$$

This reaction causes the depletion in Au and Ag in the fluid that forms the pyrite. From this it can be implied that where pyrite is found containing zones of relative low and high Au and Ag concentrations respectively, there will also be an ore deposit, as varying concentrations of Ag and Au are indicative of ore formation influencing Ag and Au concentrations within pyrite. Where there are higher concentrations of Au in the pyrite, the pyrite might have formed below the boiling horizon, where the Au and Ag are yet to form mineral phases (Drummond et al., 1985). Further research at Waihi can provide the necessary evidence to support this theory and is discussed in detail in the section below.

7.3 Implications on Precious Metal Deposits in New Zealand

7.3.1The Waihi Au-Ag Deposit

Studying the pyrite textures and geochemistry from within the Waihi epithermal system has demonstrated a complex pattern of zoning and chemical changes, which are interpreted to reflect changes in hydrothermal fluid flow over time. The difference in trace element chemistry between the Cowshed sample and the Martha samples suggests variance between deposits, as well as within each deposit. Cowshed is part of the Favona deposit, which strikes northeast (Christie et al., 2007). The Favona deposit is known to vary chemically from the Martha deposit, with enrichment in Se (Fyfe, 2014). This is shown in figure 7.3.1.1 below.

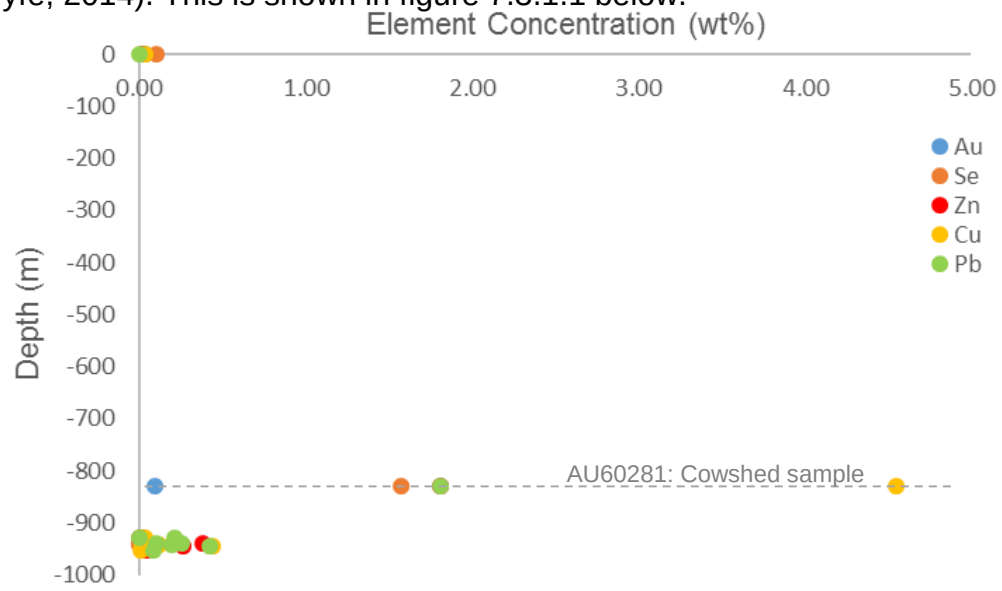

Figure 7.3.1.1: graph of trace elements against depth. The Cowshed sample is the highest in Cu, Pb and Se.

The variety of textures and elemental relationships within the pyrite grains suggests the deposition of the Martha lode in the Waihi epithermal system was influenced by a multitude of conditions that varied both over space and time. The Waihi epithermal system is a low sulfidation epithermal system (Brathwaite & Faure, 2002) therefore internal zoning within the pyrite was not expected, due to the lower oxidation conditions compared to high sulfidation systems, where zoned pyrite is commonly found (Chouinard et al., 2005, Large et al., 2009). This is believed to be the first time internal zoning within pyrite grains has been described in detail in a low sulfidation epithermal system. Previous studies have looked at how pyrite chemistry changes over the alteration halo of a low sulfidation system, but not into the internal zoning structure of individual pyrite grains (Baker et al., 2006). Baker et al. (2006) took samples from all zones of alteration. This included propylitic alteration, argillic alteration, silica-pyrite alteration, epithermal quartz veining and brecciation, and late stage chalcedony fault breccia. Sampling depths ranged from 900-1100 m RL. Baker et al. (2006) found that at Pajingo the Ag/Mo ratios and Pb/Mo ratios varied between alteration zones, and suggested these ratios could be used as microchemical vectors for ore. Applying this finding at Waihi, and the observation of zoning within the pyrite at Waihi both in the wall rock and in vein samples suggests a potential larger extent of zoning outside the examined Martha lode (Simmons & Browne 2000), possibly to the outer boundaries of the Waihi epithermal system alteration halo (Brathwaite & Faure, 2002). The samples in this study are ore-proximal samples, showing insight into the vein system only. The Baker et al. (2006) samples gave a much wider view of trace element distribution. Comparing the similar nature of the pyrite in both the Waihi and Pajingo deposits raises an interesting question for the pyrite at Waihi, based on these two studies; what will pyrite at different distances from the ore bodies at Waihi show? It would also be interesting to compare high Au/Ag pyrite to pyrite from an area with no known significant mineralization, to assess if pyrite has different amounts of Au/Ag. The pyrite might either be barren (no Au/Ag), or perhaps higher, due to no deposition of Au/Ag elsewhere.

7.3.2 The Taupo Volcanic Zone

This research has demonstrated the value of studying ore minerals for the purpose of understanding both epithermal systems and active geothermal systems today. Current fluid studies show that examining the fluid composition in a low sulfidation system, in a volcanic arc setting, will give insight into mineralisation processes, conditions and controls (Simmons et al. 2016). Just as Simmons et al. (2016) has provided a conditional metals transport budget for the active geothermal systems in the Taupo Volcanic Zone, Au-Ag-As-Sb-Te and other metal budgets also have the potential to be calculated in epithermal systems once the history of the system is known (Simmons & Browne, 2000). This could provide information for exploration of known deposits, and suggest the extent of mining capabilities. As pyrite is a 'snapshot' of fluid chemistry at the time of its growth, metal transport budgets have the potential to be calculated based on analysis of internal pyrite chemistry. An interesting study would be to look at pyrite in a system with a well constrained history, age and chemistry of the fluids, and look for zoning in pyrite, and overall pyrite chemistry. Rotokawa is a good example of a system with pyrite and these conditions (Simmons & Brown, 2007). As mentioned above, if pyrite with zones of variable Au and Ag is found outside of a known deposit area, exploration may show unknown ore deposits or extend current known boundaries, even if low grade electrum or native Au is found in initial assays. This would be possible if a link can be demonstrated between pyrite chemistry and mineralisation in an area that pyrite textures and chemistry have potential utility as an exploration tool, as has been demonstrated for other deposit types such as Carlin style and copper porphyry (Large et al., 2009, Reich et al., 2013). As demonstrated in this study, pyrite grains with textural zoning display chemical variations also. Pyrite zoning could potentially provide insight into the conditions over the system as a whole, including the periods of ore formation and high trace element fluid flow (Chouinard et al., 2005).

The Taupo Volcanic Zone (TVZ) can be viewed as the modern analogue for the Waihi epithermal system. The Waihi epithermal system is the southernmost point of the Coromandel Volcanic Zone (CVZ), last active 5-

7 million years ago (Brathwaite & Blattner, 1995). Therefore, assuming that the systems are linked by the same volcanic arc setting, information on fluid chemistry from the active TVZ can be applied to the Waihi system's history. Simmons et al. (2016) measured the concentrations of Ag, As, Au, Cu, Zn, Te and other metals in active geothermal systems in the TVZ by sampling fluids and gases down wells. This type of data produced can be considered as a snapshot in time when compared with the geochemical analysis from a zoned pyrite grain, which represents changes in fluid chemistry over time. The study by Simmons et al. (2016) shows that analysing fluid compositions in an active system is a 'snapshot' in time. Analysis of pyrite zoning provides a more detailed history. It would be interesting to determine the length of time it takes pyrite to grow in favourable conditions, as this could provide further insight into relative time scales for system evolution. The analysis of any pyrite already present in the TVZ could provide a full history of the system up to the present day.

7.3.3 Future Exploration

Assuming that the TVZ and the Waihi epithermal system are linked by the same arc setting, they can be expected to experience many of the same conditions and fluid sources (Simmons et al., 2016). This is important for exploration, as the CVZ is known to host numerous high grade ore deposits (Simpson et al., 2001).

If a relationship can be found between pyrite texture/chemistry and veins, or texture and chemistry towards veins, it has the potential for use as an exploration tool. Paleo fluid studies from the Waihi pyrite could provide accurate predictions of future Au-rich fluid flow in the TVZ. This opens up the possibility for identifying ore deposits as they are forming in the TVZ. Identifying these currently forming ore deposits has the potential to significantly improve both the economy and overall environmental impact of mining in the future. There is the potential that if processes can be understood that drive gold capture onto pyrite, the information could be used to deliberately to remove gold from solution.

7.4. Future Work

Following the geochemical analysis and interpretation of the chemistry in the pyrite from the Martha lode, a number of questions have arisen. Firstly, does this internal variation in the pyrite grains occur in all lodes in the Waihi system? Second, can we determine a boiling horizon using the pyrite geochemistry and depth data? And third, do internally zoned pyrites occur on the outer boundaries of the alteration halo? And finally; does the pyrite chemistry and texture change with proximity to veins, thus having potential exploration utility?

The importance of sample context has also been highlighted. Sampling within a greater paragenetic context would be valuable in providing a better idea of timing of the overall Waihi system. Analytical techniques such as core scanning would also aid in placing samples in context.

In answer to the first question, a more detailed and in depth study of the pyrite grains from surrounding deposits such as the Correnso, Favona and Welcome deposits would provide information on the type and extent of the pyrite zoning within the other areas of the Waihi deposit. Studying of the location of the outer reaches of the alteration halo would provide a basis for sampling for the total extent of pyrite zoning at Waihi. Replication of the methods from this research would provide adequate data to produce evidence for the boundaries of the pyrite zoning in the Waihi epithermal system. In retrospect, looking at the pyrite in broader context would have provided a better insight into conditions in the Waihi system. This proof of concept study has successfully demonstrated that there is zoning in the pyrite at Waihi in many forms. However, more work needs to be done to better understand the Waihi system. This study looked at a limited data set, and there were several issues with the data produced via EPMA and LA-ICPMS. A lot of the known Au and Ag in the deposits in the Waihi system is known to occur as electrum (Brathwaite & Faure, 2002). Both instruments were used for analysing for Au and Ag within the pyrite grains, and as a result, most electrum was ignored. Unless a gold inclusion was observed and the EPMA beam placed directly over it for analysis, any inclusions would easily be missed. The LA-ICPMS looked mostly at the relative

concentrations of Au and Ag against Fe^{57} concentration, as the data was only semi quantitative, owing to the absence of a sulfide trace element LA-ICPMS standard.

With respect to the second question, to provide evidence that boiling conditions are responsible for the variation in Au and Ag in the pyrite zones, a study of the boiling textures down drill holes needs to be done. This should be accompanied by geochemical analysis of the pyrite grains throughout the extent of the drill hole. If there is a sudden depletion in Au and Ag in all zones where boiling textures are encountered, there will be evidence to suggest the boiling conditions are the main controls on Au/Ag concentration (Simmons et al., 2016). However, there is a timing issue associated with this theory. For example, if a grain grew after boiling, it would be low in Au and Ag regardless of whether it was below or above the boiling horizon.

Sampling of pyrite grains found at the boundary of the alteration halo (if any) and bleach etching of these grains will highlight the extent to which the zoned pyrite occurs. Geochemical analysis of zones near the boundary of the alteration halo will indicate the Au and Ag levels and potential ore deposits by comparison with the geochemistry of the grains from within high grade deposits such as the Martha deposit.

It would also be possible to illustrate the history of a specific vein using these methods. Sampling from a single vein, with samples taken in context ie. within the sulfide band, within the quartz matrix or within the wall rock and at specified depth would provide enough data for a construction of paleo fluid chemistry during each pyrite grain's growth period. Isolating the zones within grains of high Au and Ag, along with their associated depth and time would enable a 4D model of auriferous fluid flow through veins to be made.

8. Conclusion

The Waihi epithermal system is a high grade economic ore deposit. The system contains a variety of minerals including sulfides, the most common of which is pyrite. Pyrite is a ubiquitous mineral found in many different settings. Pyrite is important to study due to its capability of incorporating trace elements into its crystal structure, given the right conditions.

This is a new and thus unique study almost globally on low sulfidation systems, other than the research mentioned by Baker et al. (2006). There are many different types of internal zoning observed in the pyrite grains from the Martha lode in the Waihi epithermal system. These range from central zones with outer borders, to zoning that adopts a tree ring appearance, with multiple zones. These varying zones suggest a complex history of fluid movement, varying over vertical and horizontal extent.

The textural zones found in the pyrite are indicative of chemical differences between zones. As is the main contributor to the colour change observed under reflected light microscopy, after the pyrite grain is etched.

The varying concentration of Zn and Cu between samples of different depths reflects that with a decrease in depth there is a change from Zn-Pb sulfides to Zn-Pb-Cu-Ag sulfides and electrum.

The independence of Au in the pyrite suggests that the controls of Au concentrations are not coupling with As or temperature controls but rather due to varying boiling conditions or a limited supply at the fluid source. Both theories have merit but further study is required to provide sufficient evidence in support of either.

The variation in Au and Ag concentration in the pyrite internally, and across all samples, suggests that the history of auriferous fluid flow in the Martha deposit is more complex than current studies suggest. This can be of use to Oceana Gold, who currently own and are continuing exploration in the Martha mine, as it suggests there is more to know about the Au and Ag behaviour in the Martha deposit, and this type of knowledge could improve mining outputs.

References

Anawar, H. M. (2015). Sustainable rehabilitation of mining waste and acid mine drainage using geochemistry, mine type, mineralogy, texture, ore extraction and climate knowledge. Journal of Environmental Management, 158, 111-121. doi: http://dx.doi.org/10.1016/j.jenvman.2015.04.045

Arribas Jr, A. (1995). Characteristics of high-sulfidation epithermal deposits, and their relation to magmatic fluid. Mineralogical Association of Canada Short Course, 23, 419-454.

Baker, T., Mustard, R., Brown, V., Pearson, N., Stanley, C. R., Radford, N. W., & Butler, I. (2006). Textural and chemical zonation of pyrite at Pajingo: a potential vector to epithermal gold veins. Geochemistry-Exploration Environment Analysis, 6, 283-293. doi: 10.1144/1467-7873/05-077

Berner, R. A. (1970). Sedimentary pyrite formation. American Journal of Science, 268(1), 1-23.

Blanchard, M., Alfredsson, M., Brodholt, J., Wright, K., & Catlow, C. R. A. (2007). Arsenic incorporation into FeS 2 pyrite and its influence on dissolution: a DFT study. Geochimica et cosmochimica acta, 71(3), 624-630.

Borrelli, L., Antronico, L., Gulla, G., & Sorriso-Valvo, G. M. (2014). Geology, geomorphology and dynamics of the 15 February 2010 Maierato landslide (Calabria, Italy). Geomorphology, 208, 50-73. doi: 10.1016/j.geomorph.2013.11.015

Boyle, R. (1969). Hydrothermal transport and deposition of gold. Economic Geology, 64(1), 112-115.

Brathwaite, R. L., & Faure, K. (2002). The Waihi epithermal gold-silver-base metal sulfide-quartz vein system, New Zealand: Temperature and salinity controls on electrum and sulfide deposition. Economic Geology, 97(2), 269-290.

Brostigen, G., & Kjekshus, A. (1969). Redetermined crystal structure of fes 2--pyrite. Acta Chem Scand, 23(6), 2186-2188.

Camera, C. A. S., Apuani, T., & Masetti, M. (2014). Mechanisms of failure on terraced slopes: the Valtellina case (northern Italy). Landslides, 11(1), 43-54. doi: 10.1007/s10346-012-0371-3

Cascini, L., Cuomo, S., & Pastor, M. (2013). Inception of debris avalanches: remarks on geomechanical modelling. Landslides, 10(6), 701-711. doi: 10.1007/s10346-012-0366-0

Castendyk, D., & Webster-Brown, J. (2010). Effects of mine expansion on geochemical predictions of pit lake water quality: an example from Martha Mine, Waihi, New Zealand. New Zealand Journal of Geology and Geophysics, 53(2-3), 143-151.

Castendyk, D. N., Mauk, J. L., & Webster, J. G. (2005). A mineral quantification method for wall rocks at open pit mines, and application to the Martha Au–Ag mine, Waihi, New Zealand. Applied Geochemistry, 20(1), 135-156. doi: http://dx.doi.org/10.1016/j.apgeochem.2004.07.001

Chandra, A., & Gerson, A. R. (2010). The mechanisms of pyrite oxidation and leaching: a fundamental perspective. Surface Science Reports, 65(9), 293-315.

Christie, A. B., Simpson, M. P., Brathwaite, R. L., Mauk, J. L., & Simmons, S. F. (2007). Epithermal Au-Ag and related deposits of the Hauraki goldfield, Coromandel volcanic zone, New Zealand. Economic Geology, 102(5), 785-816.

Clarke, J. E. H., Marques, C. R. V., & Pratomo, D. (2014). Imaging Active Mass-Wasting and Sediment Flows on a Fjord Delta, Squamish, British Columbia (Vol. 37).

Cline, J. S. (2001). Timing of gold and arsenic sulfide mineral deposition at the Getchell Carlin-type gold deposit, north-central Nevada. Economic Geology, 96(1), 75-89.

Craw, D. (2001). Tectonic controls on gold deposits and their environmental impact, New Zealand. Journal of Geochemical Exploration, 73(1), 43-56. doi: http://dx.doi.org/10.1016/S0375-6742(01)00171-6

Danyushevsky, L., Robinson, P., Gilbert, S., Norman, M., Large, R., McGoldrick, P., & Shelley, M. (2011). Routine quantitative multi-element analysis of sulphide minerals by laser ablation ICP-MS: Standard development and consideration of matrix effects. Geochemistry: Exploration, Environment, Analysis, 11(1), 51-60.

Deditius, A. P., & Reich, M. (2016). Constraints on the solid solubility of Hg, Tl, and Cd in arsenian pyrite. American Mineralogist, 101(6), 1451-1459.

Deditius, A. P., Reich, M., Kesler, S. E., Utsunomiya, S., Chryssoulis, S. L., Walshe, J., & Ewing, R. C. (2014). The coupled geochemistry of Au and As in pyrite from hydrothermal ore deposits. Geochimica et cosmochimica acta, 140, 644-670. doi: http://dx.doi.org/10.1016/j.gca.2014.05.045

Deditius, A. P., Utsunomiya, S., Reich, M., Kesler, S. E., Ewing, R. C., Hough, R., & Walshe, J. (2011). Trace metal nanoparticles in pyrite. Ore Geology Reviews, 42(1), 32-46.

Deol, S., Deb, M., Large, R. R., & Gilbert, S. (2012). LA-ICPMS and EPMA studies of pyrite, arsenopyrite and loellingite from the Bhukia-Jagpura gold prospect, southern Rajasthan, India: Implications for ore genesis and gold remobilization. Chemical Geology, 326, 72-87.

Drummond, S., & Ohmoto, H. (1985). Chemical evolution and mineral deposition in boiling hydrothermal systems. Economic Geology, 80(1), 126-147.

Fyfe, S. (2014). Variable ore mineralogy in the Waihivein system, Hauraki Goldfield, Waihi, New Zealand. (Master of Science (Geology)), University of Auckland, Auckland, New Zealand.

Genna, D., & Gaboury, D. (2015). Deciphering the Hydrothermal Evolution of a VMS System by LA-ICP-MS Using Trace Elements in Pyrite: An Example from the Bracemac-McLeod Deposits, Abitibi, Canada, and Implications for Exploration. Economic Geology, 110(8), 2087-2108.

Graf, J. L., & Skinner, B. J. (1970). Strength and deformation of pyrite and pyrrhotite. Economic Geology, 65(2), 206-&.

Gregory, D. D., Large, R. R., Halpin, J. A., Steadman, J. A., Hickman, A. H., Ireland, T. R., & Holden, P. (2015). The chemical conditions of the late Archean Hamersley basin inferred from whole rock and pyrite geochemistry with Δ 33 S and δ 34 S isotope analyses. Geochimica et cosmochimica acta, 149, 223-250.

Gregory, M. J., Lang, J. R., Gilbert, S., & Hoal, K. O. (2013). Geometallurgy of the pebble porphyry copper-gold-molybdenum deposit, Alaska: implications for gold distribution and paragenesis. Economic Geology, 108(3), 463-482.

Gurung, S., Stewart, R., Gregg, P., & Bolan, N. (2000). An assessment of requirements of neutralising materials of partially oxidised pyritic mine waste rock. Soil Research, 38(2), 329-344.

Hofstra, A., Leventhal, J., Northrop, H., Landis, G., Rye, R., Birak, D., & Dahl, A. (1991). Genesis of sediment-hosted disseminated-gold deposits by fluid mixing and sulfidization: Chemical-reaction-path modeling of ore-depositional processes documented in the Jerritt Canyon district, Nevada. Geology, 19(1), 36-40.

Hu, G., Dam-Johansen, K., Wedel, S., & Hansen, J. P. (2006). Decomposition and oxidation of pyrite. Progress in Energy and Combustion Science, 32(3), 295-314.

Huang, X.-W., Gao, J.-F., Qi, L., & Zhou, M.-F. (2015). In-situ LA-ICP-MS trace elemental analyses of magnetite and Re–Os dating of pyrite: The Tianhu hydrothermally remobilized sedimentary Fe deposit, NW China. Ore Geology Reviews, 65, Part 4, 900-916. doi: http://dx.doi.org/10.1016/j.oregeorev.2014.07.020

Hungr, O., Leroueil, S., & Picarelli, L. (2014). The Varnes classification of landslide types, an update. Landslides, 11(2), 167-194. doi: 10.1007/s10346-013-0436-y

Huston, D. L., Sie, S. H., Suter, G. F., Cooke, D. R., & Both, R. A. (1995). Trace elements in sulfide minerals from eastern Australian volcanic-hosted massive sulfide deposits; Part I, Proton microprobe analyses of pyrite, chalcopyrite, and sphalerite, and Part II, Selenium levels in pyrite; comparison with delta 34 S values and implications for the source of sulfur in volcanogenic hydrothermal systems. Economic Geology, 90(5), 1167-1196.

Large, R. R., Danyushevsky, L., Hollit, C., Maslennikov, V., Meffre, S., Gilbert, S., . . . Thomas, H. (2009). Gold and trace element zonation in pyrite using a laser imaging technique: implications for the timing of gold in orogenic and Carlin-style sediment-hosted deposits. Economic Geology, 104(5), 635-668.

Li, W., Wu, S. G., Wang, X. J., Zhao, F., Wang, D. W., Mi, L. J., & Li, Q. P. (2014). Baiyun Slide and Its Relation to Fluid Migration in the Northern Slope of Southern China Sea (Vol. 37).

Lloyd, J., & Taylor, J. (1994). On the temperature dependence of soil respiration. Functional ecology, 315-323.

Lowson, R. T. (1982). Aqueous oxidation of pyrite by molecular oxygen. Chemical Reviews, 82(5), 461-497.

Luther, G. W. (1987). Pyrite oxidation and reduction: molecular orbital theory considerations. Geochimica et cosmochimica acta, 51(12), 3193-3199.

McClay, K., & Ellis, P. (1983). Deformation and recrystallization of pyrite. Mineralogical Magazine, 47(4), 527-538.

Min, X. B., Xue, K., Ke, Y., Zhou, B. S., Li, Y. W. J., & Wang, Q. W. (2016). Sulfidation Roasting of Hemimorphite with Pyrite for the Enrichment of Zn and Pb. Jom, 68(9), 2435-2442. doi: 10.1007/s11837-016-1986-y

Myagkaya, I. N., Lazareva, E. V., Gustaytis, M. A., & Zhmodik, S. M. (2016). Gold and silver in a system of sulfide tailings. Part 1: Migration in water flow. Journal of Geochemical Exploration, 160, 16-30. doi: http://dx.doi.org/10.1016/j.gexplo.2015.10.004

Orchard, V. A., & Cook, F. J. (1983). Relationship between soil respiration and soil moisture. Soil Biology and Biochemistry, 15(4), 447-453. doi: http://dx.doi.org/10.1016/0038-0717(83)90010-X

Parian, M., Lamberg, P., Möckel, R., & Rosenkranz, J. (2015). Analysis of mineral grades for geometallurgy: Combined element-to-mineral conversion and quantitative X-ray diffraction. Minerals Engineering, 82, 25-35. doi: http://dx.doi.org/10.1016/j.mineng.2015.04.023

Paton, C., Hellstrom, J., Paul, B., Woodhead, J., & Hergt, J. (2011). Iolite: Freeware for the visualisation and processing of mass spectrometric data. Journal of Analytical Atomic Spectrometry, 26(12), 2508-2518. doi: 10.1039/c1ja10172b

Paul, B., Paton, C., Norris, A., Woodhead, J., Hellstrom, J., Hergt, J., & Greig, A. (2012). CellSpace: A module for creating spatially registered laser ablation images within the Iolite freeware environment. Journal of Analytical Atomic Spectrometry, 27(4), 700-706. doi: 10.1039/c2ja10383d

Pirajno, F. (2009). Hydrothermal processes associated with meteorite impacts. In Hydrothermal Processes and Mineral Systems (pp. 1097-1130). Springer Netherlands.

Pope, J., & Trumm, D. (2015). Controls on Zn Concentrations in Acidic and Neutral Mine Drainage from New Zealand's Bituminous Coal and Epithermal Mineral Deposits. Mine Water and the Environment, 34(4), 455-463.

Pownceby, M. I., & Johnson, C. (2014). Geometallurgy of Australian uranium deposits. Ore Geology Reviews, 56, 25-44. doi: http://dx.doi.org/10.1016/j.oregeorev.2013.07.001

Read, S., Perrin, N., & Richards, L. (1999). Applicability of the Hoek-Brown failure criterion to New Zealand greywacke rocks. Paper presented at the 9th ISRM Congress.

Reich, M., Chryssoulis, S. L., Deditius, A., Palacios, C., Zúñiga, A., Weldt, M., & Alvear, M. (2010). "Invisible" silver and gold in supergene digenite (Cu 1.8 S). Geochimica et cosmochimica acta, 74(21), 6157-6173.

Reich, M., Deditius, A., Chryssoulis, S., Li, J.-W., Ma, C.-Q., Parada, M. A., . . . Mittermayr, F. (2013). Pyrite as a record of hydrothermal fluid evolution in a porphyry copper system: A SIMS/EMPA trace element study. Geochimica et cosmochimica acta, 104, 42-62. doi: http://dx.doi.org/10.1016/j.gca.2012.11.006

Rottier, B., Kouzmanov, K., Walle, M., Bendezu, R., & Fontbote, L. (2016). Sulfide Replacement Processes Revealed by Textural and LA-ICP-MS Trace Element Analyses: Example from the Early Mineralization Stages at Cerro de Pasco, Peru. Economic Geology, 111(6), 1347-1367.

Rovere, M., Gamberi, F., Mercorella, A., & Leidi, E. (2014). Geomorphometry of a submarine mass-transport complex and relationships with active faults in a rapidly uplifting margin (Gioia Basin, NE Sicily margin). Marine Geology, 356, 31-43. doi: 10.1016/j.margeo.2013.06.003

Seward, T. (1993). The hydrothermal geochemistry of gold Gold metallogeny and exploration (pp. 37-62): Springer.

Shoaei, Z. (2014). Mechanism of the giant Seimareh Landslide, Iran, and the longevity of its landslide dams. Environmental Earth Sciences, 72(7), 2411-2422. doi: 10.1007/s12665-014-3150-8

Simmons, S. F., & Brown, K. L. (2007). The flux of gold and related metals through a volcanic arc, Taupo Volcanic Zone, New Zealand. Geology, 35(12), 1099-1102.

Simmons, S. F., Brown, K. L., & Tutolo, B. M. (2016). Hydrothermal Transport of Ag, Au, Cu, Pb, Te, Zn, and Other Metals and Metalloids in New Zealand Geothermal Systems: Spatial Patterns, Fluid-Mineral Equilibria, and Implications for Epithermal Mineralization. Economic Geology, 111(3), 589-618.

Simmons, S. F., White, N. C., & John, D. A. (2005). Geological characteristics of epithermal precious and base metal deposits. Economic Geology 100th anniversary volume, 29, 485-522.

Steadman, J. A., Large, R. R., Davidson, G. J., Bull, S. W., Thompson, J., Ireland, T. R., & Holden, P. (2014). Paragenesis and composition of ore minerals in the Randalls BIF-hosted gold deposits, Yilgarn Craton, Western Australia: Implications for the timing of deposit formation and constraints on gold sources. Precambrian Research, 243, 110-132.

Steadman, J. A., Large, R. R., Meffre, S., & Bull, S. W. (2013). Age, origin and significance of nodular sulfides in 2680Ma carbonaceous black shale of the Eastern Goldfields Superterrane, Yilgarn Craton, Western Australia. Precambrian Research, 230, 227-247.

Steadman, J. A., Large, R. R., Meffre, S., Olin, P. H., Danyushevsky, L. V., Gregory, D. D., . . . Holden, P. (2015). Synsedimentary to Early Diagenetic Gold in Black Shale-Hosted Pyrite Nodules at the Golden Mile Deposit, Kalgoorlie, Western Australia. Economic Geology, 110(5), 1157-1191.

Steiner, A., & Rafter, T. A. (1966). Sulfur isotopes in pyrite, pyrrhotite, alunite and anhydrite from steam wells in the Taupo volcanic zone, New Zealand. Economic Geology, 61(6), 1115-1129.

Thomas, H. V., Large, R. R., Bull, S. W., Maslennikov, V., Berry, R. F., Fraser, R., . . . Moye, R. (2011). Pyrite and pyrrhotite textures and composition in sediments, laminated quartz veins, and reefs at Bendigo gold mine, Australia: insights for ore genesis. Economic Geology, 106(1), 1-31.

Wang, L., Wu, S. G., Li, Q. P., Wang, D. W., & Fu, S. Y. (2014). Architecture and development of a multi-stage Baiyun submarine slide complex in the Pearl River Canyon, northern South China Sea. Geo-Marine Letters, 34(4), 327-343. doi: 10.1007/s00367-014-0372-4

White, N. C., & Hedenquist, J. W. (1995). Epithermal gold deposits: styles, characteristics and exploration. SEG newsletter, 23(1), 9-13.

Williams-Jones, A. E., & Heinrich, C. A. (2005). 100th Anniversary special paper: Vapor transport of metals and the formation of magmatic-hydrothermal ore deposits. Economic Geology, 100(7), 1287-1312. doi: 10.2113/100.7.1287

Yan, Y., Zhang, N., Li, S., & Li, Y. (2014). Mineral chemistry and isotope geochemistry of pyrite from the Heilangou gold deposit, Jiaodong Peninsula, Eastern China. Geoscience Frontiers, 5(2), 205-213.

Zaw, K., Gemmell, J., Large, R., Mernagh, T., & Ryan, C. (1996). Evolution and source of ore fluids in the stringer system, Hellyer VHMS deposit, Tasmania, Australia: evidence from fluid inclusion microthermometry and geochemistry. Ore Geology Reviews, 10(3), 251-278.

Zhu, Y., An, F., & Tan, J. (2011). Geochemistry of hydrothermal gold deposits: A review. Geoscience Frontiers, 2(3), 367-374. doi: http://dx.doi.org/10.1016/j.gsf.2011.05.006

Appendices

All appendices are digital. The outline for the structure of the digital copy is below.

Appendix I – Samples

- AU samples
- XFM samples

Appendix II – Raw Data

- EPMA
- LA-ICPMS
- XFM

Appendix III – Analysis Images

- EPMA Backscatter
- LA-ICPMS (iolite)
- XFM RBG Maps